THE UNIVERSITY OF CHICAGO

CONTROL OF ESCAPE BEHAVIOR BY DESCENDING NEURONS IN DROSOPHILA MELANOGASTER

A DISSERTATION SUBMITTED TO
THE FACULTY OF THE DIVISION OF THE BIOLOGICAL SCIENCES
AND THE PRITZKER SCHOOL OF MEDICINE
IN CANDIDACY FOR THE DEGREE OF
DOCTOR OF PHILOSOPHY

BIOLOGY

BY
MARTIN Y. PEEK

CHICAGO, ILLINOIS
DECEMBER 2018

TABLE OF CONTENTS

LIST OF FIGURES

LIST OF TABLES

ACKNOWLEDGMENTS

I would like to give special thanks to my advisor, Gwyneth Card, for supporting me through the PhD process. The Card lab has been integral to my scientific development, and I am indebted to each member: Katie, Pat, Ryan, Jan, Hiro, Erica, Nathan and Tess. The environment at Janelia for studying fly neuroscience is special to me because of the people who work so hard to move the science forward. I appreciate the conversations with everyone, and in particular Allan, Stephen, Eyal, Sung-Soo, Alice, Kristin, Johannes, Ed, Michael, and Aljoscha. There is an instrumentation group at Janelia where I have always felt welcome to put my engineering hat back on. I have had memorable discussions about designing and building with Peter, Bruce, Bill, Tanya, Brian, Jason and Magnus.

I would like to also recognize my graduate program classmates. It has been a better journey struggling through together. Special thanks to Brian, Mathias, Jack, Sam, TJ, Zhihao, Davis, Hannah, Kelly, Dylan, Mai, Max, Mischa, Barrett, Robin, John and Rudy.

Outside of lab, I was fortunate enough to find some enriching things near Ashburn. I enjoyed learning how to throw pottery from Shawn with Heather, Tomoko, Meghan, Allan, Holly, Angela and Sandy. I also kept my fitness up rock climb with Kristin, Katie, Stephen, Meghan and Kasper. Thanks to Daniel for coordinating a few woodworking projects.

After driving up to UChicago from Janelia in 2011, I was welcomed by Melina into her lab where I met and learned from many wonderful scientists, including Matt and Yen-Chyi. My experience there was formative in starting to become a neuroscientist and neuroethologist, and so I am grateful to Dan and Melina, and the UChicago community.

I am grateful for conversations and guidance from my Janelia/UChicago graduate committee: Dan, Melina, Vivek and Gabe. Through my time in the program, I was also supported and encouraged by Kevin, Katie, Maryrose, Ulrike and Erik. Thanks to Hoang and Elena for helping schedule and organize the defense, and thanks to Glenn, Masashi, Eyal and Minoru for presentation feedback.

Finally, thanks to Gerry for developing the Janelia Research Campus, which made the

work presented here possible. I am grateful for the effort, insight and dedication of my collaborators. At the end of chapters 2 and 3, I have included descriptions to highlight the contributions of my colleagues.

CHAPTER 1

INTRODUCTION

1.1 Introduction to Nervous Systems and Behavior

A primary function of the animal nervous system is the detection of changes in the external environment in order to generate appropriate actions. Movement is a critical response because the resources that are required for survival and reproduction are heterogeneously distributed in the environment. Sensing and movement improves the chances of finding food, accessing mates and avoiding danger [5]. Sensory neurons, cells specialized to detect light, odors, vibrations, or other stimuli, detect changes in external environment and transmit chemo-electric signals to interconnected networks, or circuits, of neurons in order to determine an appropriate action. To move, specialized neurons called motor neurons signal muscle cells which contract to pull parts of the body into new orientations. Combinations of contractions coordinate movement and produce locomotion by applying forces against the local environment. Similar movements are grouped into behaviors, such as running, jumping and swimming. Sensorimotor pathways, the circuits comprised of sensory neurons, motor neurons, and neurons which connected them, link stimulus to behavior. The structure and function of these interconnections are the least characterized, and the focus of my research.

1.1.1 Basic anatomy of the central nervous system

Nervous system architecture is classified into two groups: nerve nets and central nervous systems. Nerve nets consist of interconnected neurons in radially-symmetric animals such as jellyfish and hydra (Cnidarians), comb jellies (Ctenophores), and starfish (Echinoderms). The Hydra nerve net is composed of a diffuse lattice of neurons that form neural circuits. These circuits are associated with distinct behavioral responses to particular types of sensory stimuli, for example body contraction and elongation in response to light [40]. Bilaterally-symmetric animals (Bilaterians) generally develop central nervous systems that are composed

of the brain and the nerve cord, organs with a high density of neurons and neuroglial support cells. The central nervous system is more sophisticated than a nerve net. It receives and transmits information to all parts of the body, and forms complex neural circuits that regulate internal processes like emotional state and homeostasis, as well as control behaviors such as speaking and writing. The identification and characterization of different circuits is a main objective in current neuroscience research [165].

The central nervous system is functionally segregated. The brain is formed by a developmental process and evolutionary trend called cephalization, in which anterior sense organs and ganglia of the nervous system are fused together to form a brain [135]. The brain serves as the major information processing center and receives sensory signals from the visual, mechanosensory, vestibular, olfactory, gustatory and auditory systems, among others [74]. This information is passed via sensory afferents from sense organs in the head or from other parts of the body. The brain integrates this information and forms signals for movement that are transmitted down to the nerve cord. The nerve cord contains motor nerves which control muscle contraction, as well as local circuits which form reflexes and locomotor patterns [77]. An animal can perform its full range of behaviors through the coordinated activity of the brain and nerve cord.

1.1.2 Descending neurons and behavior

Neural signals are passed from the brain to the nerve cord through descending neurons (DNs). The information passed from sensory processing centers in the brain to motor circuits in the nerve cord must be encoded within a set of neurons that is orders of magnitude fewer in number than in the brain or nerve cord. In vertebrate locomotion, DN activity is critical for anticipatory movements such as changing locomotor gait on uneven ground or for stepping over objects. Descending signals also maintain a base of postural support upon which these locomotor changes are superimposed. The overall behavior observed is thought to be the integration of these DN signals with local activity in the nerve cord [37].

DNs represent a bottleneck within the central nervous system. In model organisms used for neuroscience research, anatomical studies have estimated the number of DNs in comparison to the number of neurons in the brain and nerve cord. In the fruit fly, *Drosophila melanogaster*, the brain is composed of ∼135,000 neurons [3], the nerve cord of ∼10,000 neurons [142], and the DNs of 300-500 bilaterally-symmetric pairs [59, 68, 106], approximately 0.5% of the total neurons [3]. Generally, animals have a relatively limited number of DNs with which to signal the nerve cord. Because scientists work in a regime where our ability to measure neural activity at high fidelity is limited, DNs are a key target for understanding how specific brain signals control behavior.

Early studies focused on the most conspicuous, largest DNs, and found that they are often important for generating startle and escape behaviors [42]. For example, in flies [155] and anamniotes (lamprey, teleost fish, amphibians) [41], activity in the pair of giant descending neurons drive escapes. Behavioral studies indicate that escape can be readily elicited with visual or mechanosensory stimuli that mimic predators rapidly approaching the animal [42]. By examining the neural basis of the escape behavior, we seek to understand how the brain rapidly detects and transforms these threatening stimuli into signals that are transmitted down DNs to motor neurons to generate escapes.

While escape studies have focused on the giant DNs, there is strong evidence that additional DNs serve as functional parallel pathways. A neural circuit with multiple information channels may provide additional robustness or serve to increase their dynamic range and flexibility [95]. In zebrafish, the pair giant DNs, the Mauthner cells, along with two homologous pairs MiD2cm and MiD3cm, form the Mauthner array, a group of six DNs which contribute to escapes [109, 91]. In fruit flies and larger fly species, anatomical evidence for DNs sharing some characteristics with the giant fiber (GF) descending neuron have been reported [73, 100], but their functional roles remain unexplored.

1.2 Overview of Escape Behavior Research

The study of sensorimotor processing requires detailed investigation of neural circuits and the actions they produce. Neural systems which control startle and escape behavior have been particularly amenable to investigation for several key reasons. These behaviors are typically low-latency responses to threatening stimuli. Rapidity minimizes the time between threat detection and motor output, potentially limiting the number of involved neurons and complexity of the neural processing, thereby limiting experimental scope and facilitating modeling. Escapes are often high acceleration movements whose kinematics are relatively stereotyped within species, facilitating behavioral characterization and detection of perturbations. Startle and escape are essential to survival, and are critical in determining the evolutionary fitness of prey under selective pressure by predation. They have been observed in species across the animal kingdom, allowing comparative examination of neural circuit properties. They are robust, so are easily adaptable for study in laboratory conditions. Finally, in several of these species, underlying neural circuits contain conspicuous giant neurons with large axons which are amenable for physiological techniques for functional characterization [60].

1.2.1 The Looming stimulus paradigm and visually-mediated escapes

To examine startle and escape in diverse animal species, researchers have employed a range of sensory stimuli, including mechanosensory impulses, noxious odors, sharp sounds and visual expansion [42]. In visually-mediated escape, when predator attacks, its approach will create a looming, or expanding, stimulus on the prey's eye. Recently, researchers have focused on a common visual paradigm that models these stimuli. Formalized by Gabbiani [53], looming stimuli are typically designed to mimic a dark object on a light background approaching at constant velocity (v), modeling the angular size of the object on the fly's retina (θ) as a function of time (t):

$$\theta(t) = \arctan\left(\frac{l}{v * t}\right) \tag{1.1}$$

The pattern of looming expansion is defined by l/v (also called r/v in some literature), which is the ratio of the approaching virtual object's radius (l) to its approach velocity (v) (Figure 1.1). This creates a non-linear growth curve over time. By adopting this definition, looming responses have been characterized in a range of cell types and brain regions in different species.

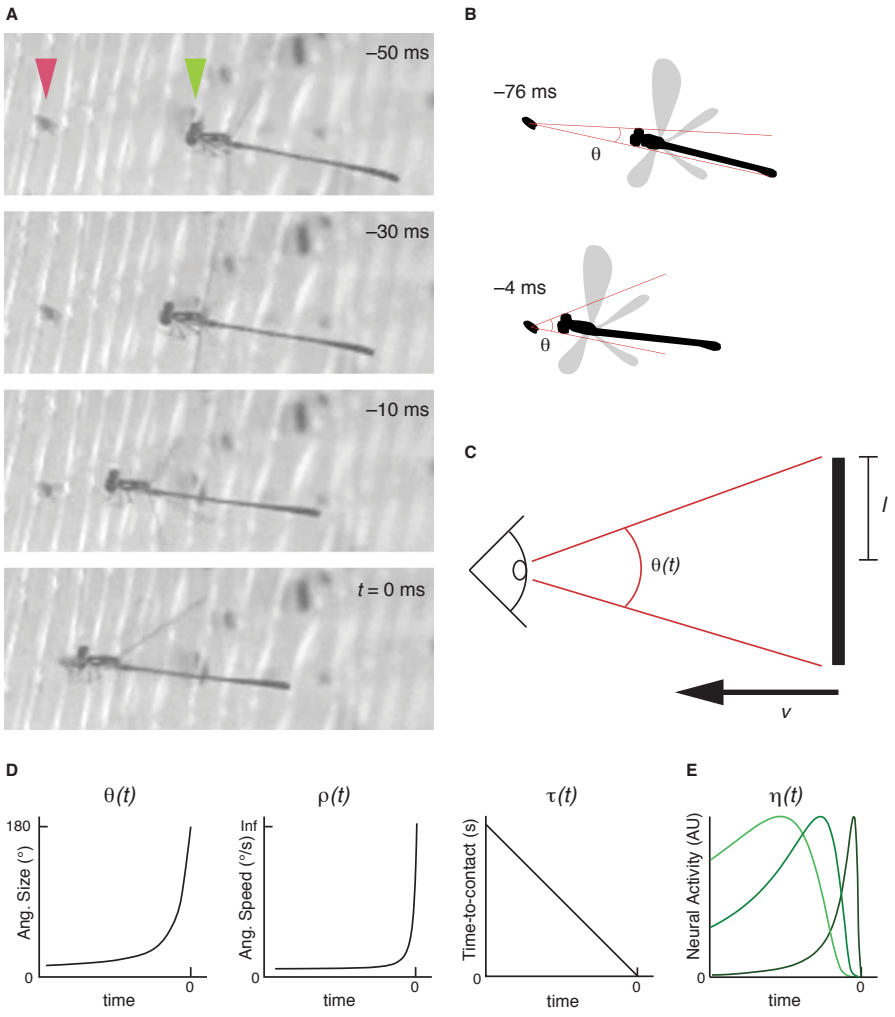

Figure 1.1: Looming Stimulus Paradigm
(A) Video montage of a damselfly predatory approach toward a perched Drosophila, with $t = 0$ at time of damselfly-fly contact. Green arrow indicates fly and red arrow indicates damselfly. Images recorded at 1000 frames per second.
(B) As the damselfly approaches the fly, it projects a larger image on the flys retina, as measured by its angular size (θ). A and B adapted from [155].
(C) Looming stimuli emulate an object with half-size (l) approaching with constant velocity (v), covering an angular size (θ) of the preys retina. The size-to-speed ratio, l/v, characterizes the non-linear increase in θ over time. Adapted from [48].
(D) Evolution of kinematic parameters of the looming stimulus during approach time. $\theta(t)$ is the loom angular size, $\rho(t)$ is the loom angular velocity and (τ) is the time-to-contact. $t = 0$ at the theoretical time-to-contact, where $\theta = 180°$.
(E) The derived optic variable, η, is a non-linear function of the loom size, $\theta(t)$, and speed, $\rho(t)$. Looms with different l/v values (represented by different shades of green) will lead to peak θ values at different times relative to time-to-contact. However, these peaks will all occur at a fixed delay after the stimulus reaches a certain size threshold, regardless of loom speed (or l/v). D and E adapted from [88]. Reproduced from [114].

Whether by convergence or homology, escape circuits across species take on a remarkably similar organization. Looming-sensitive neurons have been reported in vertebrate retinal ganglion cells [147], thalamus [141] and superior colliculus [39], as well as the invertebrate optic lobe [156, 82, 64, 107]. Looming information is passed through a direct route to motor areas in the nerve cord. In the locust, some looming-sensitive visual projection neurons have been shown to synapse directly on descending interneurons [110], and multiple looming-sensitive descending pathways have been found [49]. In mammals, non-cortical looming-escape pathways have been identified in the mouse [129]. Direct comparison of responses reveals remarkable conservation in computation and neuroanatomy across species. Evidence shows at least one class of looming-sensitive response, η, is present in animals as diverse as insects and mammals (Figure 1.2), and encodes a looming size threshold used to activate escape behaviors before predator contact. (Adapted from [114])

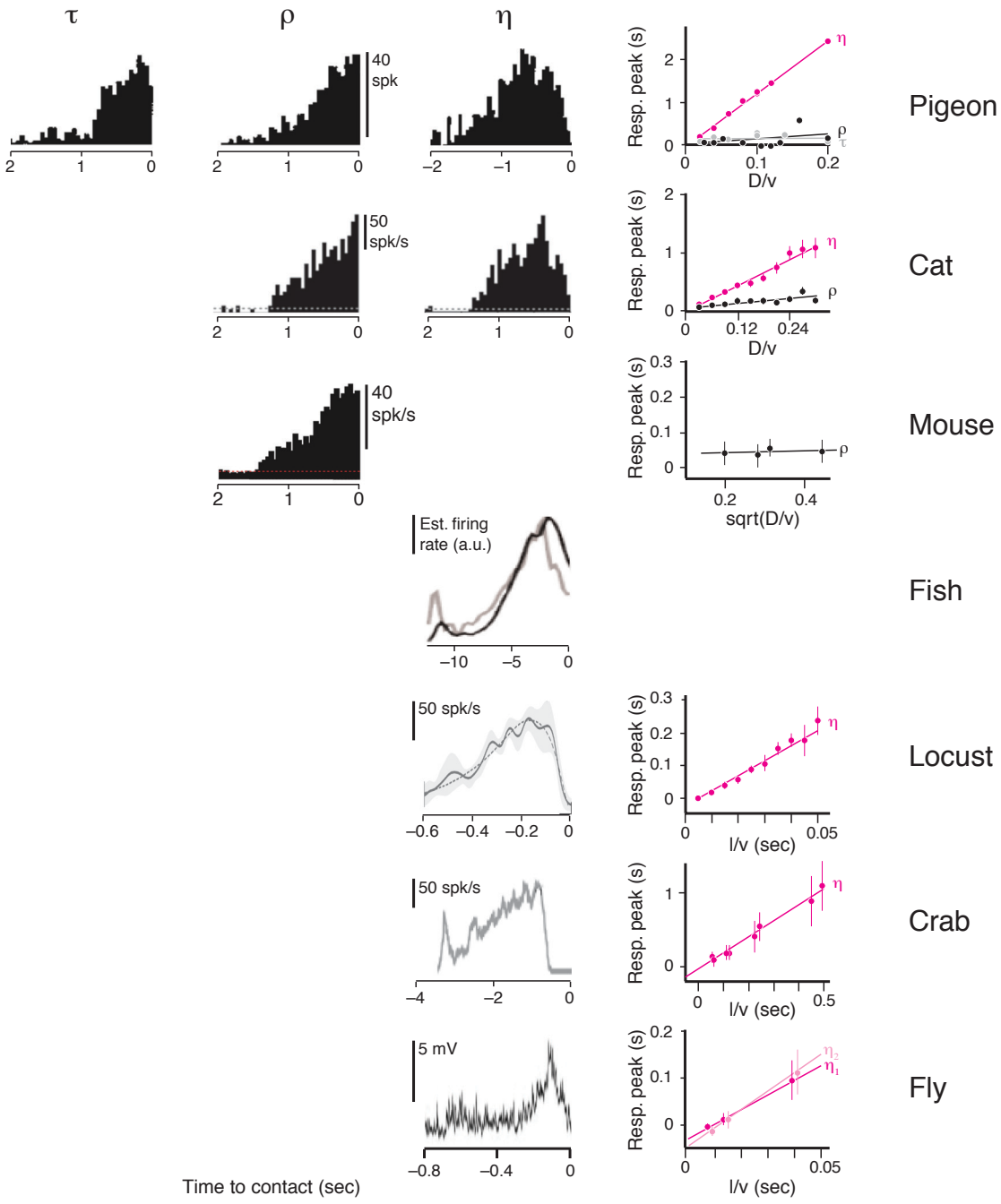

Figure 1.2: Identified Loom-Encoding Neurons Across Species
Cols 13: Examples from t, r or h neural response types identified in pigeon nucleus rotundus, cat superior colliculus, mouse superior colliculus, fish optic tectum, locust LGMD neuron, crab MLG1 neurons and fly giant fiber neurons. Col 4: Time-to-contact at peak neural responses (points) for each l/v tested. Linear fits with positive slope indicate that neurons peak at a threshold angular size, given by the slope of the line. Linear fits with slope = 0 indicate the peak occurs at a fixed time-to-contact. Data adapted from [53, 48, 39, 141, 108, 129, 92, 155, 52] Reproduced from [114].

1.2.2 Escape directionality

A critical feature of looming-evoked escape behavior is the control of escape direction to a directed stimulus. Understanding the underlying neural control is an area of active research. Directional escapes, also called escape trajectories, have been studied in many species [42, 34, 35, 25, 60], including crickets [146, 75], cockroaches [36], locusts [124], flies [23, 25] and fish [43, 39]. Research in species that use refuges in the wild, such as crabs that dig home burrows, report even more complex escape sequences that depend not only on threat orientation, but also distance to burrow and relative position of the ocean for offshore escape [161, 66]. In the lab, detailed studies in the zebrafish conclusively show that the laterality of response (right vs. left) is adjusted based on looming stimulus location [39] (Figure 1.3). In addition, mechanosensory stimuli presented at the head or tail alter the degree of bending of the body early in the behavior such that the fish swims away from the threat. This initial bending is dependent on the Mauthner array [91, 92]. To adapt escapes to stimulus direction and contextual cues demonstrates greater flexibility than previously thought available in highly stereotyped behaviors like escape.

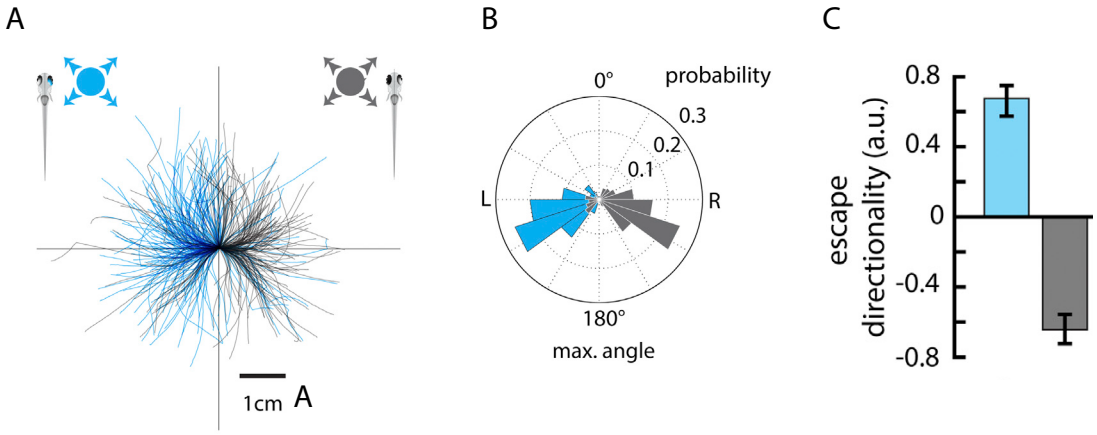

Figure 1.3: Directional Loom-Evoked Escape in Zebrafish
(A) Escape trajectories elicited by looming stimulus on the right (blue) or left (black) visual field, projected beneath the fish.
(B) Angular histogram of the maximum turn angle produced in the first 50 ms of the trajectories in A.
(C) Escape directionality plotted as a left-minus-right preference index, calculated by (left turns - right turns)/(left turns + right turns). Left and right loom stimuli consistently evoke lateral responses away from the stimulus position. Reproduced from [39].

1.3 Review of the Escape Behavior of Adult *Drosophila Melanogaster*

1.3.1 Fly escape is a sequence of distinct movements

Adult flies exhibit startle-induced locomotion in response to mechanosensory, olfactory and visual stimulation [164, 29, 152, 151]. In response to visual threats, flies will freeze, increase their walking velocity [56] or escape by initiating flight. Visually-induced escape is best studied in the context of looming stimuli [22, 61, 47]. Escapes are composed of a sequence of stereotyped actions that include freezing, leg repositioning with postural adjustment, wing raising and jumping with wing depression, shown in Figure 1.4. Flies perform rapid directional escapes, jumping away from the looming stimulus [23]. (Adapted from [60])

The fly's ability to orient its escape away from the looming stimulus direction is dependent on the postural adjustments and leg repositioning performed in its escape sequence. These serve to adaptively move the fly's center of mass in a manner dependent on the center of

looming stimulus expansion. The fly's escape trajectory is defined by the location of the center of mass relative to the position of its mesothoracic (middle) pair of legs that extend during jumping [23] (Figure 1.4). The neural substrates which underlie these movements in the escape sequence have yet to be determined.

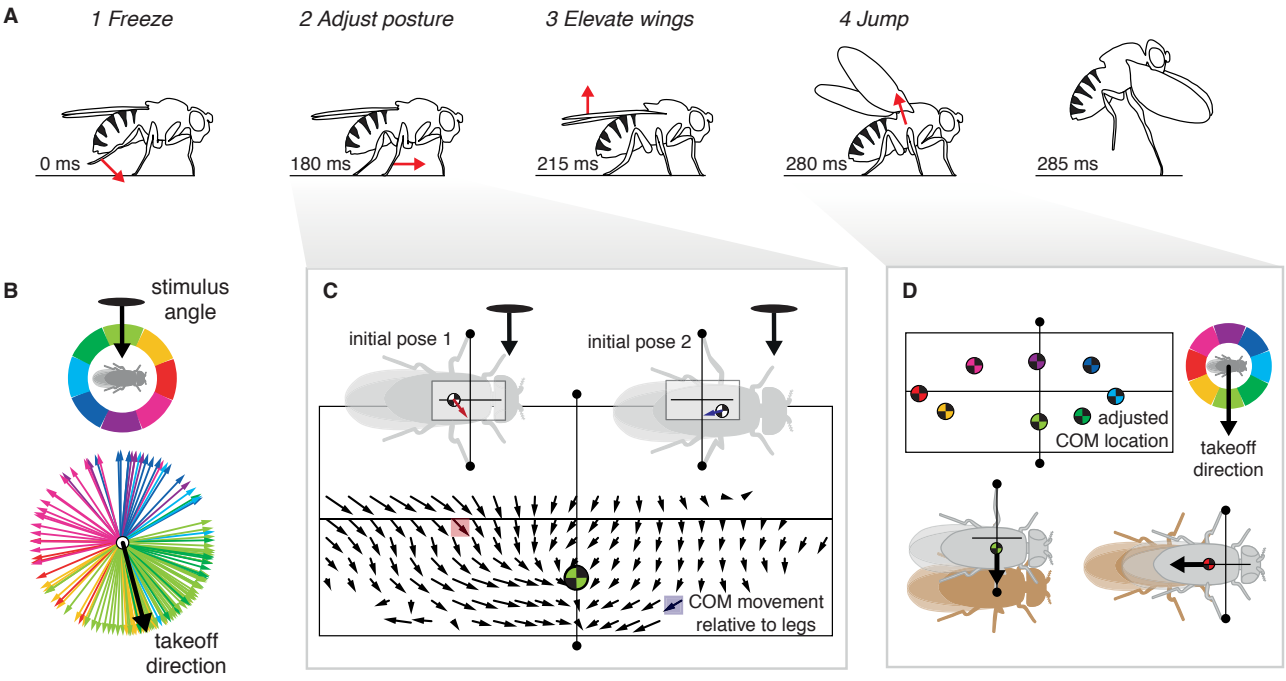

Figure 1.4: Fly Escape Sequence and Directionality
Fly escape is composed a sequence of behaviors which enable directional responses.
(A) Example escape sequence in response to a looming stimulus. The fly sequence is composed of: 1) freezing - placing all of its legs on the substrate and stopping movement, 2) leg repositioning - moving its legs to move its center of mass (COM) toward the escape direction, 3) wing elevation raising both wings in preparation of takeoff, and 4) jumping extending the middle legs and depressing the wings to start flapping flight.
(B) Flies escape away from threatening stimuli. The color codes for an angular range of stimuli. Responses represented by individual color coded arrows are distributed approximately 180° away.
(C) Postural adjustments are performed according to the initial pose of the fly relative to the stimulus. Two examples demonstrate two different COM shifts relative to their middle legs. A vector field represents the COM movement of many fly escapes.
(D) The flys escape direction is determined by the shift in COM, binned into eight color-coded ranges. Two examples schematize the COM shift (gray to brown) and the escape direction. Figure reproduced from [25].

1.3.2 The Giant Fiber system

The giant fibers (GFs), first described by Power in 1948 [120], constitute a pair of neurons in which a single action potential initiated in one GF drives bilateral wing depression and leg extension [155]. The giant fiber system (GFS), shown in Figure 1.5, contains known sensory inputs and downstream motor outputs. The characterization and development of the giant fiber system (GFS) has been reviewed in detail by Allen et. al [4]. First characterized in larger fly species, GFs project multiple dendritic branches in the central brain that synapse to neurons that co-fill with dye [9, 100]. Auditory receptor neurons in the antennae, called Johnstons organ neurons, of type AB, form electrical synapses with the GFs in the antennal motor and mechanosensory center (AMMC) [73, 133]. These inputs mediate mechanosensory responses [89]. GFs are also responsive to looming visual stimuli. One visual input is the lobula columnar cell type LC4 (also called ColA) [111, 102]. The dendrites of individual LC4 neurons tile and span the lobula, the 4th order visual neuropil of the optic lobe, and their axon terminals form a glomerular output structure that overlaps with GF dendrites. LC4 neurons co-fill with GFs in larger flies, and their connectivity has been demonstrated in Drosophila [156]. GFs may also take input from the giant commissural interneurons, which co-fill with dye. These neurons cross the central brain to link activity between the GFs, potentially imposing a bilateral activity pattern in GFs. Additional anatomical evidence suggests that GF axons are electrically coupled to each other in the ventral nerve cord, which could serve as a separate mechanism to match GF activity [118]. GF outputs have been well characterized anatomically [80] and downstream targets have been characterized electrophysiologically [145]. GFs project large axons down the cervical connective into the ventral nerve cord, where they form chemical and electrical synapses with the peripheral synapsing interneuron (PSI) and the tergotrochanteral muscle motorneurons (TTMn). The TTMns control mesothoracic leg extension. The PSI pair synapse to each other and to contralateral dorsal longitudinal muscle motorneurons (DLMn) which control wing depression. Thus, a unilateral or bilateral GF spike drives symmetric leg extension followed by wing depression to affect an escape.

(Adapted from [60])

Recent work by von Reyn et. al. [155], investigated the role of GF activity in escape behavior. High-throughput behavioral experiments showed a bimodal distribution in the duration of looming-elicited escape behaviors, measured from the start of wing raising to the moment of takeoff. Employing a split-GAL4 line [116] expressing only in the GFs, precise neural activation by CsChrimson [81] and inactivation via KIR2.1 channel hyperpolarization [10] revealed that GFs are necessary and sufficient for short duration escape behaviors. Although files perform long duration escapes without GFs, it is possible that GFs also contribute to this jumping component when they are available. Long duration escapes likely rely on unknown parallel looming-sensitive descending pathways that converge at the TTMn and DLMn. Somatic whole cell patch clamp recordings of GFs while monitoring flight initiation with high-speed videography showed that GF spike timing relative to unidentified pathways determines whether the fly performs a short or long duration escape behavior. (Adapted from [60])

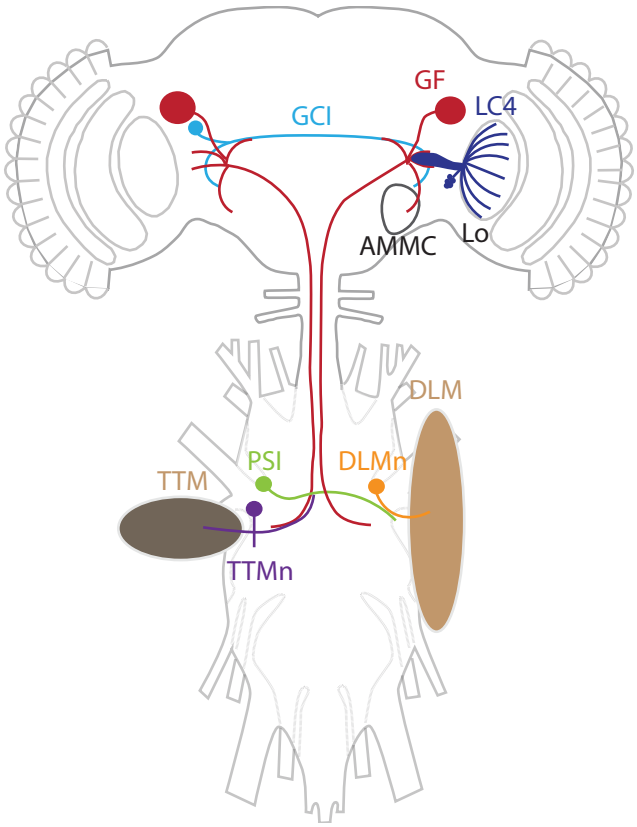

Figure 1.5: Giant Fiber System
Schematic of identified cell types in the giant fiber system (GFS) within the fly central nervous system. The GFS consists of a pair of giant fibers (GF, red) and their bilaterally symmetric inputs and outputs, shown here on one side only. GF inputs in the brain: giant commissural interneurons (GCI), lobula columnar neuron 4 (LC4; Lo indicates lobula), antennal motor and mechanosensory center (AMMC). GF outputs in the ventral nerve cord: peripheral synapsing interneuron (PSI), tergotrochanteral muscle motorneurons (TTMn), dorsal longitudinal muscle motorneurons (DLMn). The TTMn and DLMn output to their respective muscles, the TTM and DLM, that generate leg extension and wing depression in fly escape. Reproduced from [60].

1.3.3 Looming-sensitive visual neurons

Foma1 Neurons

Recent work in Drosophila has focused on characterizing looming-sensitive cells in the visual pathway. The enhancer trap line Foma1 was identified in a genetic silencing screen for optomotor deficits [76]. Included in the Foma1 neuronal expression pattern are a cluster of three neurons with broad dendrites in the lobula plate and 2 neurons with dendrites in the lobula. The lobula and lobula plate are neuropiles critical for motion detection (reviewed by [15]). Electrophysiological characterization demonstrated that a subset of Foma1 visual neurons are sensitive to looming stimuli. Activation of the Foma1 neurons with Channelrhodopsin2 generated escape behavior and silencing with temperature-sensitive Shibire strongly and significantly reduced escape to looming visual stimuli, indicating that Foma1 neurons, or a subset within, are essential for looming-evoked escape behavior [31]. (Adapted from [60])

LC4 Neurons

To understand the looming-sensitive visual inputs to the GF, von Reyn et. al. [156] studied the LC4 cell type [46, 111, 138]. There are 60-70 LC4 neurons per hemisphere, and their axons exit the optic lobe and project into the ventrolateral protocerebrum of the brain to form a large bundle called an optic glomerulus [140]. They comprise one of approximately 20 optic glomeruli, each formed from a distinct visual output cell type [113, 162]. The study determined that the GF lateral dendrite projects into the LC4 glomerulus and is functionally postsynaptic to LC4. Silencing LC4 and recording the GF shows that LC4 contributes to the looming speed sensitivity in the GF loom response. Furthermore, in behavioral experiments, activation of LC4 generate GF-like short duration escapes.

LPLC2 Neurons

Similar to the LC4 neurons, the LPLC2s are visual output neurons which form a distinct optic glomerulus and also provides input to the GF. Activation of LPLC2 also drives escapes [162]. Studied recently by Klapoetke et. al. [82], the LPLC2s themselves take input from both the lobula plate and lobula. The lobula plate contains outputs for directionally selective motion-sensitive small-field neurons called T4 and T5 that terminate in 4 layers, each corresponding to a cardinal direction. Anatomical analysis of the lobula plate dendrites showed a unique configuration in which cross-shaped dendrites ramified into each of the layers such that each branch detected outward motion from the neuron's receptive field center. Characterization by calcium imaging confirmed that LPLC2 is selectively responds to loming, and local inhibitory neurons selective for inward motion grant a high degree of specificity.

1.4 Tools for Neuroscience Research in *Drosophila Melanogaster*

In studying the sensorimotor processing underlying escape, the advent of precise neurogenetic tools in genetic model organisms allow dissection of neural function with precision not available in other animal systems. The basis for this technology in flies is the GAL4-UAS binary expression system, detailed below. Advances in this system allow repeatable identification and manipulation of specific genetically-defined neuronal cell types. In behavioral experiments, this allows both activation and silencing of specific cell types, which is an important tool revealing their behavioral roles.

Flies present other important practical benefits as well, including: relatively low maintenance costs for keeping large numbers of individual genetic lines, fast generational times for building particular genotypes efficiently and the ability to generate large numbers of genetically identical individuals to gain statistical power in experiments. [131]

1.4.1 GAL4-UAS binary expression system

The GAL4-UAS system [17, 38] is a widely-used genetic tool in fly research that confers cell-specific control of expression. By locating the site-specific yeast transcription activator GAL4 downstream of a genomic enhancer of an endogenous gene that expresses in particular neurons, GAL4 is expressed in those neurons. The UAS (upstream activating sequence) is located upstream of a desired responder gene. When GAL4 is expressed, UAS is activated, and the downstream gene is expressed. This scheme gives robust and consistent control of gene expression in neurons in which the genomic enhancer is active.

Selection of the downstream gene controls the type of experiment performed. Common downstream gene sequences are fluorescent reporters, such as GFP [131], which identifies the particular neurons under genetic control. Neurons can be silenced through the expression of TNT or KIR2.1 constructs [10] which are used to identify loss-of-function behavioral or physiological phenotypes. For gain-of-function experiments, neurons may also be optogenetically activated by expression of light-gated ion channels such as ReachR [70] or CsChrimson [81], in combination with an appropriate light pulse.

Alternative and complementary binary expression systems have been developed, such as the LexA-LexAop system [19, 87], which allows independent control of two populations of cells. For example, for a functional connectivity experiment, CsChrimson can be expressed in a putative upstream cell type with the GAL4-UAS system while GFP can be expressed in a putative downstream cell type to target an electrophysiological recording. This scheme allows experimenters to repeatably test if activity in the first cell type drives recorded downstream activity, indicating that they are functionally connected [82]. There are many schemes, including epistasis experiments which can be employed using two binary expression systems.

Spatial refinement of the GAL4-UAS expression pattern can be achieved by the split-GAL4 technique [93, 116]. By driving GAL4's DNA binding and activation domains under separate enhancers, via a leucine zipper, GAL4 function is only reconstituted in neurons belonging to both expression patterns. By searching for multiple GAL4 expression patterns

for a cell type of interest, generating split-GAL4 combinations of pairs of these patterns, and selecting resulting lines in which only the cell type of interest lies in the expression intersection. This allows for highly-specific control of genetic expression if successful intersections can be generated.

The generation of cell type-specific split-GAL4 libraries is an incredibly powerful tool for precisely investigating individual elements of neural circuits [33]. The number of existing GAL4 halves has been sufficient to develop split-GAL4 libraries that cover many of the individual cell types in particular anatomic regions of the fly brain, such as the fly optic lobes [154, 162], mushroom bodies [6, 8], central complex [160] as well as the DNs [106]. These collections are both an anatomical catalog of cell types as well as a resource for further functional investigation.

1.4.2 In vivo whole-cell patch clamp electrophysiology

Progress in genetic control of cell type expression has been complemented by recent advances in fly electrophysiology. Preparations for somatic whole-cell patch clamp recordings were initially developed by Turner and Wilson for study of the olfactory system[159], and further engineered to be able to address state-dependent changes in activity while walking [28] and in flight [94]. These experiments can leverage the cell type-specific reagents by targeting fluorescent labeled somata with patch electrodes [104]. In this paradigm, experimentalists are confident that the recordings profile a specific identified cell type in each fly, without requiring post hoc identification through either an effective anatomical dye fill from the patch electrode or a match to the response profile of an identified cell type. This simplifies and improves consistency in electrophysiological characterization within a set of experiments and enables straightforward future examination of previously studied cell types.

1.5 Thesis Research Direction and Scope

An ongoing challenge in studying neural circuits and behavior is determining how to assess functional roles for putative parallel sets of neurons that may contribute to the same behavior. These circuits are difficult to dissect because additional neurons may have redundant functions, which make predicting the behavioral output difficult in perturbation experiments. With current technology, it is possible to activate or silence target neurons in a cell type-specific manner [132]. These are also referred to as gain of function or loss of function experiments. In a system where activity in two or more neurons can generate a particular behavior, silencing any single neuron may not reveal a deficit when presenting a stimulus that naturally elicits that behavior. Furthermore, if many neurons are naturally active in performing a behavior, inducing activity in a single neuron may not be sufficient to generate the behavior, and the conclusion that the neuron drives the behavior will be shrouded. In escape systems, since many pairs of DNs may be coactive during the same threatening stimulus, it can be difficult to observe differences associated with eliciting or blocking activity in a single pair.

I worked with my colleague, Ryan Williamson, to tackle the behavioral detection side of this problem. We developed the FlyPEZ, a flexible experimental tool which is able to distinguish minute differences in escape and other behaviors. The FlyPEZ efficiently produces high-speed videos of fly behavior with high spatial resolution. If different DN cell types drive similar but not identical motor patterns, we can use the FlyPEZ to differentiate their contributions. Chapter 2 consists of a manuscript, now in press, with full details on the development, usage and proof-of-principle of the device.

In chapter 3, I present a project exploring the role of a group of DNs in fly escape. These DNs are anatomically parallel pathways to the GFs. Using the FlyPEZ, I determined that, like the GFs, certain DN cell types drive escape. In electrophysiology experiments, I find that each of these DNs are strongly responsive to threatening visual stimuli. This indicates that they are co-active when flies are confronted with approaching predators. Further behavioral

analysis indicates that two DNs drive postural adjustments which lead to forward or backward escapes. Finally, analysis of connectivity between LC4 and these DNs in an electron microscopy dataset reveals spatial biases consistent with generating an appropriate escape direction. Overall, I found a functional group of DNs that serves as part of the feed-forward descending control of the fly escape sub-behaviors.

Finally, in chapter 4, I will discuss future directions, ideas, and questions raised but unanswered during these projects. In particular, there are a number of speculative thoughts relating to the DN project in chapter 3 that are recorded for future fly escape and descending control aficionados.

CHAPTER 2
THE FLYPEZ: RAPID BEHAVIORAL PHENOTYPING OF AUTOMATICALLY ISOLATED DROSOPHILA AT HIGH RESOLUTION

2.1 Chapter Overview

We developed the FlyPEZ as a tool to automate fly behavior experiments. The throughput allows population sampling at a range of stimulus parameters, which is critical to understand behavioral variability and contextual dependencies. Although I used the FlyPEZ for studying control of escape behavior by a set of descending neurons, it can be used for a range of fly behavior experiments. We believe that the method could be useful in the research community, so we put together a paper which includes a characterization and demonstration of the FlyPEZ's capabilities. This chapter is adapted from a manuscript submission for journal publication. The name, FlyPEZ, references a candy container which dispenses a single small tablet when opened, and is reminiscent of the FlyPEZ's ability to separate individual flies from a group.

2.2 Abstract

Sparse manipulation of neuron excitability during free behavior is a critical tool for identifying neural substrates of behavior. Genetic tools for such manipulation exist in the fruit fly, *Drosophila melanogaster*, but detecting the resulting, potentially precise, behavioral phenotypes in this small animal requires a high-throughput assay with high temporal and spatial resolution. Here, we introduce FlyPEZ, which achieves these aims by automatically releasing flies one-at-a-time onto a small platform for targeting by visual stimuli, optogenetic lights, and high-speed video cameras. FlyPEZ provides the resolution to track individual appendages with a throughput of thousands of flies per day. Its modular components can

also easily augment other assays. We use FlyPEZs capabilities to demonstrate a novel role for head casting during unrestrained optomotor responses, comprehensively model the input-output function for directional looming-evoked escape takeoffs, and discover a new, millisecond timescale loss-of-function phenotype from genetic silencing of a single visual projection neuron type.

2.3 Introduction

To understand how neural circuits coordinate movement and control complex behaviors, it is advantageous to perturb activity in sparse neuronal subsets while observing the behavioral consequences [62, 122, 158], ideally during natural behaviors. Recently available neuroanatomical information and corresponding genetic reagents available in the fruit fly, *Drosophila melanogaster*, have refined the spatial [71, 116] and temporal [11, 70, 81] targeting of such neuronal manipulations, offering an unprecedented opportunity to link neuronal activity in identified cell types to behavior. However, such precise manipulations often require equally precise measurements of behavior to detect their effects. In particular, activity in individual neurons is known to affect the timing, extent, or direction of movement for individual appendages such as the legs [98], wings [127], or proboscis [128], which can only be seen by camera systems with high spatial and temporal resolution. Phenotypes have also been shown to vary depending on the sensory [1], social [121], and behavioral [28] context in which the animal was observed. Furthermore, data from tens or hundreds of thousands of individuals may be required to discern phenotypes, because behavior of freely moving animals and genetic expression are inherently variable [116, 122] and thousands of sparse-expression lines may need to be screened. The quest to link sparse neuronal manipulation to free behavior phenotypes therefore requires a high-resolution, high-throughput assay in which environmental variables can be controlled. State-of-the-art methods for recording large numbers of flies use planar arenas to study groups during walking or standing behaviors [18, 130]. This has been a successful approach for classifying a wide range of behaviors [13, 56, 72] and using sta-

tistical approaches to map them in an unbiased manner to neurons whose activity may affect them [7, 21, 67, 69, 122]. However, arenas are limited in external stimulus precision and flexibility, and cannot control influences from other flies. Furthermore, because the camera must be mounted far above the flies to encompass the entire arena in its field of view, most current large-arena systems cannot resolve appendages, and are limited to two-dimensional tracking, in which some appendages may be occluded. Higher spatial resolution can be achieved by isolating individuals in smaller arenas (e.g. [13, 119, 134]), including courtship chambers [30] or small mazes [20]. Isolation comes with the additional benefit of eliminating the influence of uncontrolled social interactions on behavior, and a smaller area makes it easier to target the fly with external stimuli. But in these cases, individuals must be loaded into each chamber, and the time required to manually process each fly drastically limits throughput. Automated means to manipulate single flies into specialized assays are emerging [2, 125] and have the potential to bring high-resolution, single-fly assays into the high-throughput realm. However, current methods use air pressure or robotic arms to forcibly move flies around, thereby introducing an external stimulus that may perturb the flies, alter their behavioral state, or mask experimental phenotypes [12, 149]. Such manipulations are especially problematic for studying behaviors in response to visual stimuli because the robot arm movement itself becomes a salient visual stimulus to which the fly is exposed, potentially habituating [45, 126] or facilitating [167] responses during the experiment. Such applied-force automation is thus best suited to experiments where animals are given a long recovery period between fly handling and experimental protocols, a period that itself reduces throughput. Here we present an alternate approach that overcomes these challenges to assaying natural behavior with simultaneous high-resolution and high-throughput. The FlyPEZ system automatically isolates individual flies on a small platform, without undue perturbation, where they can be targeted for visual or optogenetic stimulation and their responses recorded using a macro lens on a high-speed camera. FlyPEZ is modular and consists of three novel components, each of which are affordable and can operate in stand-alone fashion. FlyGate is a 'smart'

gate that separates individual flies walking upwards by negative geotaxis out of a standard fly vial [54]. Negative geotaxis has previously been used to successfully remove groups of flies in bulk from a vial without perturbation [125, 155], however by adding a linear photodetector array and a motorized gate calibrated to stop flies without squishing them, we are able to control their release rate and isolate them one-at-a-time for experimental stimulation. FlyDetect, is a template-matching 3D-tracking algorithm that precisely locates either the anterior or posterior end of the animal to determine the flys center of mass and orientation, even if half of the animal is occluded. GlobeDisplay is a spherical screen surrounded by a custom conical mirror onto which a single projector can display images that cover nearly the entire visual field of the fly. The integrated FlyPEZ system can quantify a wide range of unrestrained behaviors in detail with a throughput appropriate for running forward genetic screens, including screening collections of driver lines targeting single neuronal cell types. As a proof of principle, we demonstrate the FlyPEZs ability to quantify millisecond movements of the head, wings, and legs of thousands of flies during visually-evoked innate behaviors, and we harness this capability to identify distinct roles for different visual projection cell types in coordinating looming-evoked escape. We also provide examples of a range of other behaviors, including grooming, courtship, and proboscis extension, that can be observed with the FlyPEZ, and we show the system can be adapted to automatically make repeated measurements of the same individual, enabling the study of learned behaviors. The FlyPEZ system thus provides the flexible components needed for extracting high-resolution behavioral information from large populations of individually-measured flies, making it possible to quantify fly behavior at the level of detail required to identify functional roles for single cell types, in the context of unrestrained behavior.

2.4 Results

2.4.1 Implementation of FlyPEZ

FlyPEZ comprises three separable but integrated modules (Figures 2.1A, 2.2A): a fly dispenser (FlyGate, Figures 2.1B, 2.2B), a custom tracking algorithm (FlyDetect, Figures 2.1C-D), and a surround visual display (GlobeDisplay, Figure 2.1E). To begin an experiment, the user inserts a vial of flies into a spring-loaded holder under the FlyPEZ and scans a barcode that loads previously entered experimental parameter data into a graphical user interface written in MATLAB. The rest is automatic (Figure 2.2C).

FlyGate, the fly dispenser module, first automatically separates individual flies from the vial group. Flies exit the vial voluntarily by negative geotaxis and funnel into a tunnel just wide enough for a fly to walk forward (Figure 1B). In the tunnel, an IR laser light shines through a thin vertical slit in the tunnel wall, illuminating a linear photodetector on the opposite side. A fly in the tunnel occludes part of this light, creating a shadow that indicates its location (Figure 2.2D-E). When the fly shadow reaches a designated tunnel height, an onboard microcontroller signals a servomotor to close a small plastic gate behind the fly, preventing passage by subsequent flies. A gate in the 'Blocked' position is precisely calibrated such that, on the rare occasions when the gate closes on a fly, the impinged fly is not damaged (Figure 2.2F). Flies exiting the tunnel emerge on the recording platform, a 5 mm X 5 mm glass square adjoining the tunnel exit. Water surrounds the platform to prevent flies from walking away (Figure 2.1B). The small platform size keeps the fly centered in the visual panorama and the focal regions of both the camera and optogenetic-activation lights.

FlyDetect software monitors the platform via real-time video input from two small, angled mirrors that periscope orthogonal views of the fly down to a camera (Photron, San Diego, CA) sampled by a computer at 15 Hz. One mirror, positioned beneath the glass platform, delivers a ventral view of the fly (Figure 2.1C, bottom inset video frame) and another, facing platform front, delivers a side view (Figure 2.1C, top inset).

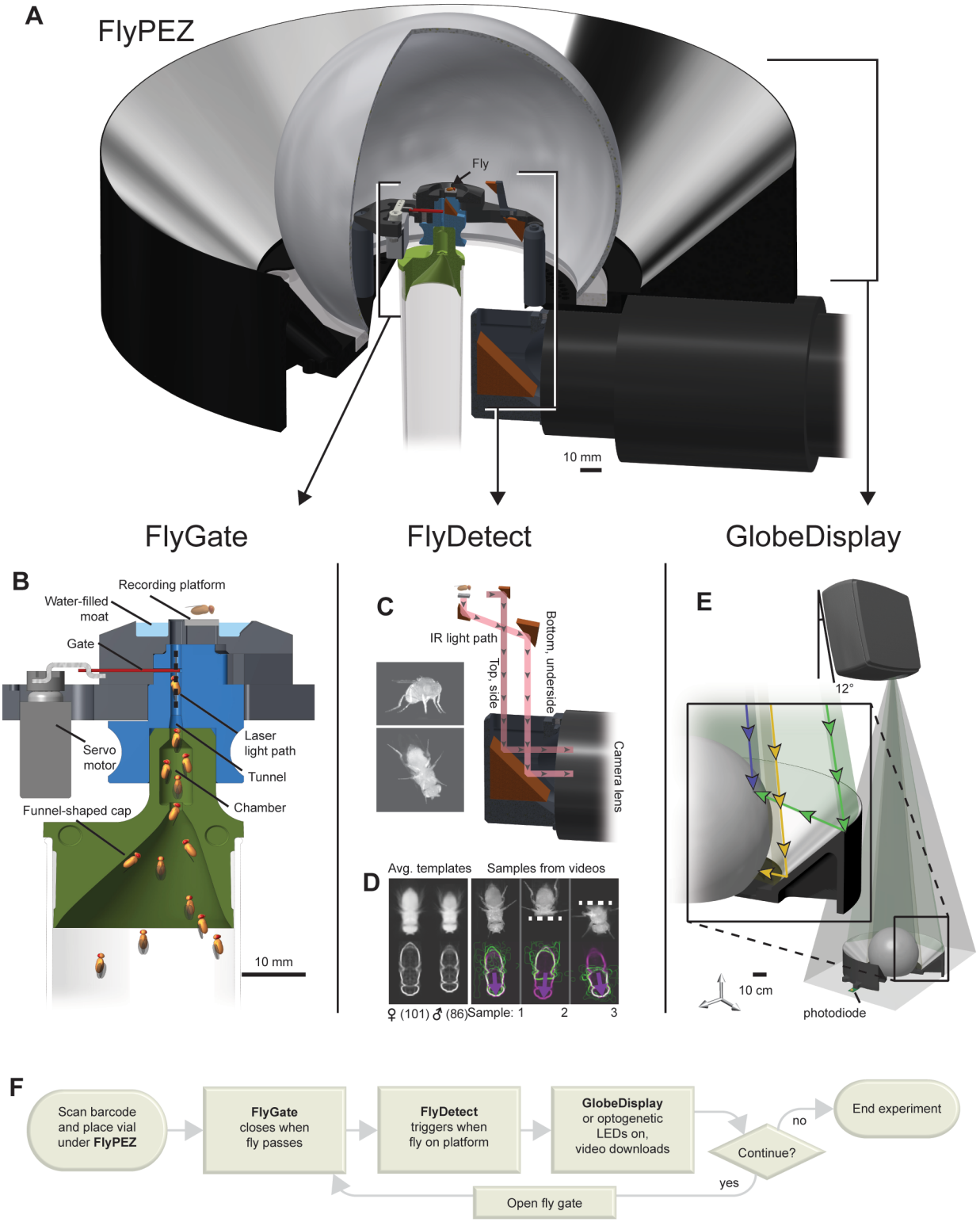

Figure 2.1: Implementation of FlyPEZ

Figure 2.1 ***(previous page)*****: Implementation of FlyPEZ**
(A) The FlyPEZ system comprises three separable but integrated modules: FlyGate, FlyDetect, and GlobeDisplay. Diagram view sectioned to reveal FlyPEZ interior.
(B) The FlyGate module (shown in cross-section) includes a funnel-shaped cap that is inserted into a standard fly vial (green), a removable plastic tunnel (blue) that contains a laser light sheet and linear photodetector, the gate (red) attached to a servo motor (grey), and a 5 mm X 5 mm glass recording platform (light gray).
(C-D) The FlyDetect algorithm finds the center of mass and heading of flies in real-time and posthoc analyses, even when the fly is partially occluded. It takes as input video frames acquired via four small mirrors that direct two perspectives of the fly onto a single camera lens such that both orthogonal views of the fly are simultaneously recorded in focus (C). To generate the templates used for tracking (D), images of ∼100 flies were aligned and averaged (female and male, left). Separate templates for the anterior and posterior ends of the flies were then generated.
(E) Model of the GlobeDisplay panoramic visual stimulus module, including projector, plastic spherical screen, and surround conical mirror. The projector is angled 12° to compensate for the optics which were designed by the manufacturer to project an elevated picture onto a wall. The inset shows how the reflected portion of the image (green) intercepts the directly projected portion (blue).
(F) Flow chart of a typical FlyPEZ experiment. See also Figures 2.2, 2.3, 2.4.

Four infrared (850 nm) light emitting diodes (LEDs) provide illumination for the camera outside the flys visual range [99] (Figure 2.2D). FlyDetect is a custom tracking algorithm designed to work specifically with the small FlyPEZ platform, where the fly may at times overhang the edge and become partially occluded in the bottom camera view. The algorithm uses template-matching to locate the flys anterior ('head') and posterior ('tail') halves separately in each video frame. From these, FlyDetect determines the flys whole-body center of mass and anterior-to-posterior heading (Figures 2.1D, 2.3A-F). A final refinement step used in post-hoc tracking analyses, but not in the real-time data acquisition, aligns the edges of the template with specific features of the tracked fly, thereby increasing the tracker accuracy (Figure 2.3G, also see Methods). As this approach works by partitioning the fly into segments, it can also be applied to individual appendages, for example, to track head movement relative to the body (see Figure 2.8).

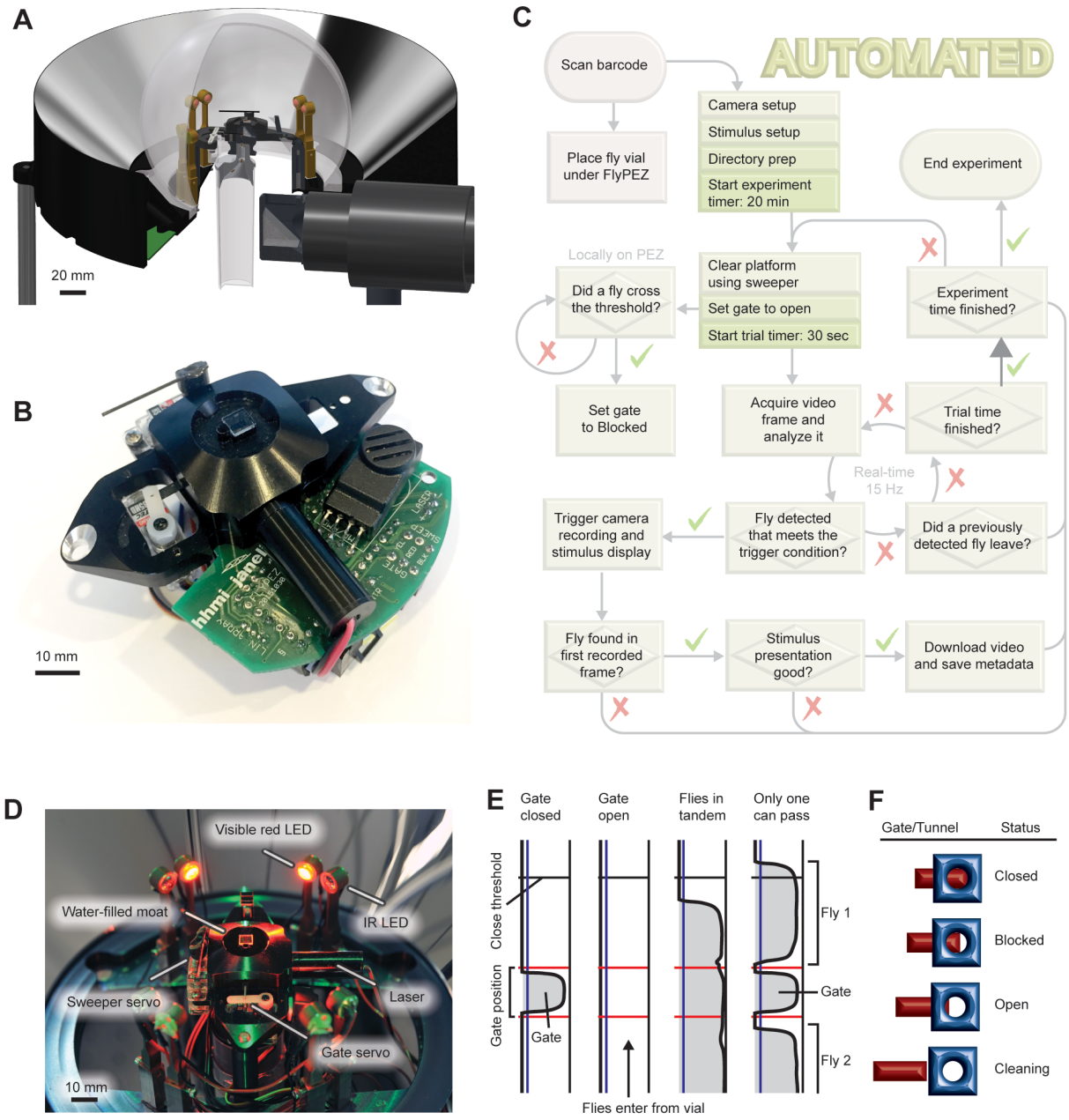

Figure 2.2: Implementation of FlyGate

Figure 2.2 ***(previous page)*****: Implementation of FlyGate**
(A) Section view of FlyPEZ base as in Figure 2.1A but including more detailed parts, such as the IR and optogenetic LEDs (copper color) and sweeper (black).
(B) Photo of stand-alone FlyGate module, capable of functioning independently. The part includes an on-board microcontroller and custom circuit board.
(C) Detailed flow diagram of a typical experiment from start to finish. The only manual steps include scanning the barcode and securing the fly vial underneath the FlyPEZ.
(D) Close-up photograph of the FlyPEZ with the spherical projection screen removed showing the interior parts.
(E) Four examples of the output of a linear photodetector array that is used by the on-board FlyPEZ microcontroller to determine the location of the gate and flies inside the tunnel. This output is also displayed in real-time in the FlyPEZ graphical user interface. Horizontal amplitude of the bold black line is proportional to the amount of light detected from a laser directed at the array through a slit. A closed gate blocks most of the light at the gate location. Flies traversing the tunnel also block the light, and when enough light at a set position past the gate is blocked, the servo controlling the gate is set to the 'Blocked' position to prevent the passage of subsequent flies.
(F) Model of gate positions, as viewed downward through the tunnel. 'Closed' completely blocks the laser light and is used for finding the gate position with respect to the linear photodiode array. 'Blocked' is closed enough to block passage of flies while leaving enough room to prevent crushing a fly passing the gate. 'Open' creates enough space for a fly to pass while preventing the passage of two flies in tandem. 'Cleaning' releases the tunnel piece for quick cleaning if debris is blocking the passage, which occurs approximately once every 4,000 flies.

To assess tracking accuracy, we compared the heading and center of mass location output by the algorithm to manual tracking of these parameters in 1151 frames selected from videos of 215 different flies (Figure 2.3H-J). The automated tracking is 95% accurate to within an equivalent of 4% the length of the fly and can track 94% of the downloaded videos (Figure 2.3K). When a fly arrives at the platform center with rotational velocity below 150°/s, FlyDetect signals experimental stimulation to begin and the camera starts recording. The triggered stimulus can be either optogenetic stimulation with four red (624 nm) LEDs or a pre-rendered visual stimulus movie using the GlobeDisplay described below. GlobeDisplay software rotates the projected stimulus to display relative to the flys frame of reference using the real-time orientation of the fly determined by FlyDetect. After every triggered recording, a motorized bar sweeps the platform area to clear any remaining flies, and FlyGate opens to start another trial.

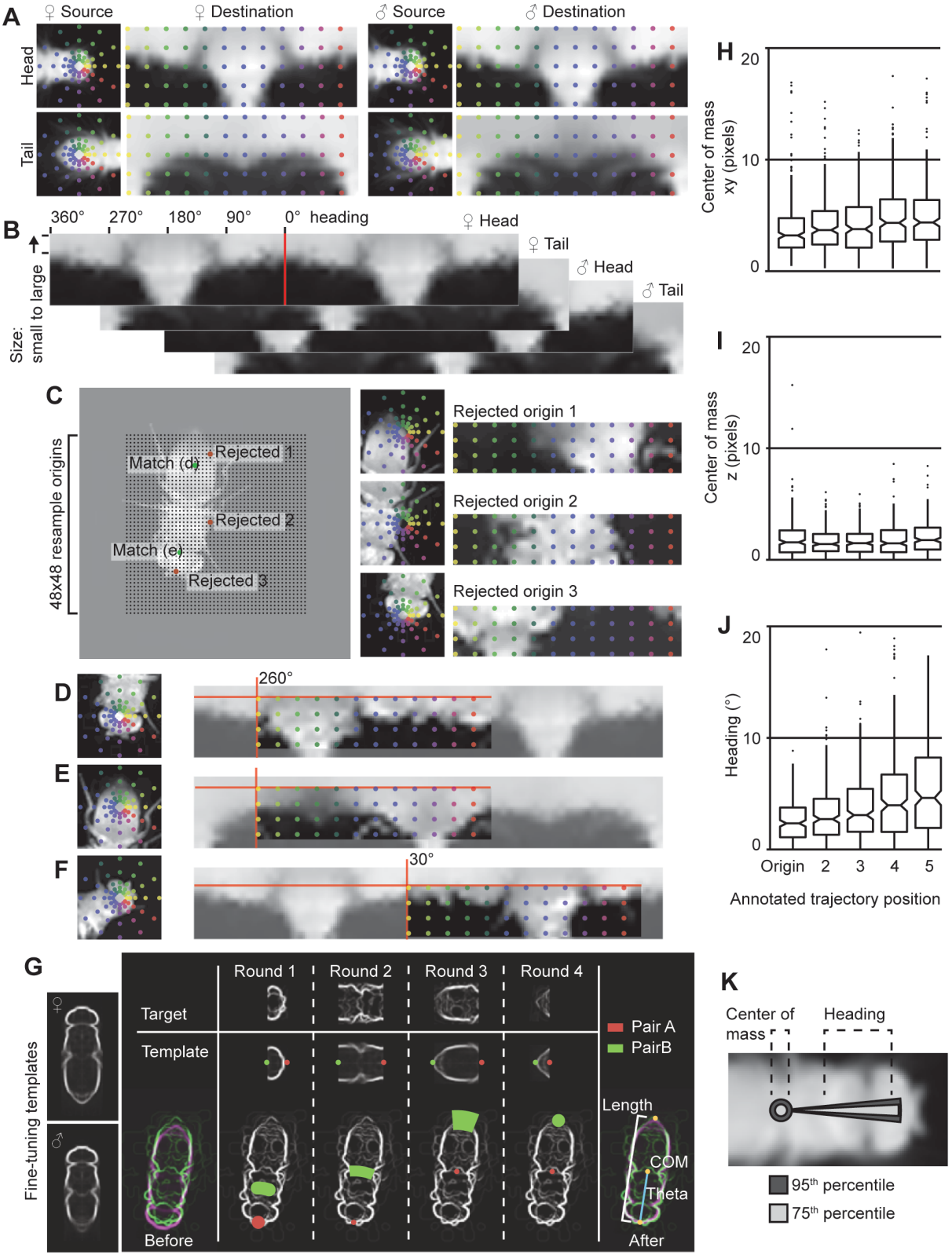

Figure 2.3: Implementation of FlyDetect

Figure 2.3 ***(previous page)*****: Implementation of FlyDetect**
(A) Using the average fly depicted in Figure 1D, a template is generated by radially resampling either the anterior or the posterior ('head' and 'tail' are used for convenience) region of both females and males. Including separate male and female templates improved tracking accuracy, although the tracker does not reliably identify gender. For reference, each colored point on the original image (left, source) corresponds to the same color point on the resampled image (right, destination). This transformation is rapid using MATLAB because the 'Destination' image is generated only by referencing (or 'indexing') pixels in the 'Source' image, as opposed to the slower approach of transformation via interpolation. Other approaches deal with size variation by rescaling the image, but in this approach, the 'Source' image is indexed in a non-linear manner using spokes which radiate from the center while the corresponding points in the 'Destination' are evenly spaced. Therefore, the x-axis of the 'Destination' image represents size while the y-axis represents image rotation.
(B) To ensure that a match can be found regardless of the orientation of the fly in a video, templates are constructed from two duplicated 'Destination' images from (A) positioned side-by-side.
(C) To locate a fly within a video frame, the program tests for the presence of a head or tail at multiple locations (left, 48 x 48 grid of black dots overlaid). At each location, the image is resampled in a similar way as described in (A), but this time using fewer points per spoke. The resampled image is then compared to the four template images in (B) and the coefficient of determination (r^2) is determined. A 'match' is the location having the highest r^2 value, if that value exceeds the empirically determined threshold of 0.33. All other locations are rejected. (D-F) For three example frames, the 'Destination' fly image is overlaid with the template in the best match location. The fly in (F) has a different orientation compared to that in (D) and (E), resulting in a shift along the template x-axis, and is smaller, resulting in a shift downward compared to the other examples.
(G) To refine the match, a new template is used which enhances the edges of the fly template. Starting at one extreme end of the fly, the edges template is fit onto the fly in the video using interpolated transformations, a slower process. For jump direction tracking, this is only done for frame one. For optomotor response data, when separate head tracking is desired, this is done for all frames. Fly heading is defined as the average heading of the three 'rounds' having the best fit. To visualize the quality of the fit before and after this refining procedure, the template in green is overlaid with the fly in magenta such that the outlines turn white when aligned. Note that more of the outline appears white in the 'After' panel compared to 'Before'. (H-J) Tracking accuracy was assessed by comparing human annotations of high-speed FlyPEZ videos to automated ones. Using a MATLAB program, an experimentally blind human clicked on the extreme ends (head and tail) of five evenly spaced frames for trajectories of 215 flies that moved at least 50 pixels without any occlusions. Distances were measured as Euclidean distance in pixels. The average of the head and tail points defines the center of mass xy position (H) and the heading is the anterior direction of that vector (J). For the z-axis, the upper and lower bounds of the fly viewed from the side were annotated by hand, and the midpoint between these was compared to the tracking (I).
(K) Tracking confidence visualized by overlaying it onto an average fly.

To capture the flys fastest action, a 3-ms escape jump [24, 153], we record at 6000 frames per second and use a 105 mm lens (Nikon, USA) with 12-mm extension tubes, for a spatial resolution of 50 pixels/mm. Under these conditions, a fly jumping at speeds of 0.3 m/s travels 2.5 pixels per frame, which is appropriate for tracking with FlyDetect. The temporal and spatial scale of a recording is easily matched to a specific behavior by adjusting camera parameters.

GlobeDisplay projects panoramic images for the visual stimulation of fly behavior on trials for which the experimenter selects a visual stimulus. Similar to a smaller spherical projection system for tethered flies[136], GlobeDisplay achieves nearly complete coverage of the flys visual field (360° azimuth, 90° to -30° elevation) from a single light source by stitching together a portion of the image that is projected directly onto the sphere (zenith down to 30° elevation) with a portion reflected off a mirror onto the side of the sphere (-30° to 30° elevation)(Figures 2.1E and 2.4A-C). In contrast to the smaller display, managing reflections onto our larger, 6-diameter globe screen required a novel, machined mirror shape, an approach also used in vertebrate virtual reality systems [63]. In this case we designed a conical mirror to surround the globe at its base. Flies view projected images from the inside of the globe, at its geometric center, where the platform is located (Figure 1A). The custom-manufactured plastic globe assembly (TRU-PLASTICS, Sturtevant, WI) is coated on the outside with rear projection paint (ScreenGoo, Goo Systems Global, Ontario, Canada). A projector with its color wheel removed (DepthQ WXGA 360, Lightspeed Design, Bellevue, WA; with modifications designed by A. Leonardo) displays movie frames at 360 Hz, faster than the flicker-fusion frequency of the fly visual system [144]. Visual stimuli are pre-generated as a sequence of two-dimensional grayscale images representing objects in terms of azimuth and elevation (Figure 2.4A) and subsequently warped onto the globe screen (see Methods and Figure 2.4B-D). A one-time calibration procedure ensures the projection is centered on the globe and that projections are transformed as expected (Figure 2.4D).

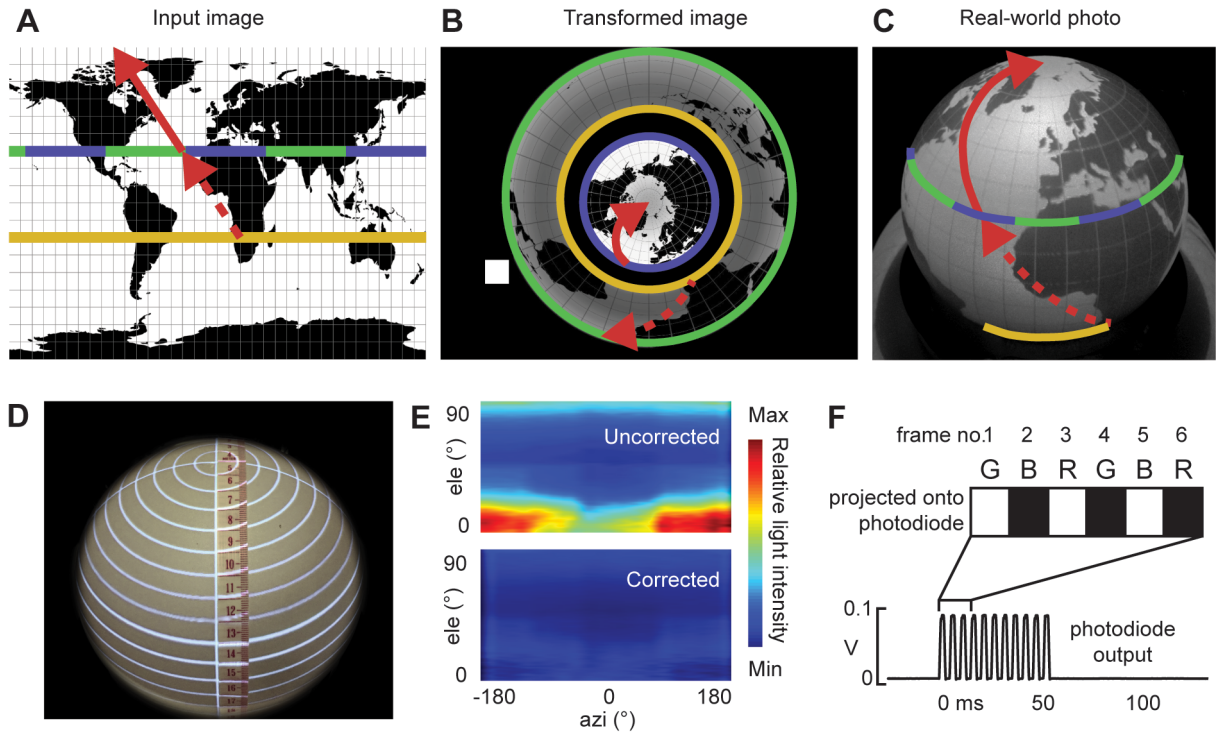

Figure 2.4: Implementation of GlobeDisplay
(A) Visual stimulus frames are generated as a 2D Mercator projection in terms of azimuth and elevation, just as earth is typically represented on a flat map. Overlaid colored lines show the same relative locations in A-C.
(B) A geometrical Image transformation is accomplished on the GPU in real time using the Psychophysics Toolbox, an open source OpenGL wrapper for MATLAB. The small white square in the lower left represents the position where the image flickers black and white with every stimulus frame over a photodiode to capture stimulus timing.
(C) A photograph of the GlobeDisplay with the input image from (A) projected onto it. (D) As part of the calibration procedure, latitude lines are displayed with a 10 cm spacing. The lines are then compared to a tailors tape measure to confirm that the displayed image matches the desired geometry.
(E) Brightness is corrected empirically, such that the image displays on the spherical projection screen with uniform light intensity.
(F) To identify trials in which frames were dropped, a square outside the image flickers from white to black with every frame at 360 Hz. This generates a square wave photodiode signal that is digitized by a NIDAQ board with its clock synchronized to the camera. After an experiment is complete, automatic raw data processing determines the frame on which the stimulus began and whether frames were dropped.

To ensure light levels across the globe are consistent from the perspective of the fly, a custom manufactured device positioned at the platform location was used to scan the inside of the globe screen with a photodetector. Brightness levels across the dome were then empirically corrected based on these measurements. This correction compensates for both the varying angle of incidence of the light on the spherical screen and the focusing effect of the mirror (Figure 2.4E). While the mirror does induce some variability in spatial resolution of images on the globe, the minimum spatial resolution is one degree, well below the minimum detectable by *Drosophila* [65]. Images are displayed with accurate timing using the Psychophysics Toolbox [16, 83, 115], an open-source software package for MATLAB. Stimulus frame presentation is monitored during an experiment using a photodiode outside the spherical projection area (Figure 2.4F). Unavoidable occlusions from the optogenetic and IR LED lights inside the globe near the horizon were minimized by design, occupying less than 2% of the flys field of view and reaching a maximum elevation of 5°. Also, the small number of flies retained by the globe during an experimental session each occupy less than 0.5° on the flys eye, below the flys spatial resolution, and are removed after each 20-minute run.

To further enhance the throughput capacity of the system, we designed several automatic data quality checks into the system flow. The longest duration event of each trial is the download of the video from the camera to the computer (20-40 seconds). To eliminate time wasted downloading unusable videos, each video and stimulus photodiode trace are automatically screened before download to determine if they pass quality checks (only one fly on the platform, no stimulus frames dropped, etc.).

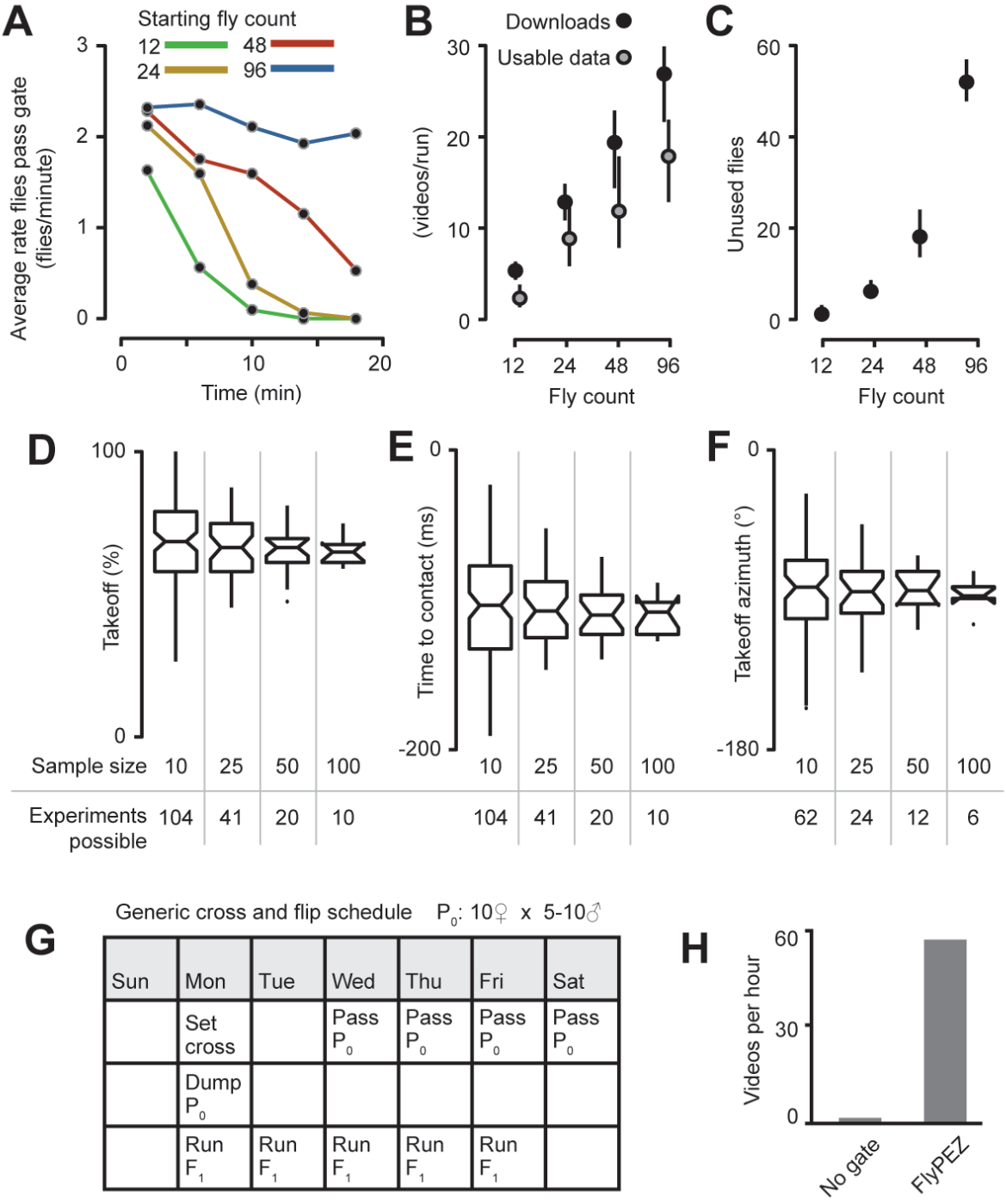

Figure 2.5: FlyPEZ Quantifies Single Fly Behavior with High Throughput

Figure 2.5 ***(previous page)*****: FlyPEZ quantifies single fly behavior with high throughput**
(A) We measured the instantaneous FlyPEZ throughput rate over a typical 20-minute experiment for fly vials of varying density (n = 12, 24, 48, or 96 flies; N = 8, 8, 8, and 7 vials, respectively). Shown are the number of flies passing the gate and triggering a blocked state in 4-minute bins. Densities of 96 flies produced a steady rate of ∼2 flies/minute exiting the vial and passing the FlyGate for the entire experiment. We attained a similar density in our experiments by crossing 10 males with 5-10 females (see G).
(B) Median number of videos downloaded per run (black) and median number of usable videos that pass manual curation (gray) per 20-minute experiment.
(C) Number of flies remaining in the vial at the end of the experiment. Vertical lines indicate inner quartile range.
(D-F) Box plots showing how a result would change depending on how many data points were collected. This relates to the consistency of the FlyPEZ and to the variability in fly behavior. Experiments were performed twice a day using the DL fly stock and the same visual stimulus (l/v = 40, 45° elevation, 45° azimuth) for 45 days. The total sample size of 1089 was then divided into groups of 10, 25, 50, and 100. This comparison highlights the tradeoff between the number of experimental conditions obtainable in a set amount of time and the statistical power of the results. For (D) and (E), N = 1089 flies; for (F), N = 651 flies.
(G) Fly handling schedule that can be followed to obtain a vial density of ∼100 flies.
(H) Data was acquired for a total of 3 hours from one FlyPEZ in two separate ways. Flies entered the viewing platform either at will (no gate) or using FlyGate.

Passed trials are downloaded from the camera, saved, and queued for a subsequent rapid manual curation step using a custom graphical user interface (Figure 2.6A-B) that removes any further unusable data (∼13% of videos downloaded). The net output is about 20 usable videos per 20-minute experiment for each FlyPEZ (Figure 2.5A-C). Our setup of four FlyPEZ devices can acquire over 1500 videos in 8 hours, enough data to test at least 40 experimental conditions per week, which is sufficient for large silencing or activation screens (Figure 2.5D-G). When compared to using the device without the FlyGate (Figure 2.5H), FlyPEZ confers a 100-fold increase in throughput per device.

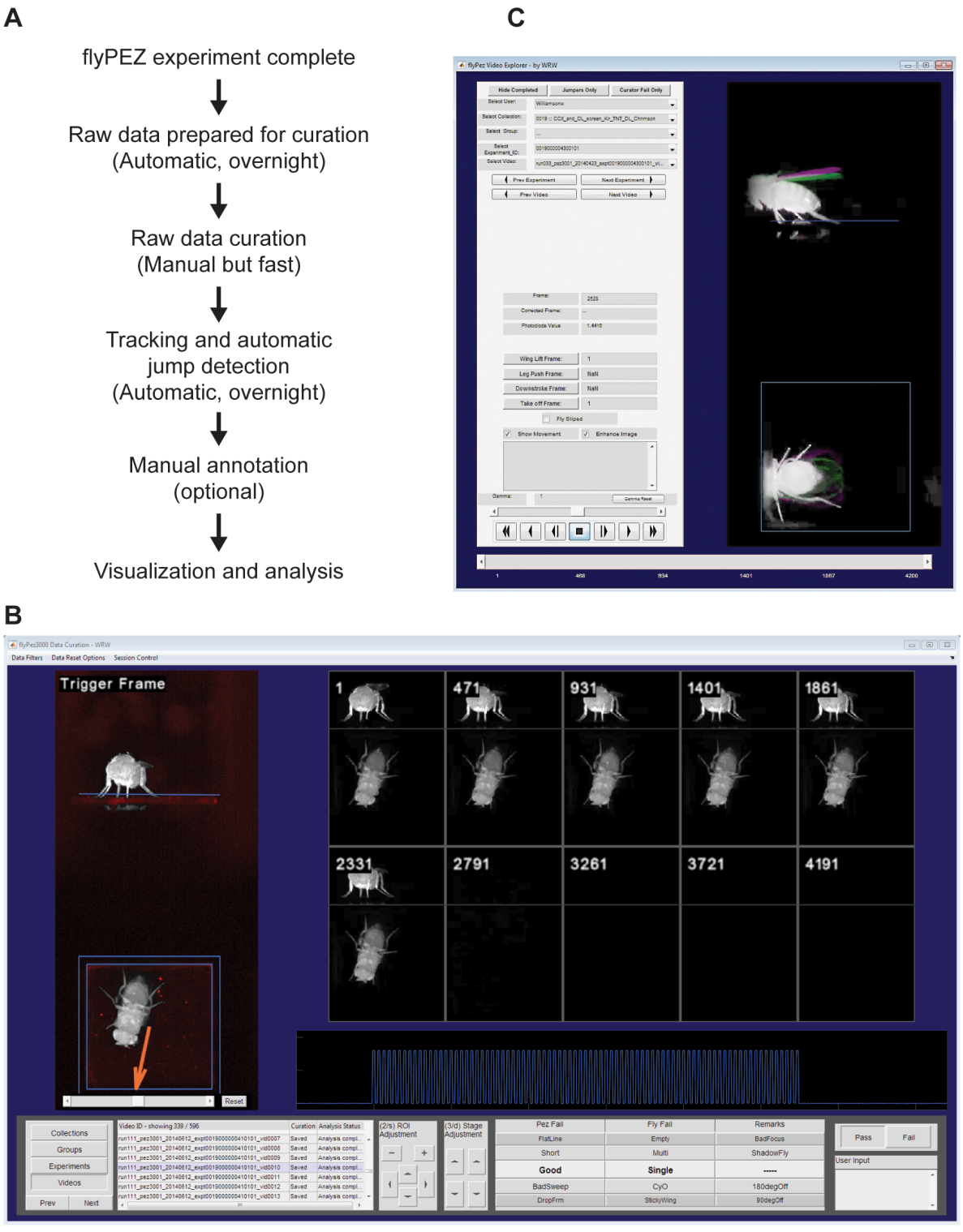

Figure 2.6: FlyPEZ Data Management Pipeline

Figure 2.6 ***(previous page)*****: FlyPEZ Data Management Pipeline**
(A) Raw FlyPEZ video data is collected and organized by date, run, and FlyPEZ device number. On a separate computer, a program scheduled to run every night re-organizes the newly acquired data into an 'experiment ID' based system. During this phase, the timing of stimuli is determined, metadata consistency is cross-checked, and the data is queued for manual curation.
(B) The data curation GUI is used to assess raw FlyPEZ data. Data are manually marked for exclusion ('Fail') based on any of the manually noted conditions: more than one fly is present during the video; no fly is present; the fly from the previous video was not cleared; an obvious balancer phenotype, such as curly wings, are visible; there is an error in the stimulus photodiode data. A 'user input' text entry box also allows users to exclude data for other reasons at their discretion. Users also note the accuracy of FlyDetect by determining whether the arrow is facing the same direction as the fly. An experienced user can curate over 1000 videos per hour. Newly curated data is scheduled for post-hoc tracking overnight using the algorithm described in Figure
(C) After tracking is complete, a user may hand-annotate events such as the precise timing of wing raising. This is facilitated by the Video Explorer program, a separate graphical user interface designed for viewing the videos and for manual annotations.

The FlyPEZ modules FlyGate, FlyDetect, and GlobeDisplay work in concert to provide efficient automation of single-fly behavioral experiments. The modules are straightforward to assemble either independently or as an integrated system (Figure 2.7) from the complete FlyPEZ parts list, design files, and code base (including the FlyDetect algorithm) available for download at: `https://www.dropbox.com/home/Paper_WRW_pez3000/FlyPEZ_supporting_documents/FlyPEZ_design_and_assembly`. In particular, the FlyGate can be built independently for less than $2500 USD, which is comparable to other fly dispenser technologies [2, 125]. The stand-alone dispenser module (Figure 2.2B) could thus be used to deliver flies from a home vial into any apparatus without perturbation from handling.

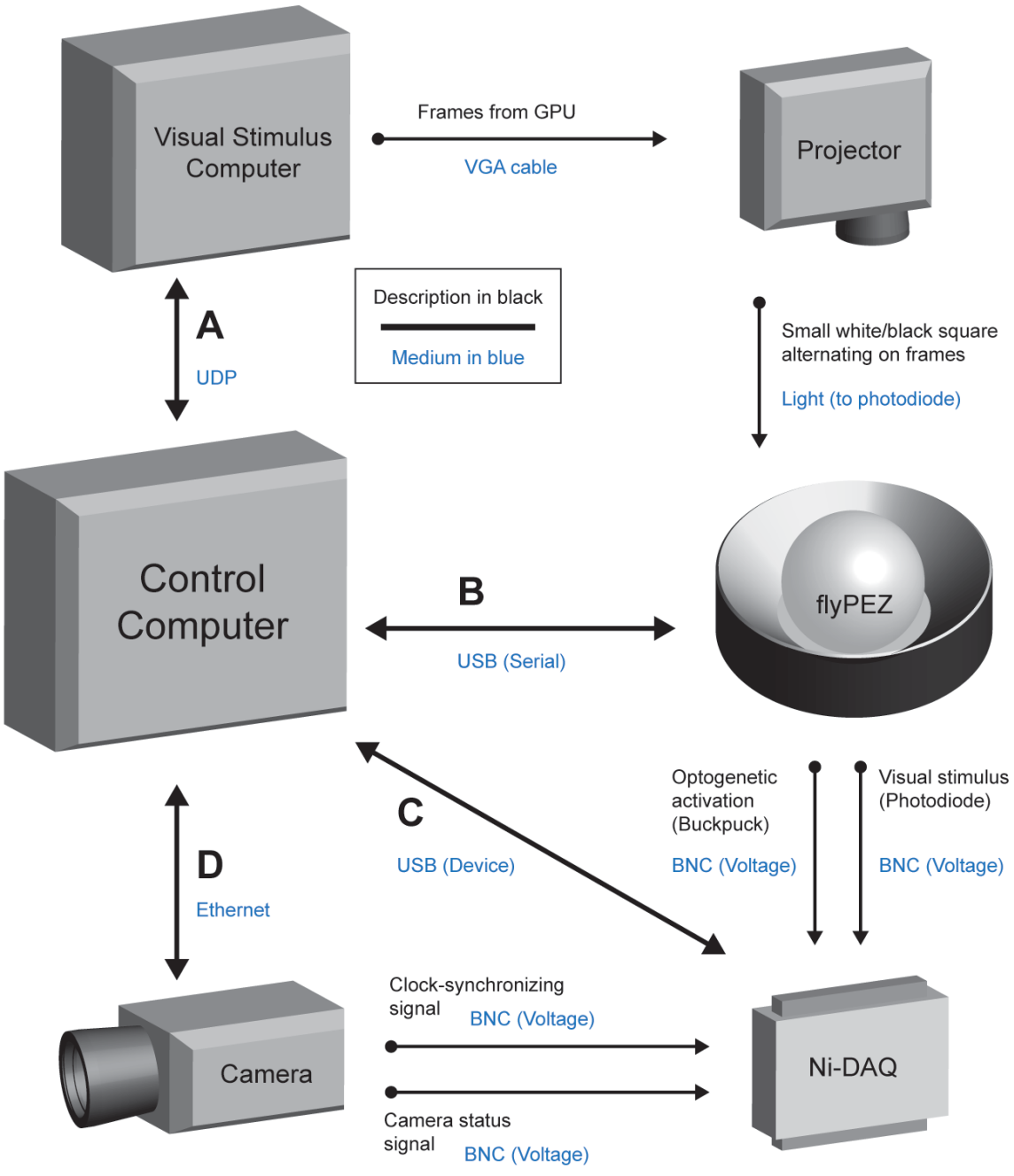

Figure 2.7: FlyPEZ Hardware Communication Diagram

Figure 2.7 *(previous page)*: FlyPEZ Hardware Communication Diagram
The control computer is responsible for coordinating all hardware activities during data acquisition. (A) When a visual stimulus is scheduled with an experiment, the control computer sends the name of a pre-generated stimulus to the visual stimulus computer, which prepares the frames using Psychophysics Toolbox in MATLAB (see Methods). During an experiment, the control computer sends fly azimuth information and triggers the visual stimulus computer with a latency of 200-300 ms. After the stimulus presentation, the visual stimulus computer sends a success or failure message to the control computer. The timing of the stimulus relative to the video recording and an assessment of the execution of the stimulus is accomplished by analyzing a photodiode record acquired by the Ni-DAQ. This two-way communication is facilitated using User Datagram Protocol (UDP) via an inexpensive specialized UDP cable which connects to the Ethernet jack.
(B) A USB serial connection transmits commands to and receives status data from the FlyPEZ. Information from the FlyPEZ includes: temperature, humidity, fly count, cooling power, and the linear photodiode sensor data. Commands from the FlyPEZ include target temperature, IR light intensity, sweeper, gate position, and optogenetic activation prepare/execute.
(C) The National Instruments data acquisition board (Ni-DAQ) provides a digital clock and synchronizes all stimulus and recording events at a sub-millisecond timescale. It receives voltage-encoded status signals from: 1) the FlyPEZ buckpucks, which directly correlate to optogenetic activation LED intensity; 2) from the photodiode, stimulated by a region of visual stimulus projection; and 3) from the camera (recording start/stop). The Ni-DAQ sends this information to the control computer, and since the Ni-DAQ and camera clocks are synchronized, all events recorded by the Ni-DAQ can be associated with specific recorded video frames.
(D) Each camera has an IP address and the control computer manages the camera via an Ethernet cable using transmission control protocol (TCP). Using this connection, the control computer can change the camera settings, set record/live feed status, and receive video frames. These tasks are accomplished using the control program we generated in MATLAB using the software development kit provided by PHOTRON.

2.4.2 High-resolution quantification of visual behavior in freely-behaving Drosophila

As a demonstration of the type of high-resolution behavioral analyses that can be conducted using FlyPEZ, we examined the kinematics of unrestrained flies in a classic visual behavior paradigm: the optomotor response. Rotation of the visual panorama induces most animals with a visual system to follow the direction of the motion, reducing retinal slip to stabilize their gaze (direction the eyes are facing) relative to the background [57]. Flies adjust their gaze by a combination of turning their body and turning their head (to which the eyes are fixed). In blowflies, evidence suggests that walking animals improve performance of their visual system by navigating with rapid turns ('saccades'), during which head velocity

exceeds that of the body, such that the head completes the turn before the body [14]. A similar program has been observed in tethered *Drosophila* walking on a ball [51], but not during saccadic turns in unrestrained flies navigating a maze [55]. It is thus unclear if freely-walking *Drosophila* turn their head and body together during optomotor turning responses to rotation of the visual panorama. We created panoramic vertical grating patterns with a pole at the zenith of the GlobeDisplay (Figure 2.8A, top) rotating with contrast frequencies known to elicit strong turning in tethered walking flies [57]. Our FlyDetect tracking algorithm automatically tracked the position and orientation of the thorax and head separately during responses.

Consistent with observations in tethered flies [28], we found that grating motion drives a fly to steadily adjust its gaze in the same direction as the motion, at roughly the grating speed (Figure 2.8A). We also observed a second type of gaze adjustment. Periodically, flies rapidly shifted their gaze in the direction opposite to that of the panoramic stimulus, a behavior we refer to as a 'reverse saccade' (Figures 2.8A, arrow; 2.8B, negative velocity dips). Both the onset time and the number of reverse saccades per trial were variable (Figure 2.9A). We tracked head and body movement (Figures 2.8C-F and 2.9B-E) during both inter-saccade intervals (Figures 2.8D and 2.9F) and within saccades (Figure 2.8E-F). We found that head movements were the major component of total gaze angle change for both periods. Reverse saccades also included increased translation of the center of mass in the xy-plane (Figure 2.9G). Importantly, we found that, during saccades, the head motion precedes the body turn by 45 ms (Figure 2.8F), to our knowledge the first demonstration that Drosophila use a head-before-body saccade program similar to that of house flies [14].

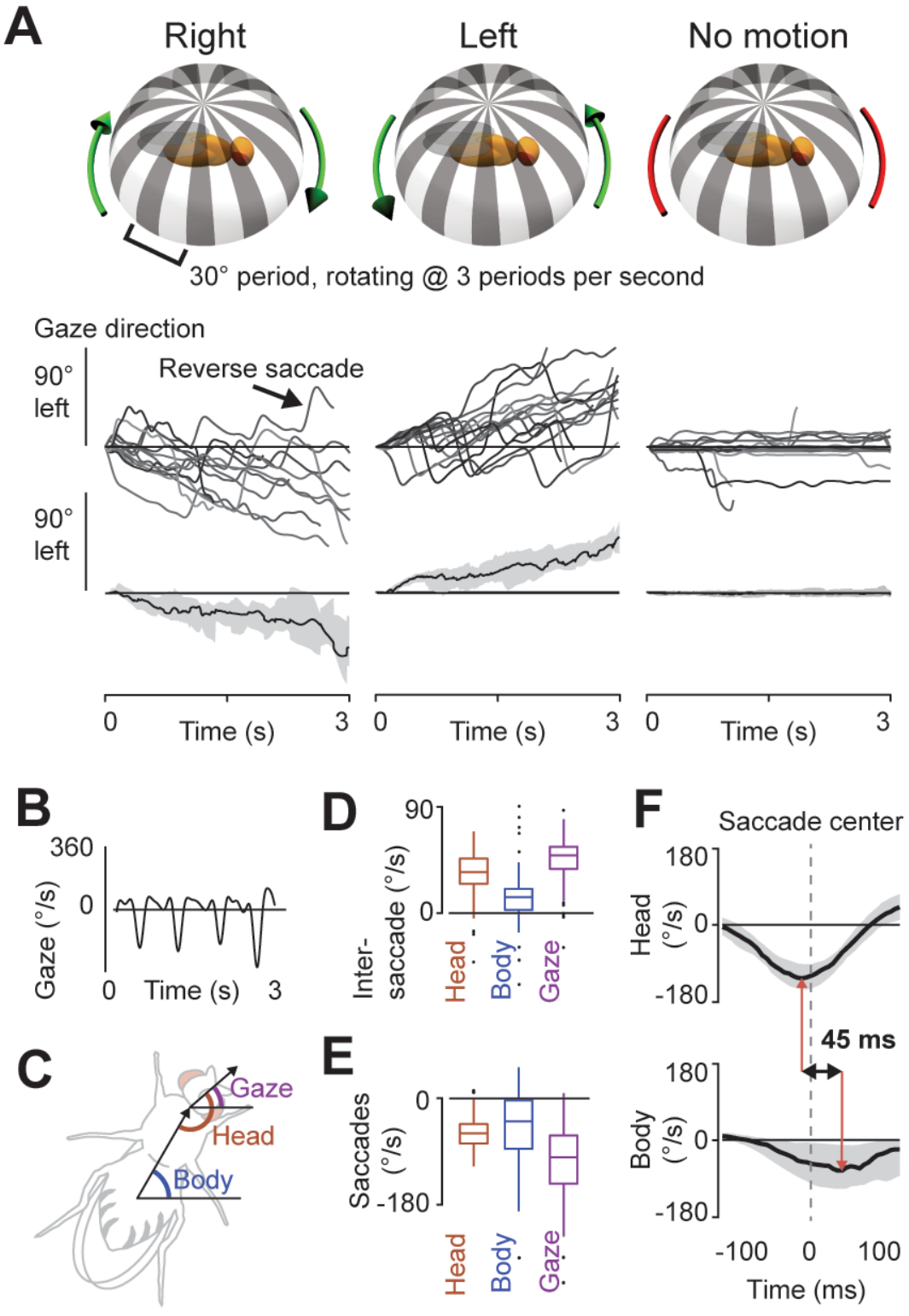

Figure 2.8: High-Resolution Quantification of Visual Behavior in Freely-Behaving *Drosophila*

Figure 2.8 ***(previous page)*****: High-Resolution Quantification of Visual Behavior in Freely-Behaving *Drosophila***
(A) Rotating gratings (30° spatial period, 3 Hz, top) projected with the GlobeDisplay evoked fly turning behavior. Gaze trajectories for individual flies are overlaid (middle row), black line and shading indicate population median and inner-quartile range, respectively (bottom row); Right, N = 18; Left, N = 31; No motion, N = 29 flies. Flies generally turned in the same direction as the grating, albeit slower. We observed periodic rapid turns in the opposite direction (reverse saccades, arrow).

(B) Single fly example of gaze angular velocity showing four reverse saccades.
(C) Schematic showing how gaze angle is composed from the body and head angles.
(D-E) Box plots of average angular velocities between saccades (D, n = 53 inter-saccade intervals, N = 49 flies) and during the saccades (E, n = 61 saccades, N = 49 flies). Data from leftward and rightward gratings were pooled and rightward grating responses were reflected as if from a leftward grating.
(F) Relative timing of head and body angular velocity changes during reverse saccades. Time equals zero is set by the point of most negative gaze angular velocity in each reverse saccade. Head angular velocity minimum precedes the reverse saccade by 10 ms (red line, top), while the body minimum occurs 35 ms after (red line, bottom), for a total head-body lag of 45 ms (black double-arrow). Black line is median and shading is inner-quartile range. (n = 61 saccades, N = 49 flies).

2.4.3 High-throughput mapping of a visual-motor transformation in three dimensions

A significant advantage of the FlyPEZ is its ability to capture three-dimensional motion data repeatedly and rapidly. To demonstrate the high-throughput capabilities of FlyPEZ, we used the system to empirically determine the comprehensive input-output function for control of the flys escape direction in response to a looming visual stimulus. Previously, we have shown that flies can adjust their azimuthal takeoff direction to move away from a rapidly expanding (looming) disk approaching from a 45° elevation [24]. However, it is unknown what strategy the fly uses to direct escape from other potential attack elevations. Using information from the FlyDetect real-time tracking algorithm, and taking advantage of the panoramic GlobeDisplay projection system, we recorded over 12,000 individual fly responses to looming stimuli positioned at 46 different azimuth and elevation locations throughout the flys dorsal hemisphere. We found that the probability of a fly performing an escape takeoff

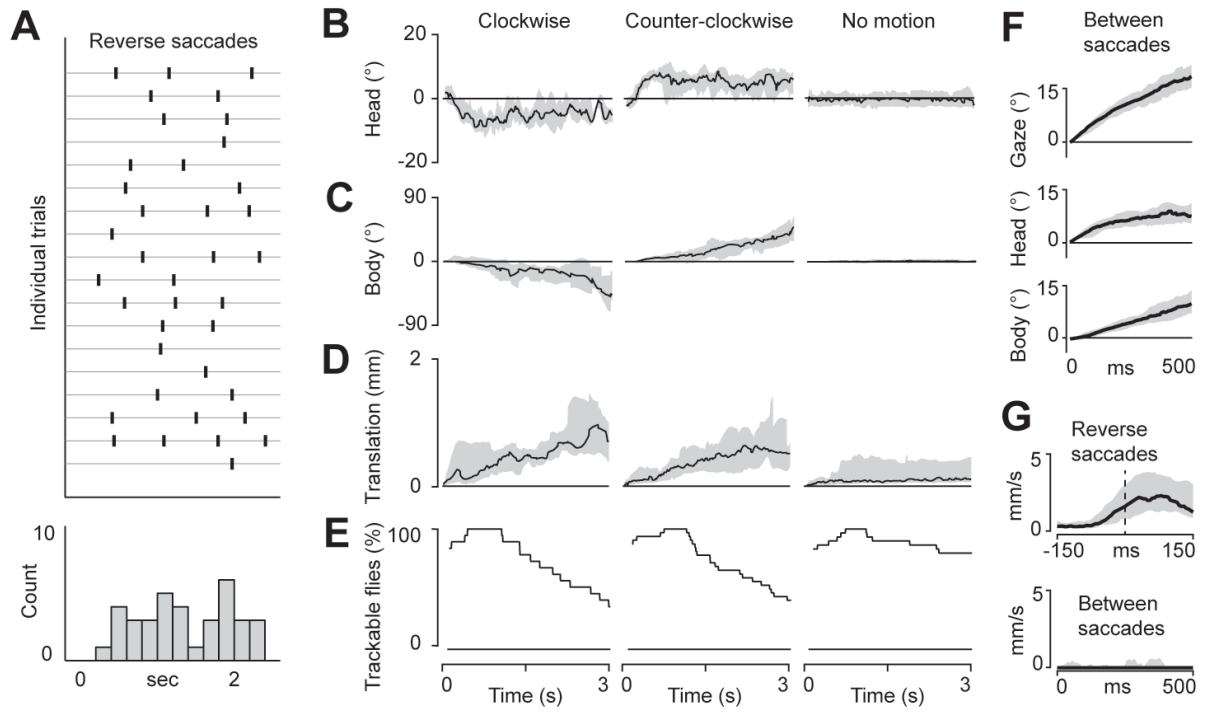

Figure 2.9: Head and Body Movements in Response to a Rotating Grating
(A) Raster plot showing occurrence of reverse saccades (see Figure 2.8) over time for all trials where the fly was tracked for at least 2.5 seconds (top) and histogram (bottom); N = 18 flies.
(B-D) Population median (black line) and inner-quartile-range (gray) of head (B) and body (C) rotation as well as center of mass translation (D) for the duration of the stimulus presentation.
(E) Percent trackable flies for the duration of the stimulus presentation.
(F) Head, body and gaze (head + body) angles over the first 500 ms between saccades. Median in black, inner-quartile-range in gray; n = 80 instances; N = 32 flies.
(G) Translational speed during reverse saccades (top, n = 61 reverse saccades) and between saccades (bottom, n = 80 instances); N = 32 flies.

depends on the position of the looming stimulus (Figure 2.10A). Interpolating from our measured stimulus locations, we determined that lateral looming stimuli at 90° azimuth and 30° elevation elicit the largest percentage of flies to takeoff, whereas frontal looming stimuli at 0° azimuth and 60° elevation, elicit the smallest (the nearest raw data points occur at elevations of 45° and 67°, respectively). To quantify takeoff direction, we reconstructed the takeoff trajectory of each fly in three dimensions using the automatic tracking of the flys center of mass in both of FlyPEZs two camera views (Figure 2.10B). For each takeoff, we manually annotated the frame in which the flys mesothoracic (jumping) legs started to extend and the frame in which the tarsi first lost contact with the ground, a total duration of 3-5 ms. We defined the direction of the escape takeoff as the vector the flys center of mass moved between these two frames. In agreement with previous, manually-performed experiments [24], flies adjusted their escape azimuth to takeoff away from the stimulus at all azimuths when the stimulus was presented at a 45° elevation (Figure 2.10C). To test whether the fly could also control its escape takeoff elevation, we looked at trials in which the stimulus has the same azimuth (0°), but the elevation varied. We show here for the first time that flies adjust their takeoff elevation to avoid the looming stimulus (Figure 2.10D).

These results represent a comprehensive description of the relationship between predator approach angle and takeoff behavior, and we used the data to model the stimulus-to-escape direction transformation function. We observed that flies did not always orient their takeoffs directly away from the stimulus, but instead also showed a bias to takeoff forward, relative to their body axis (Figures 2.10C, center plot; 2.11A). We modeled the escape direction ($\vec{R}$) as the weighted vector sum of the drive for the fly to takeoff 180° in azimuth away from the stimulus ($\vec{A}$) and the drive to takeoff forward along its own current heading ($\vec{F}$, Figure 2.10E, see also ??Data S1):

$$\vec{R} = (1 - m)\vec{A} + (m)\vec{F} \tag{2.1}$$

Using our data, we empirically solved for the relative weighting of away vs. forward drive, m, across the full range of stimulus azimuths, at elevations 0°, 23°, and 45°. We found that

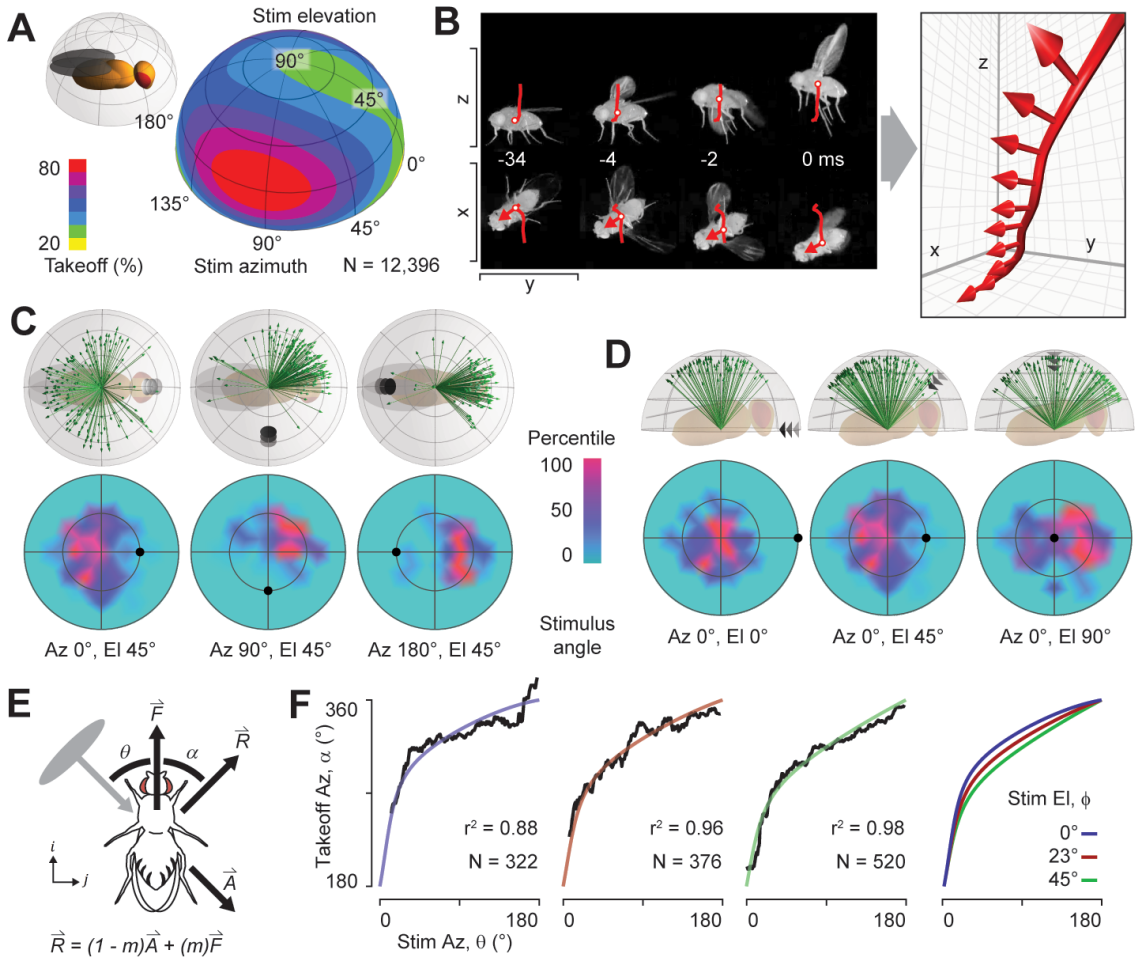

Figure 2.10: High-Throughput Mapping of a Visual-Motor Transformation in 3D
(A) Takeoff rate in response to looming stimuli presented from different locations throughout the flys entire dorsal visual field, interpolated from 46 azimuth-elevations positions (see Methods). Inset illustrates orientation of the fly. Location on the sphere represents a stimulus location; color indicates takeoff rate (ranging from 20% to 80%), N = 12,396 flies.
(B) We reconstructed each flys center-of-mass jump trajectory and heading in three dimensions using the dual-perspective image recorded with a high-speed video camera at 6,000 frames per second.
(C-D) Takeoff direction (green arrows) in response to looming visual stimuli approaching from various azimuth and elevation locations, illustrated by the black 3D arrows embedded in each panel. Data are a random subsample of the entire population (N 150 shown for each panel). Population summaries (bottom row) are color-coded, interpolated histograms, shown from a top-down perspective. (C) N = 507, 0° az; N = 908, 90° az; N = 132, 180° az. (D) N = 85, 0° el; N = 507, 45° el; N = 152, 90° el.
(E) We model the flys jump direction ($\vec{R}$) in a given trial as the weighted sum of a vector oriented directly away from the stimulus ($\vec{A}$) and a vector oriented forward along the fly's heading ($\vec{F}$). The vector coefficients sum to 1 and can thus be defined by a single variable, textitm.
(F) Takeoff direction azimuth (α) in response to looming visual stimuli azimuth (θ) for elevations 0°, 23°, and 45°. Each black line is a sliding median. Color lines were calculated using the model in (E); r^2 indicates goodness-of-fit compared to the original data.

m could be modeled as a linear function of the stimulus azimuth (θ, Figure 2.11B):

$$m(\theta) = (w * \theta) + c_1 \tag{2.2}$$

This means that as the stimulus moves in azimuth from in front (0°) to behind the fly (180°), the weighting of the 'away drive' increases. Furthermore, the coefficient w was itself well-fit by a negative linear function of stimulus elevation ($w(\phi)$, $r^2 = 0.997$, Figure 2.11C):

$$W(\phi) = (c_2 * \phi) + c_3 \tag{2.3}$$

This indicates that higher stimulus elevations correspond with an increased away drive in response to looming stimuli approaching from the front. In other words, if flies are attacked from low elevations, their takeoff has a stronger forward bias, whereas if they are attacked from higher elevations (overhead), their takeoff has a stronger bias away from the stimulus. By using our data to fit only three constants (c_1, c_2, c_3) in two linear equations, we were able to predict the median takeoff direction of the fly (α) in response to a looming stimulus from most locations (θ,ϕ) in its visual field (Figure 2.10F).

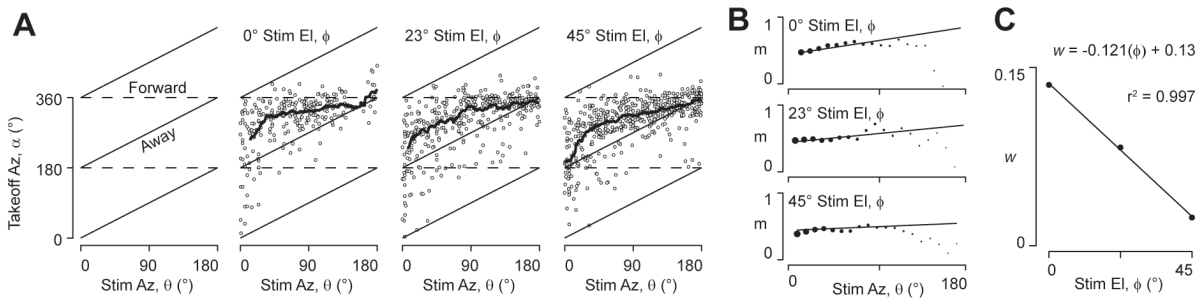

Figure 2.11: Modeling Escape Direction

(A) Scatter plots of the takeoff direction azimuth (α) in response to looming visual stimulus azimuth (θ). Each dot represents a single jumping fly. Three elevations (ϕ) were selected for analysis: 0°, 23°, and 45°. The median jump direction (black line overlaid) was calculated using a sliding window of 9. The horizontal dashed line at $\alpha = 360°$ indicates where the data would fall if the fly always took off forward relative to its own heading ($\vec{F}$). The solid diagonal black line indicates where the data would fall if the fly always took off directly away from the stimulus ($\vec{A}$).

(B) The relative weighting parameter, m, between forward and away directions can be calculated for each trial from the azimuth of the stimulus presented to the fly and the azimuth of its resulting escape takeoff. Black dots represent values for the variable (m) calculated at the center of 9° bins spanning the stimulus azimuth. Dot size represents the influence of (m) on takeoff direction ($\vec{R}$), which decreases linearly as the difference between A and F from (θ) = 0° to 180° (since at $\theta = 180°$ $\vec{A}$ and $\vec{F}$ are the same, so m will be arbitrary). Lines were generated using the equation $m(\theta) = (w * \theta) + c_1$ (Eq. 2.19), according to the escape direction model. Weighted goodness of fit values (r^2) for top, middle and bottom, respectively: 0.47, 0.46, and 0.27.

See 2.7 for derivation.

2.4.4 Distinguishing behavioral roles for neuronal cell types

A premise of the FlyPEZ is that behaviors may need to be analyzed at high temporal and spatial resolution to distinguish the role of individual cell types in coordinating those behaviors. As a final proof of this concept, we used the FlyPEZ to investigate how activity in two different visual projection neuron cell types influences the expression of looming-evoked takeoff behaviors. We previously screened all 20 known lobula columnar (LC) visual projection neuron types [162] and established that only two, LC4 and LC6, drive a takeoff behavior in 100% of flies when activated. Although they both drive takeoff and their dendritic arbors overlap (Figure 2.12A, asterisk), we hypothesized that LC4 and LC6 may have different functions in coordinating escape from looming predators because their axons terminate in distinct central brain glomeruli (Figure 2.12A, arrows), and they have distinct visual looming responses. LC4 neurons (Figure 2.12A, red) synapse directly onto the ipsilateral Giant Fiber (GF, Figure 2.12A, yellow; [156]), a descending neuron whose activation induces a takeoff jump, and they encode fast looming motion [156]. In contrast, LC6 terminals do not overlap GF dendrites (Figure 2.12A, blue), and respond preferentially to slow looming motion [162]. Silencing LC4 or GF neurons is known to alter the timing of wing and leg actions during the takeoff sequence. Specifically, without functional GFs flies are unable to produce a 'short mode' takeoff sequence, in which the fly jumps off the ground before it fully elevates its wings. Instead, the fly is limited to using only a 'long mode' takeoff, in which the wings are raised at least 7 ms prior to the tarsi leaving the ground (Figure 2.12C). As GF presynaptic partners, LC4 are also implicated in control of the short mode takeoff, but the contribution of LC6, if any, to takeoff control is unknown.

To examine in more detail the roles of LC4 and LC6 neurons in looming-evoked escape, we used the FlyPEZ to analyze the detailed timing of wing and leg actions during hundreds of takeoff sequences where activity in LC4, LC6, or GF neurons was enhanced or depressed. To optogenetically activate each cell type, we expressed the photoactivatable ion channel, CsChrimson [81] using a cell-type specific genetic driver [162] and then triggered a 50-ms red

light pulse with 3.5 mW/mm^2 power when a fly appeared on the FlyPEZ recording platform (Figure 2.12B). This light intensity elicited takeoff in 100% of flies in which LC6, LC4, and GF were activated (Figure 2.12D) but almost no control flies with the CsChrimson transgene but no cell-type specific driver.

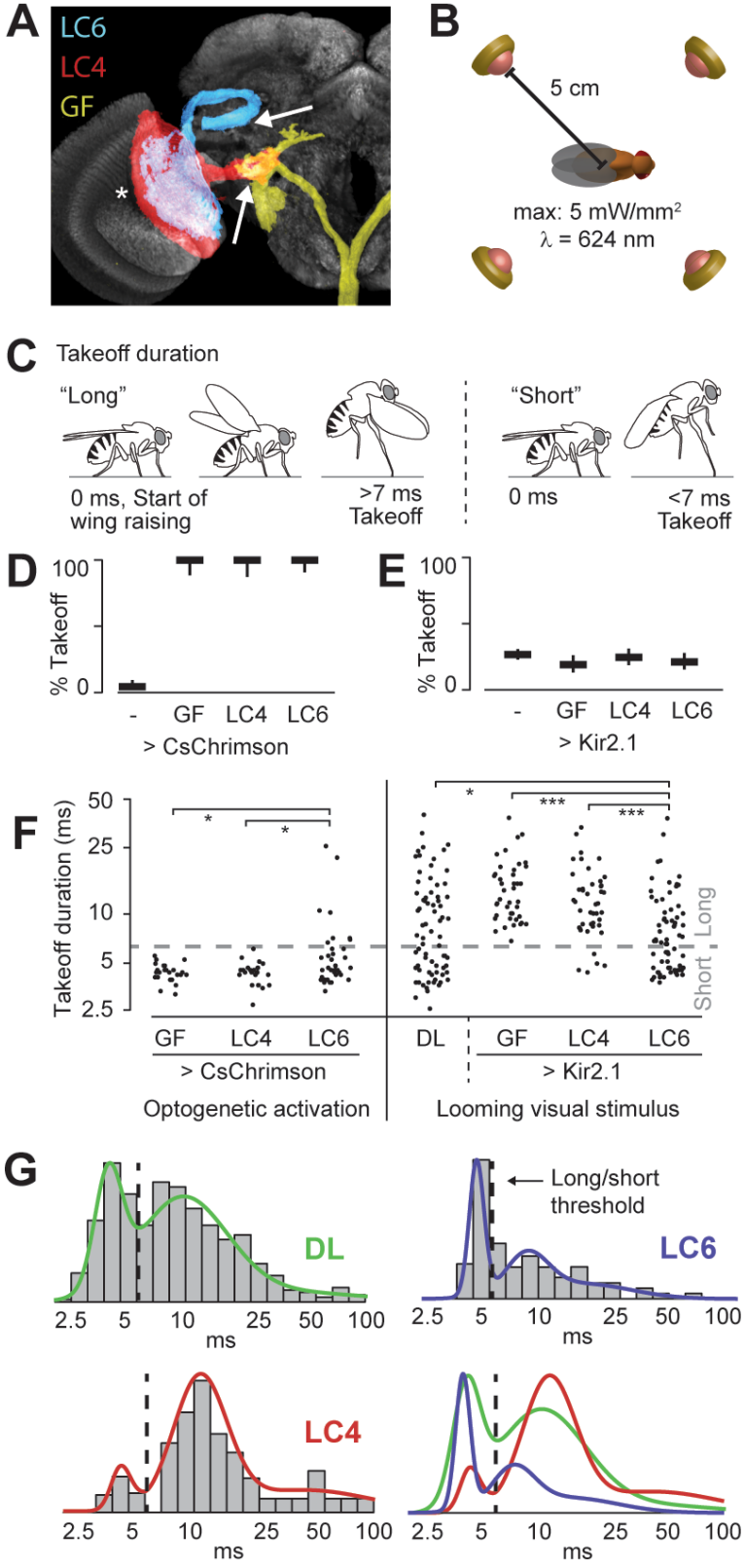

Figure 2.12: Distinguishing Behavioral Roles for Neuronal Cell Types

Figure 2.12 ***(previous page)*****: Distinguishing Behavioral Roles for Neuronal Cell Types**
(A) Neuroanatomy of lobula columnar (LC) visual projection neuron cell types LC6 (blue) ([162]), LC4 (red) ([162]), and, the giant fiber (GF) descending neuron (yellow) [156]. Image is an overlay of expression patterns of eGFP-tagged CsChrimson (used for optogenetic activation) targeted selectively to each cell type. Images are adapted from previously published data ([156, 162]) acquired via personal communication. Presynaptic regions for LC4 and LC6 indicated with arrows, asterisk denotes dendrites.
(B) Optogenetic experiments employ four red LEDs (624 nm wavelength), positioned 5 cm from the fly to emit a maximum light intensity of 5 mW/mm^2.
(C) The duration of the takeoff motor program (takeoff duration) can be 'long' (>7 ms) or 'short' (<7 ms). In long takeoffs, but not short ones, the fly fully raises its wings before leaving the ground.
(D-E) Percentage of flies that takeoff in response to optogenetic stimulation (D) and looming visual stimuli when genetically silenced (E). For (D), N = 123, 30, 27, 38 flies for control, GF, LC4, and LC6 conditions respectively; for (E), N = 491, 152, 196, 180 flies for control, GF, LC4, and LC6 conditions respectively. Vertical lines are 95% confidence intervals determined using the Clopper-Pearson method.
(F) Distribution of takeoff durations in response to optogenetic activation (left) and looming visual stimulus (right). Dashed line indicates the 7 ms short versus long takeoff boundary. For CsChrimson experiments, N as in (C); for Kir2.1 experiments, N = 463 (100 randomly subsampled data points shown), 41, 87, and 59 for DL, GF, LC4 and LC6 conditions respectively. All distributions were compared using the two-sample Kolmogorov-Smirnov test. CsChrimson: GF-LC6, $p = 0.03$; LC4-LC6, $p = 0.01$; Kir2.1: DL-LC6, $p = 0.02$; GF-LC6, $p = 4.0 * 10^{-8}$; LC4-LC6 $p = 1.3 * 10^{-5}$.
(G) Histogram of looming evoked takeoff durations for DL, LC6, and LC4 silencing experiments. Black dashed line indicates 7 ms boundary between long and short takeoffs. Gaussian mixed model fit in color-coded lines. Same sample size as in (F).

In separate experiments, to investigate loss-of-function phenotypes, we genetically silenced these neurons by expressing the inward rectifying potassium channel, Kir2.1 [10], in a DL wild type background, and recorded fly responses to frontal looming (0° azimuth, 45° elevation) at a variety of looming speeds (l/v = 20, 40, or 80). We found no significant reduction of the looming-evoked takeoff rate relative to the control flies with the Kir2.1 genetic background but no cell-type specific driver (Figure 2.12E). Next, we manually annotated wing and jumping leg movements in each trial using a custom graphical annotation interface (see Methods, Figure 2.6C). Confirming previous results, we found that silencing either GF or its presynaptic partner, LC4, significantly reduced or eliminated short mode escapes and that activation of either of these cell types produced only short mode takeoffs (Figure 2.12F). LC6 silencing and activation, however, resulted in takeoff duration distributions that were

significantly different from GF, LC4, and the DL wild type control (Figure 2.12F). To visualize this more clearly, we fit the takeoff duration distributions of the DL control, LC4, and LC6 silenced data with a mixture of Gaussians model (Figure 2.12G). The control data are fit well by a bimodal distribution, with distinct peaks indicating the short and long modes (Figure 2.12G, green). Whereas LC4 silencing significantly reduced the first peak, representing the proportion of flies executing a short (<7 ms) escape (Figure 2.12G, red), we found that LC6 silencing strongly decreased the amplitude of the second peak (Figure 2.12G, blue). This indicates that the long mode is suppressed when LC6 is silenced, suggesting that LC6 contributes to the long mode escapes through a descending pathway distinct from the GF. LC6 is thus the first neuronal cell type determined to be involved in the 'long mode' escape pathway. Our results demonstrate that LC4 and LC6 visual projection cell types contribute differentially to the timing and control of looming evoked escape behaviors, a distinction most evident at the level of individual appendage movement.

2.4.5 Behavioral range and flexibility of the FlyPEZ

In the examples above, we have focused on optomotor head movements and the actions of the wings and legs during looming-evoked escape to demonstrate the FlyPEZs ability to quantify behavior of unrestrained animals with the temporal and spatial resolution required to observe detailed action of the appendages. In addition to these examples, we also observed a wide range of other behaviors using the FlyPEZ (Figure 2.13. These include spontaneous behaviors such as takeoff, wing flicking, abdomen flexion, proboscis extension, defecation, and grooming (Figure 2.13A-H). We also observed optogenetically-triggered actions including takeoff, backwards walking, turning, and reaching (Figure 2.13I-L) using flies expressing CsChrimson in GF, LC16, LC17, and LC10-1, respectively (see also [162]).

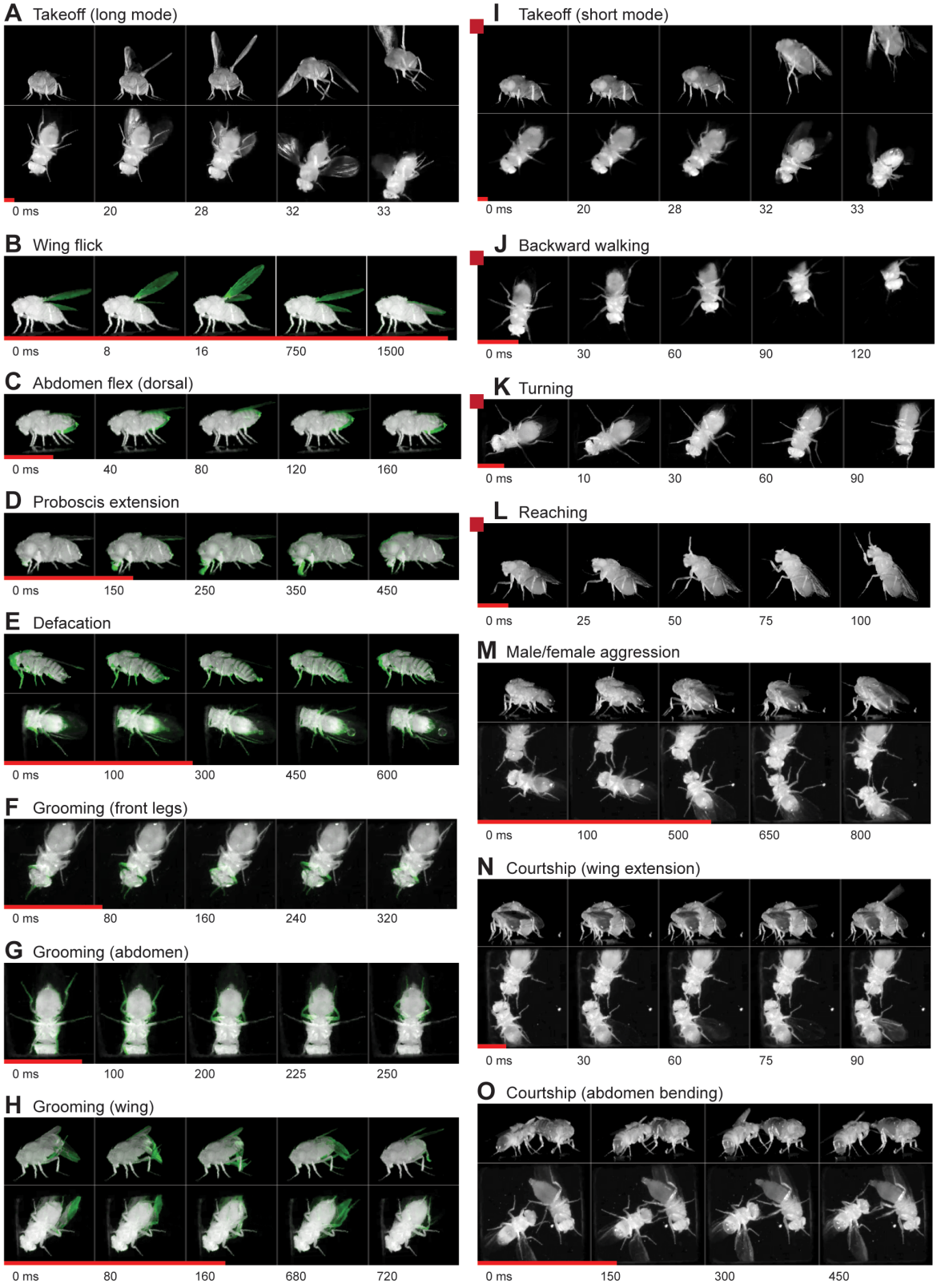

Figure 2.13: Behavioral Range of the FlyPEZ

Figure 2.13 ***(previous page)*****: Behavioral Range of the FlyPEZ**
A range of different behaviors recorded using FlyPEZ are represented as a short series of still frames. The red line below each panel represents the relative duration of each recording. Red squares at the top, left corner indicate behaviors induced by optogenetic activation.
(A) Voluntary takeoff, demonstrating the long-mode of jumping with wings raised (see Figure 2.12).
(B-H) Behaviors involving subtle movements, some of which involve a single appendage. Pixels changing in intensity from one frame to the next have been highlighted in green to facilitate identification of the moving part.
(I-L) Behaviors induced by optogenetic activation of the giant fibers (I), and the lobula columnar cell types LC16 (J), LC17 (K), and LC10-1 (L). Giant Fiber activation elicits the short-mode of jumping without wings raised (see Figure 2.12). (M-O) Social interactions can also be observed at high-resolution on FlyPEZ. These sequences show including aggression (M), wing extension (N), and abdomen bending (O) between a male and female fly.

In general, since the FlyPEZ achieves high-throughput and external stimulation control by isolating individuals on a small platform, it is well-suited to examine of the vast array of behaviors that flies perform in a relatively local spot. In addition to those shown in Figure 2.13A-L, this could include egg-laying, as well as courtship and aggressive displays. To illustrate the potential to observe social interactions between two flies, such as courtship or aggression, we performed experiments in which we programmed the FlyGate to allow two flies to pass rather than one. Figure 2.13M-O shows example interactions from a male and a female isolated together on the platform, including aggressive interactions with their legs (Figure 2.13M), wing extension during courtship (Figure 2.13N), and male abdomen bending during courtship (Figure 2.13O). The examples above illustrate the FlyPEZs ability to observe a wide range of innate or stimulated behaviors. In addition, with minor modifications, the FlyPEZ could also be used for quantifying behaviors related to learning, memory, and adaptation. Critically, these would require repeated measurements of the same individual over time or during repeated stimulation. FlyPEZ, in the implementation presented here, captures only a single trial per individual to achieve high throughput. To perform repeated measurements from the same fly, we augmented two of our FlyPEZ setups by adding a small, 25 mm diameter, glass dome over the platform and moat area, leaving the moat dry (Figure 2.14A). The dome was large enough to allow a fly to execute an escape takeoff, but small

enough that a fly could readily find its way back to the platform. For these demonstration experiments, we disabled the sweeper function and programmed looming stimuli to be displayed every 30-seconds to encourage movement. Since our real-time FlyDetect algorithm triggers whenever a fly appears on the platform, the fly exploring the small space repeatedly triggered the looming stimulus and video recording. The rate of data acquisition was steady over an 80-minute period (Figure 2.14B), during which over half of the flies tested (14/24) returned to the platform and triggered the stimulus multiple times, with a single-fly maximum of 21 triggers (Figure 2.14C). The looming-evoked takeoff rate and response time were not different between flies from single trial experiments (no dome) and the first trial of each fly tested inside the clear dome (Figure 2.14D-E), indicating that the clear dome itself did not impair the flys view of the GlobeDisplay stimulus. For looming-evoked takeoffs, we did observe habituation over repeated stimulation such that after the third trigger, average takeoff rate began to decline. Altogether, the FlyPEZ assay is a versatile platform that can be used to automatically capture a range of innate, social, and learned fly behaviors.

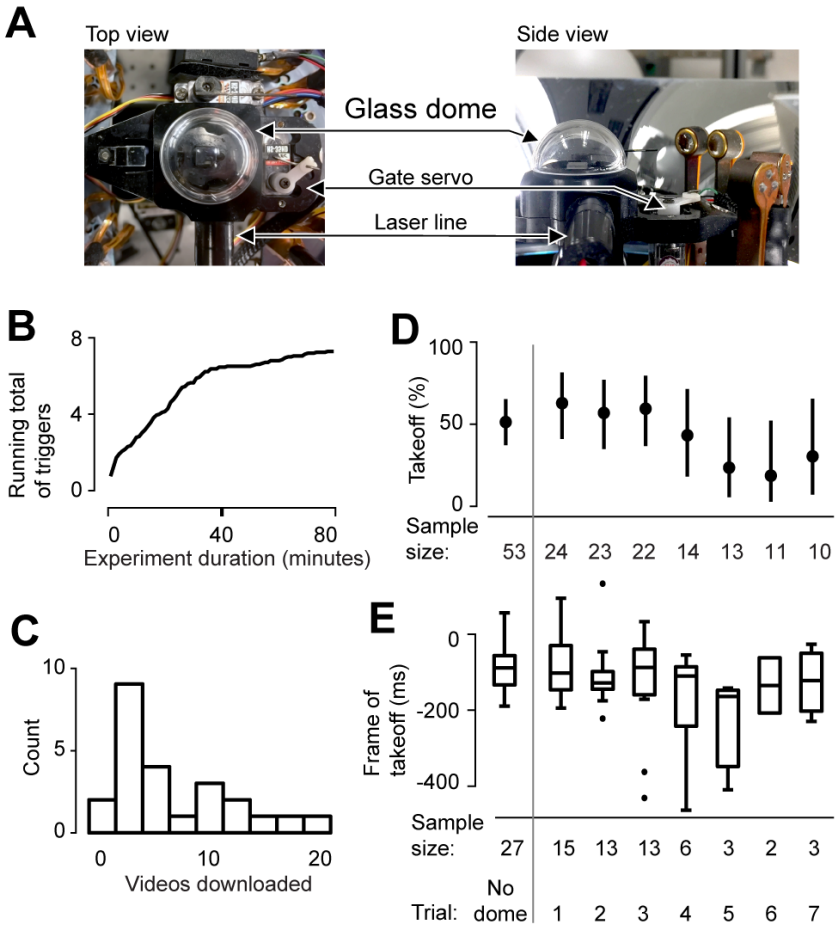

Figure 2.14: FlyPEZ Flexibility: Quantifying Repeated Stimulation of Individual Flies
(A) Photos of the FlyGate apparatus augmented with a small glass dome which retains an individual fly near the platform for repeated experimental trials.
(B-C) Rate of data acquisition under this regime. Average number of videos downloaded per fly over an 80-minute experiment (B, N = 24) and a histogram of total videos downloaded per single-fly experiment (C).
(D-E) Variability in the rate (D) and timing (E) of takeoff behavior after repeated presentations of a looming visual stimulus approaching at $l/v = 40$, from 90° az, 45° el. Single stimulation of 53 individual flies without using the dome ('No dome') is compared to the first 7 rounds of repeated stimulation using the dome (sample size as indicated).

2.5 Discussion

FlyPEZ achieves high-throughput measurement of fly behavior by automatically isolating individual flies on a recording platform, where they are precisely targeted for optogenetic or visual stimulation and simultaneous videography. High-speed videography with macrophotography allows quantification of the behavioral response at a temporal and spatial scale sufficient to capture the movement of individual body parts. On our 5 mm X 5 mm platform, flies exhibit a wide range of complex behaviors during which one can clearly visualize the coordination of legs, wings, head, and other moving fly parts. The large sample sizes, fine spatiotemporal scale, and stimulus flexibility afforded by the FlyPEZ should allow experimenters to observe important changes in behavior when modulating brain activity, such as by the sparse activation or silencing of individual neuronal cell types.

2.5.1 Experimental strengths and utility of the FlyPEZ

Our approach to isolating an individual fly on a small platform offers several advantages. The FlyGate dispenser mechanism relies on an innate fly behavior (negative geotaxis), by which flies move through the apparatus voluntarily, preventing undue arousal or damage by any direct perturbation. Mutant flies with significant motor impairments may not be able to climb this apparatus, however, we see this as an advantage, as such broad deficits are not generally the result of the kind of specific perturbation we designed FlyPEZ to test and instead often appear as false positive 'hits' in forward screens. By confining the location of the fly to a small area, its behavior can be recorded within the narrow focal depth (here, 4 mm) of high magnification lenses without having to actuate large, heavy high-speed video systems or invest in multiple expensive cameras. Isolation also confers experimental control against unwanted influence by conspecifics. Additionally, by confining the fly to the center of a panoramic screen, visual stimuli can be specifically targeted to any location in the flys visual field on a trial-by-trial basis using only a few components (light source, projector,

conical mirror, and spherical screen). The FlyPEZ system was created with affordability and simplicity in mind, relying on commercially available parts when possible and designing custom hardware that is easily manufactured by third party vendors using the downloadable supplementary CAD files we provide. Parts for the FlyGate dispenser module cost less than $2500 manufactured. The FlyDetect software is open-source and available for download. The GlobeDisplay spherical screen with custom conical mirror can be built for ∼$5000. The two most expensive components of our implementation of FlyPEZ are the projector and high-speed video camera, both of which could be exchanged for other commercially available options without disrupting FlyPEZ automation. We required 6000 frames per second to record the 3-ms jump takeoff of the fly, but this is the fly's fastest action. We have successfully tracked other behaviors, such as body turning during optomotor responses, at a tenth that rate (600 fps), which makes them appropriate to capture with less expensive video cameras. The modular construction of the FlyPEZ makes its technology potentially useful for a broad range of experimental approaches. The FlyGate release mechanism can be adapted to automate an existing experimental setup by auto-loading single flies at a set rate or in response to a trigger condition. For example, this can be incorporated into aggression assays, which are individually loaded [150] and sensitive to manual fly handling [149]. On its own, the visual stimulus apparatus can be used as an immersive virtual reality environment while maintaining the simplicity of control by a single projector. Finally, because the tracking algorithm functions even when only part of a fly is visible, it may be useful for other assays in which existing tracking algorithms perform poorly at chamber edges or with occlusions.

2.5.2 Demonstration optomotor and escape studies

As a proof of concept that the FlyPEZ enables a more precise and comprehensive quantification of natural fly behaviors, we used FlyPEZ to study two known innate visual behaviors: the optomotor response and looming-evoked escape. For the optomotor response, it was unclear whether freely moving flies use head movements as well as body movements to sta-

bilize their gaze during turns elicited by rotating whole-field gratings. We found that the head and body turn together when slowly tracking a 3Hz grating, as in tethered preparations ([28, 78]), but that the head precedes the thorax during reverse saccades, a rapid gaze adjustment opposite to the direction of visual grating motion, similar to the optokinetic nystagmus reflex observed in humans [27]. This suggests that *Drosophila* use algorithms similar to those in larger flies [14] and other species, to stabilize the visual world on their retina. For looming-evoked escape it was known that flies can control their escape direction [24]. However, prior manual methods only quantified escape for a subset of possible predator attack angles. Using FlyPEZ to track the escapes of thousands of flies, we quantified 3D escape directions from a comprehensive sampling of locations throughout the flys entire dorsal visual field. We found that control of escape direction can be modeled by the weighted sum of a drive to takeoff forward and a drive to takeoff directly away from the stimulus in azimuth, and that the relative weights of these two drives changes with elevation. The ability to quantitatively articulate the algorithms describing a behavior is a critical first step not only for understanding the behavior itself but for elucidating the computations and neural implementations that underlie it [96]. For example, in future work, we can now investigate whether neurons controlling the leg postural adjustments that determine takeoff direction are also separable into systems directing the fly forward or away from a stimulus. Our data show that many of these behavioral algorithms are occurring at the scale of individual appendage actions over milliseconds. For example, to properly study orientation behaviors in *Drosophila*, both the head and body must be tracked. By substantially increasing the number of high-resolution observations and stimulus conditions that can be measured compared to manual methods, FlyPEZ enables experimenters to generate such algorithms to describe a range of behaviors.

2.5.3 Extensibility to other behavioral paradigms

Beyond identifying behavioral algorithms, FlyPEZ, used in conjunction with the Drosophila genetic toolkit, provides a platform to interrogate their neural implementation. As an example, we used the FlyPEZ to identify distinct roles for different visual projection neuron cell types in the coordination of the looming escape response. We used the Drosophila split-GAL4 expression system to express either an optogenetic neuronal activator (CsChrimson) or a constitutive silencer (Kir2.1) in specific neuronal cell types whose activation has previously been shown to cause a takeoff: GF, LC4, and LC6. Using the optogenetic activation mode of FlyPEZ, we examined the takeoff kinematics when each of these cell types was activated and compared that with the takeoff kinematics under visual stimulation when each of the cell types was silenced. We found that LC6 neurons contribute to control of a specific 'long mode' of takeoff kinematics, in which the fly raises its wings prior to jumping off the ground. In contrast, LC4 and GF silencing control a 'short mode' where wing raising is bypassed for a more rapid takeoff, and which is critical for surviving the fastest predator attacks [155]. Our findings make LC6 the first cell type to be implicated for involvement in coordinating the non-GF-dependent mode of escape. The FlyPEZ makes detailed observation and screening of a wide array of behaviors possible with high-throughput experiments. Grooming, courtship, aggressive displays, feeding, and other actions are all observable within our recording platform. In the context of these behaviors, FlyPEZ can be used to conduct high-throughput behavior screens with collections of flies having any one of a variety of genetic manipulations, including: RNAi [56], enhancer-traps [157], null mutants [143], and any one of many existing GAL4 [62, 71, 148] or split-GAL4 [7, 21, 162] collections. Future developments can extend the possible applications of FlyPEZ even further. For example, by incorporating stimulus systems for other sensory modalities one could expand the use of FlyPEZ beyond visual behaviors. Because the flys location is confined, it should be straightforward to introduce mechanosensory stimuli, such as air puffs, or olfactory stimuli in directed air streams. FlyPEZ could then also be used to study multisensory integration in neural circuits, for

example in competing visual, mechanosensory, and aversive odor cues. By adding a simple clear domed cover over the platform, FlyPEZ can be used to make repeated measurements of individual flies, opening the door for studies involving learning and memory. The FlyPEZ is thus a flexible and modular system, capable of bringing high resolution, high throughput behavioral phenotyping to a wide range of experimental contexts.

2.6 Materials and Methods

2.6.1 Fly stocks

For all experiments, we used mixed gender, 2-5 day old *Drosophila melanogaster* reared at 21°C. Flies used in visual stimulus experiments were reared on standard cornmeal food with a 16:8 light:dark cycle, and flies for optogenetic activation experiments were reared in the dark on the same food plus 0.4 mM all-trans-retinal. Data were collected using control stocks or progeny from the following parent stocks:

Females:

Optogenetic Activation - *20XUAS-CsChrimson-mVenus (attP18)* [81]
Neuronal Inactivation - *w+ DL; DL; pJFRC49-10XUAS-IVS-eGFPKir2.1 (attP2)* [116, 155]

Males:

GF cell type - *R17A04_p65ADZp (attP40); 68A06_ZpGdbd (attP2)* [155]
LC6 cell type - *R92B02_p65ADZp (attP40); R41C07_ZpGdbd (attP2)* [162]
LC4 cell type - *R47H03_p65ADZp (attP40); R72E01_ZpGdbd (attP2)* [155]
LC10-1 cell type - *R35D04_p65ADZp (attP40); R80E07_ZpGdbd (attP2)* [162]
LC16 cell type - *R26A03_p65ADZp (attP40); R54A05_ZpGdbd (attP2)* [162]
LC17 cell type - *R21D03_p65ADZp (attP40); R65C12_ZpGdbd (attP2)* [162]

DL control (wild-type strain from M.H. Dickinson, Caltech)

2.6.2 FlyGate

The FlyGate module, which consists of the tunnel, smart gate, recording platform, and moat assembly, (Figure 2.1B) is removable so that a power meter (PM160, Thorlabs, Newton, NJ) covered by an iris with 2 mm pinhole may be placed at the experimental fly location to measure the light emitted by the LEDs used for CsChrimson activation and camera IR illumination. Temperature and humidity levels at the FlyGate platform can affect fly behavior. Each FlyPEZ is equipped with two Peltier cooling plates and two fans to remove heat generated from the electronics. A temperature/humidity sensor near the recording platform actively and locally controls the Peltiers and fans to maintain a target temperature. The temperature and humidity readings are saved at the time of each video download. We used a Thorlabs thermocouple to check the temperature at four locations: inside the fly vial, inside the tunnel, on the recording platform, and at the temperature/humidity sensor. Temperature at all locations measured within half a degree of each other. The fans can create vibration of the recording platform if not properly dampened, which reduces experimental throughput. We checked for vibrations at the platform using an ADXL345 three axis accelerometer (Analog Devices Inc, Norwood, MA) read at 3200 samples per second with a Teensy processor module and significantly reduced them by attaching the fan to the base holding the FlyGate module using rubber dampers.

Of the total flies exiting the FlyGate tunnel, approximately one third took off from the platform before the experiment began. If left unstimulated, about half the flies remaining on the platform spontaneously takeoff within 10 seconds, and the rest may remain for up to a minute. These durations would need to be evaluated by each FlyPEZ user because of the variability depending on genotype ([97]) and other factors, such as the temperature. The very few flies which return to the tunnel after passing the gate are pushed out by subsequent

flies, in which case both are discarded before another is quickly released. Unstimulated flies remaining on the stage exhibit a wide range of spontaneous behaviors including transient contact with the water moat using their tarsi or proboscis (see Figure 2.13 for more examples).

2.6.3 FlyDetect

FlyDetect is a template-based tracking method, implemented in MATLAB, that was designed to overcome specific challenges associated with automatically locating and tracking fly center of mass and heading from videos of unrestrained flies on a small platform, including: 1) flies can be positioned at the edge of the viewing platform, such that up to one third of the fly may be out of frame, 2) fly starting position and heading is variable, and 3) fly size varies by gender, genetics, and rearing conditions. The tracking system addresses these challenges by resampling the image such that x-y space is converted into size-rotation space, and then it uses a template to locate and track only the anterior or posterior end of the fly. See also Figure 2.3. Tracking accuracy was assessed by comparing human annotations of high-speed FlyPEZ videos to automated ones (Figure 2.3H-J). Using a MATLAB program and a mouse, an experimentally blind human clicked on the extreme ends ('head' and 'tail') of 215 flies in five video frames equally spaced along each flys trajectory. For this test, we only used videos in which the fly moved at least 50 pixels according to the tracker and both the anterior and the posterior were fully visible for the duration of the tracking. Distance was measured as Euclidean distance in pixels. The center of mass is the midpoint between the head and tail points, and the heading is the anterior direction of the head-tail vector. For the z-axis, the upper and lower bounds of the fly viewed from the side were annotated by hand, and the midpoint was compared to the tracking. By using two separate templates for the anterior and posterior halves of the fly, we were able to accurately track the fly, even if the fly was partially occluded when perched on the platform edge. Real-time FlyDetect analyzes frames at 15-Hz, while the post-hoc FlyDetect program takes 6 seconds to initialize frame one and

subsequently analyzes frames at 250-Hz. To track data used in the optomotor response assay (Figure 2.8), a modified version of the anterior template was used to track the head position and orientation separately from the body. To determine the z-component of the flys center of mass (Figures 2.10 and 2.12), we fit an ellipse to a binary version of the top half of the video frame, where the fly can be seen from the side. This view of the fly body was only occluded when the fly raised its wings prior to takeoff. We identified these frames as those in which the ellipses minimum axis exceeded the normal limits of the fly body, and z-axis values for these frames were interpolated. Center of mass data was filtered and derivatives calculated using a Savitzky-Golay filter.

2.6.4 GlobeDisplay

The GlobeDisplay system is comprised of a stand-alone computer, a projector, a conical mirror, and a spherical screen surrounding the freely-behaving fly. The computer running the visual stimulus was a small workstation (Dell Precision T1700, Dell, Round Rock, TX) with an affordable workstation graphics card (K600, Nvidia, Santa Clara, CA). The screens were made by cutting pre-made plastic globes (TRU-PLASTICS, Sturtevant, WI) to the correct height, sanding, and painting with six coats of Screen Goo rear projection paint (Goo Systems Global, Ontario, Canada). We required a panoramic view for the fly, however a single light source cannot display directly onto the entire surface of a 6-inch diameter sphere. We surmounted this problem by using a single projector to display images directly on the top surface of the sphere (from the pole at 90° down to 30° elevation) and then surrounding the sphere with a custom-built conical mirror, which reflects the remainder of the visual stimulus onto the sides of the sphere (from 30° above to -30° below the equator, Figure 2.1E). The reflected portion of the image is radially inverted to compensate for the reflection, and both portions of the image are warped digitally, such that when they encounter the curved surface of the dome they are rendered accurately in azimuth and elevation (Figure 2.4A-D). The two images are stitched together and blended around a 5° band

centered on their common boundary of 30° above the equator (Figure 2.4C). The procedure for generating the transformation algorithm can be found here: `https://www.dropbox.com/s/kwxp5toi3eoll0h/projectorCalibration3000_v3.m?dl=0`, and is performed only when FlyPEZ is assembled or when globes are changed (every 6 months). Accuracy of the visual stimulus transformation onto the globe was determined empirically by measuring lines projected to be 10 mm apart with tailor tape on the outside of the dome (Figure 2.4D). A custom-made 2-axis scanning device in place of the removable FlyGate apparatus was used to measure brightness inside the GlobeDisplay. Schematics for the device can be found here: `https://www.dropbox.com/sh/pscqxbsklpg2ece/AABIxubCtq4LyjhqqR6lMOGza?dl=0`. A small pinhole between the globe and the photodiode ensured that each measurement excluded ambient light and only included a radial region equivalent to a single fly ommatidium. Visual stimulus frames were displayed at 360 Hz using a modified DMD projector (DepthQ WXGA 360, Lightspeed Design, Bellevue, WA; modification by A. Leonardo). We further electronically and physically modified the projector to accommodate an LED light source as input via a light guide (SugarCUBE model M03-005, Nathaniel Group). A library of visual patterns was pre-generated, with each frame representing spherical space in terms of azimuth and elevation (Figure 2.4A). Note that while the hardware receives images as RGB frames, the projectors technically interpret frames in the order GBR. Because the spatial transformation (Figure 2.4B) is accomplished in real time on the GPU, visual stimuli can be targeted to any point on the globe by simply rotating the transformation matrix a few milliseconds prior to stimulus presentation. To target a stimulus precisely relative to the fly, its initial orientation on the recording platform was determined using FlyDetect and a 15-Hz live camera feed. Grating stimuli had a spatial period of 30° and rotated at 3 Hz for 3 seconds. Looming stimuli were designed to mimic a dark object on a light background approaching at constant velocity (v) with the angular size of the object on the flys retina (θ) as a function of time (t):

$$\theta(t) = \arctan\left(\frac{l}{v * t}\right) \tag{2.4}$$

The pattern of looming expansion is defined by l/v, which is the ratio of the approaching virtual objects radius (l) to its approach velocity (v) [53]. The data in Figure 2.10 was acquired using a looming stimulus with l/v = 40 ms, and the data in Figure 2.12 was generated with a uniform sampling from multiple values: 10, 20, 40, and 80 ms.

2.6.5 FlyPEZ throughput

Flies were automatically run through the assay at the rate of ∼2 flies/minute. Not all flies that emerged on the platform result in a downloaded video. Because downloading is a significant portion of experimental time, the initial video frame and stimulus feedback signal were evaluated first, and videos rejected if they did not contain a fly, contained multiple flies, or had a stimulus signal error. About two-thirds of the flies gated onto the platform, produced a downloaded video. Of these, 13% were discarded during manual curation (Figure 2.6B), and a further 5% were not trackable. Thus 82% of downloaded videos became useable tracked data. This means that, for experiments run with a vial of ∼100 flies, the FlyPEZ can produce nearly one useable trial per minute (Figure 2.5B). While a higher initial count maximizes throughput, more flies are unused and are possibly discarded (Figure 2.5C). These may be important considerations when designing an experiment.

2.6.6 Activation experiments

For optogenetic activation experiments, the FlyPEZ has four LEDs emitting a narrow wavelength appropriate for activation of genetically-encoded photoactivatable ion channels that open rapidly and depolarize neurons, potentially driving spikes. These LED lights are available at many wavelengths, making the system customizable for use with a range of available opsin tools [70, 81]. As a proof of principle, we have built the system with four LEDs of 624

nm wavelength, which is ideal for optogenetic activation of neurons expressing CsChrimson [81]. Each LED has a lens to focus its light over the glass platform, the intersection of which creates a $\sim$5 mm^3 zone of light exactly where a fly is centered in the camera view. Each light produces a maximum irradiance of 1.25 mW/mm^2, for a total maximum experimental irradiance of 5 mW/mm^2 from the four LEDs. The cuticle only transmits 9% of red light [79], meaning a neuron in our system may experience a maximum of 500 μW/mm^2, which is still greater than the 15 μW/mm^2 [81] or 82 μW/mm^2 [156] reported as effective in other optogenetic activation systems which bypass any cuticle. We wrote custom software to allow the user to create different experimental profiles for changes in light intensity and duration.

2.6.7 Data acquisition hardware

We acquired video data of fly responses using either an SA-4 or SA-X high-speed camera (Photron, San Diego CA). To achieve the desired image magnification, we used a 105 mm lens (Nikon, USA) with 12-mm extension tubes. When the lens f-stop is set to the maximum values that allow enough IR light through for recording (8 mm, SA4; 11 mm, SA-X), the depth of focus is 4 to 5 mm, which covers most of the 5 mm platform. A custom adapter ring fitted to the end of the lens attached a large prism used to collect the two fly views from the smaller prisms attached to the platform. We typically recorded fly responses at 6,000 frames per second (fps) saved to the cameras onboard RAM. Immediately after recording, videos were automatically downloaded to the control computer via a gigabit ethernet link. For a 600-ms video, the download time was typically 20-40 seconds, depending on the camera. Hence video download was a significant bottleneck to acquiring data faster. To increase download speed, the software initially downloads every 10th frame, determines the 50 segments in which the most motion occurs, and then downloads those 50 ten-frame segments (500 frames total) at the full rate (6,000 fps in most cases). In addition to the high-speed video capture, the cameras send a lower frame rate ($\sim$15 fps) live feed to computer running FlyDetect to automatically detect a fly and determines its body orientation. The control

computer was a high-end workstation (Dell Precision T7500, Dell, Round Rock, TX) and ran the data acquisition graphical user interface. All computers were operated using Windows 7 on a 64-bit processor. For managing the timing of stimuli and video recordings, and communicating with the control computer, we used a data acquisition board (NI-USB 6212, National Instruments, Austin, TX). See Figure 2.7 for more details about the hardware arrangement.

2.6.8 Data analysis and statistics

For the experiments in Figure 5, where a visual stimulus was presented from a single point in space, videos were excluded from analysis when the actual stimulus presentation error was greater than 30° in azimuth, caused by flies turning in the brief period between orientation measurement and stimulus display. This resulted in the removal of ∼15% of the tracked videos. The following behavior annotations were performed manually using a custom GUI (Figure 2.6C): frame of start of wing raising, frame of start of leg extension, frame of start of first downstroke, and frame of takeoff (when last tarsus leaves the ground or ceases to appear to bear weight). We define takeoff direction as the vector connecting the center of mass locations in the first frame of leg extension (which initiates the jump behavior) and the frame of takeoff. To control for any possible left/right bias, subsequent visual stimuli were presented alternately on the left or the right. Trajectories from experiments where the stimulus was presented on the right side of the fly were reflected to the left by post hoc transformation to remove left versus right distinctions. Because of this, while the center-of-mass trajectories could extend in any azimuthal direction, the visual stimulus is represented as 0° through 180°. All data acquisition and analysis software were written in MATLAB (Mathworks, Natick, MA) using the following toolboxes: Curve Fitting, Data Acquisition, Image Processing, Instrument Control, Optimization, Parallel Computing, Signal Processing, and Statistics and Machine Learning. Reverse saccades (Figure 2.8) were defined by the following two conditions: 1) the peak velocity exceed 90°/s and 2) the peak height to width

ratio is less than 0.3. Confidence intervals for binomial data in Figures 2.12C and D were computed using the Clopper-Pearson method, and hypothesis tests in Figure 2.12F were performed using a Mann-Whitney U-test for nonparametric comparisons of distributions. Further statistical details are included in the relevant figure captions. Interpolated 2D data representations in Figure 2.10 were generated from 2D histograms with dimensions in terms of azimuth and elevation, whose bins were evenly distributed in Euclidean space. The jump direction model goodness of fit was evaluated by generating a coefficient of determination (r^2) using the MATLAB function textitregstats, which compares the original data (x) to the linear model (y). Gaussian mixture models in Figure 2.12G were generated using MATLAB function textitfitgmdist, with initial conditions designed to produce equally weighted models which include 3 Gaussians.

2.6.9 Code and data availability

All design files and custom software required to manufacture and operate FlyPEZ, as well as custom software to curate, analyze, and visualize FlyPEZ data can be accessed here: `https://www.dropbox.com/sh/2maxxwysv8i3ui2/AACrrC9sL30ksxLq69AgZXMNa?dl=0`. Custom software was designed using MATLAB 2013b for PC. Videography data will be made available upon reasonable request.

2.7 Jump Direction Model Derivation

The model we propose consists of three 2D vectors with an origin at the center of the fly. The origin vector extends to the anterior of the fly. Vector $\vec{A}$ represents a theoretical jump directly away from the looming object, $\vec{F}$ is a theoretical jump forward (identical to the origin), and $\vec{R}$ is the actual jump direction. Our model proposes that $\vec{R}$ is the sum of the vectors $\vec{A}$ and $\vec{F}$ which are scaled by coefficients which add to a value of one using a single variable m. Each vector can be broken up into their components i and j. The vectors used

in the proposed model:

$$\vec{R} = (1-m)\vec{A} + (m)\vec{F} \tag{2.5}$$

are each comprised of their respective components (i) and (j).

$$\vec{R} = r_1 i + r_2 j \tag{2.6}$$

$$\vec{A} = a_1 i + a_2 j \tag{2.7}$$

$$\vec{F} = f_1 i + f_2 j \tag{2.8}$$

Using principles of trigonometry, the jump angle (α, Figure 2.10E) can be represented by:

$$\alpha = \arctan\left(\frac{r_2 j}{r_1 i}\right) \tag{2.9}$$

and the components of $\vec{A}$ (away from the stimulus) can be represented in terms of θ (the stimulus angle) by subtracting π to get

$$a_1 i = \cos(\theta - \pi) \tag{2.10}$$

$$a_2 j = \sin(\theta - \pi) \tag{2.11}$$

Since vector $\vec{F}$ is at the origin, its components are

$$f_1 i = 1 \tag{2.12}$$

$$f_2 j = 0 \tag{2.13}$$

By the form given by Eq. (2.5) and definitions given by Eq. (2.10) through Eq. (2.13), the components of vector $\vec{R}$ can be rewritten as

$$r_1 i = (1-m)\cos(\theta - \pi) + 1(m) \tag{2.14}$$

$$r_2 j = (1-m)\sin(\theta-\pi) + 0(m) \tag{2.15}$$

These components of $\vec{R}$ can now be used to define the jump angle (α) from Eq. (2.9) in terms of stimulus angle (θ)

$$\alpha = \arctan\left(\frac{(1-m)\sin(\theta-\pi)}{(1-m)\cos(\theta-\pi)+m}\right) \tag{2.16}$$

Divide all terms by $(1-m)$ gives

$$\alpha = \arctan\left(\frac{\sin(\theta-\pi)}{\cos(\theta-\pi)+\frac{m}{1-m}}\right) \tag{2.17}$$

By long division, Eq. (2.17) is simplified to

$$\alpha = \arctan\left(\frac{\sin(\theta-\pi)}{\cos(\theta-\pi)+\frac{1}{1-m}-1}\right) \tag{2.18}$$

The coefficient (m) is a linear function of stimulus angle (θ)

$$m(\theta) = (w * \theta) + c_1 \tag{2.19}$$

And (w) is a function of stimulus elevation (ϕ)

$$w(\phi) = (c_2 * \phi) + c_3 \tag{2.20}$$

The constants were empirically determined. By non-linear least squares analysis of the original data, for all elevations $c_1 = 0.44$. By linear regression of the three values obtained for w (see Figure 2.11B), $c_2 = -0.121$ and $c_3 = 0.13$.

2.8 Contributions

Work on the FlyPEZ project was performed by W. Ryan Williamson (W.R.W.), myself (M.Y.P.), Patrick Breads (P.B.), Brian Coop (B.C.), Grace Zhiyu Zheng (G.Z.Z.) and Gwyneth M. Card (G.M.C.). This chapter is adapted from a manuscript submission to the journal, Cell.

The first version of the FlyPEZ was designed, tested and prototyped by M.Y.P and G.M.C. The current version of the FlyPEZ, presented here, was designed, tested and built by B.C. and W.R.W. This newer version retained the same general design and fly handling mechanisms from the first version, but has significant improvements in: 1) durability by utilizing machined components, 2) efficiency in running experiments from integrated experimental control, and 3) stimulation capabilities from a mirror-based visual projection system.

For the work presented here, G.Z.Z., P.B., W.R.W. and M.Y.P. prepared the experimental flies. P.B., W.R.W. and M.Y.P. performed the FlyPEZ experiments. P.B. and W.R.W. curated and tracked the video data. W.R.W. made the figures. W.R.W., M.Y.P. and G.M.C. wrote the manuscript.

We had additional assistance from the Janelia Instrumentation, Development and Technology (ID&F) group, specifically from Magnus Karlsson, Steve Sawtelle, Bill Biddle and Spencer Taylor, in prototyping, debugging and iterating on the FlyPEZ design.

CHAPTER 3
CHARACTERIZATION OF DESCENDING NEURONS CONTROLLING VISUALLY-EVOKED FLY ESCAPES

3.1 Abstract

To avoid predation, nervous systems detect looming motion cues from a predator's approach to generate evasive responses . Looming-sensitive visual neurons and escape-evoking giant neurons have been identified in mobile species across the animal kingdom [42]. In flies, escape is composed of a sequence of movements to initiate flight: freezing, postural adjustment, wing elevation and wing depression with leg extension. These sub-behaviors determine critical properties of the escape. Postural shifts determine escape direction [23]. The giant fiber (GF) neuron's role in leg extension and wing depression for rapid takeoff has been well-characterized [155], indicating that additional, unknown descending neurons must contribute to the control of the other sub-behaviors in the sequence. In this study, we characterize a group of eight descending neurons (LC4DNs) which may control escape by serving as parallel signaling pathways, connecting the same regions in the brain and ventral nerve cord (VNC) as the GF. Specifically, this group of neurons extends dendrites to an optic glomerulus formed by the axon terminals of a looming-sensitive [156] visual projection neuron cell type called lobula columnar type 4 (LC4)[106]. In behavioral experiments, optogenetic activation of cell type-specific lines shows that select LC4DNs can evoke long-mode escapes, distinct from the GF-driven short-mode escapes. Whole-cell patch clamp recordings a subset of LC4DNs demonstrates similar looming-sensitivity and speed tuning, as would be expected from a common looming-sensitive input, like LC4. Finer analysis of LC4DN-activation reveals induced postural shifts that control escape direction, comparable to looming-evoked behavior. DNp11 activation generated forward jumps, whereas DNp02 and DNp04 co-activation induced backwards jumps. To determine a sensory input basis for directionality, we analyzed synaptic connectivity in an electron microscopy dataset [168] to

find inequalities in the number of synaptic connections between LC4 neurons and LC4DNs. Visualization of the LC4 dendrites reveals spatial gradients that are in opposite polarity to the activation-induced jump direction. These findings suggest a rapid feed-forward control mechanism by LC4DNs in which looming features are encoded by LC4 neurons and then filtered through a synaptic gradient that determines spatial selectivity of those features in specific DNs such that the fly generates postural shifts for escape away from the looming location.

3.2 Introduction

In response to threatening stimuli, animals generate startle and escape behaviors critical to their survival, which vary according to their body plan and ecology [42]. Because these behaviors are robust, they serve as useful experimental models for studying sensorimotor computations [32, 84, 48].

As in other species, the focus of study for the neural basis of escape in the fruit fly, *Drosophila melanogaster*, has been the giant fiber (GF) descending neurons (Figure 3.1A) [4, 60] (for more details about the GF system, see Chapter 1). Previous anatomical [120, 90, 85, 138] and physiological [90, 163, 101, 47, 155] studies establish the GF as a critical neuron for determining the mode of escape. A single GF spike evokes a short-mode escape, in which the flies do not fully raise their wings, and GFs are necessary for production of this takeoff pattern [155]. GFs can spike in response to looming stimuli [155], and can therefore be regarded as command neurons [86] for the short-mode escape pattern. Short-mode escapes trade off initial flight stability for escape speed [22] and are expected to occur more frequently during faster predator attacks [155]. In addition, the GFs may also drive a subset of long-mode escapes, in which wings are raised prior to a GF spike by other neurons [155]. Previous studies have demonstrated that this response derives from input by two specialized visual projection neuron types, LC4 [156] and LPLC2 [82], which are both looming-encoding and synapse directly to the GF lateral dendrite.

There is strong evidence that circuits outside the GF system also contribute to escape. Previous work in blowflies suggests that the GF is part of a cluster of DNs with overlapping LC4 dendrites whose axons projects to different areas of the VNC [100], indicating that other downstream neurons could also receive looming feature information and contribute to escape. As in zebrafish, ablation or inactivation of GFs reveals that escapes are still performed [91, 39, 155]; therefore, escape can be controlled by additional descending neuron pathways. Behavioral studies also suggest neural pathways in parallel to the giant fiber that could control wing raising prior to escape [61, 23, 155]. One study reported spiking responses dependent on looming stimulus angular size in extracellular neck recordings [50], and recently, a descending neuron (DNp09) has been characerized that controls the looming-evoked freezing sub-behavior [166]. These data, combined with the knowledge that the GF typically fires a single spike if it is active in looming-evoked escape [155], indicates that unknown looming-sensitive descending neurons could contribute to escape sub-behaviors. Of particular interest is the descending control of escape direction, which is a common feature of visually-evoked escapes across diverse species whose neural mechanisms are unexplored [39, 44, 124, 23] (also see Chapter 2). Directionality in flies comprises an integration of postural and visual information. Directional escapes arise from postural adjustments that shift the location of the fly's center of mass relative to its middle legs, which provide the force for jumping [105, 145, 25]. Once the posture is set, flies subsequently raise their wings and then extend their legs and depress their wings to takeoff. The direction of the jump, which determines the initial escape trajectory, is set by the earlier postural adjustments.

One hypothesis is that differences in visual drive to the left or right side of the animal could mediate left-right biases in descending neuron activity that generate a right or left escape [39]; however, forward and backward escapes require an additional mechanism to resolve degeneracy.

In this chapter, we use behavioral experiments, neural recordings, and electron microscopy (EM) ultrastructure analysis to investigate a set of recently-identified DNs that are

putative postsynaptic partners of the looming-sensitive LC4 cell type and have the potential to serve as parallel pathways to the GF for control of looming-evoked escape behaviors. We show that activation of a subset of LC4DNs is sufficient to elicit escape behaviors, including wing-raising, takeoff, and postural adjustments. We identify specific LC4DNs that drive forward and backward escape and show their input from LC4 is structured through opposite gradients of synaptic strength. This mechanism could form a representation for frontal and rear looming stimuli, and resolve the ambiguity in selecting forward or backward escape directions.

3.2.1 A study of fly descending neuron anatomy

One advantage of the fly model system is that most of its neurons are individually identifiable by their morphology and, with effort, precise brain circuits can be reconstructed with the expectation that similar arrangements will be found across individuals. A recently published study by my collaborator [106], Hiro Namiki, systematically characterized the morphology and connectivity of descending neurons in *Drosophila melanogaster*. This study is the most comprehensive description of fly descending neurons to date. Because a subset of the analysis is the starting point for finding parallel escape pathways, I will present here a summary of the relevant anatomical findings, with three accompanying figures adapted from his work.

The study characterized the anatomy of approximately half of the DNs in the fly nervous system. The analysis focused on determining the connectivity between sensory and motor neuropil in the brain and VNC by DNs. Over 100 split-GAL4 lines were generated to target specific DN cell types for both detailed anatomical and future functional investigation.

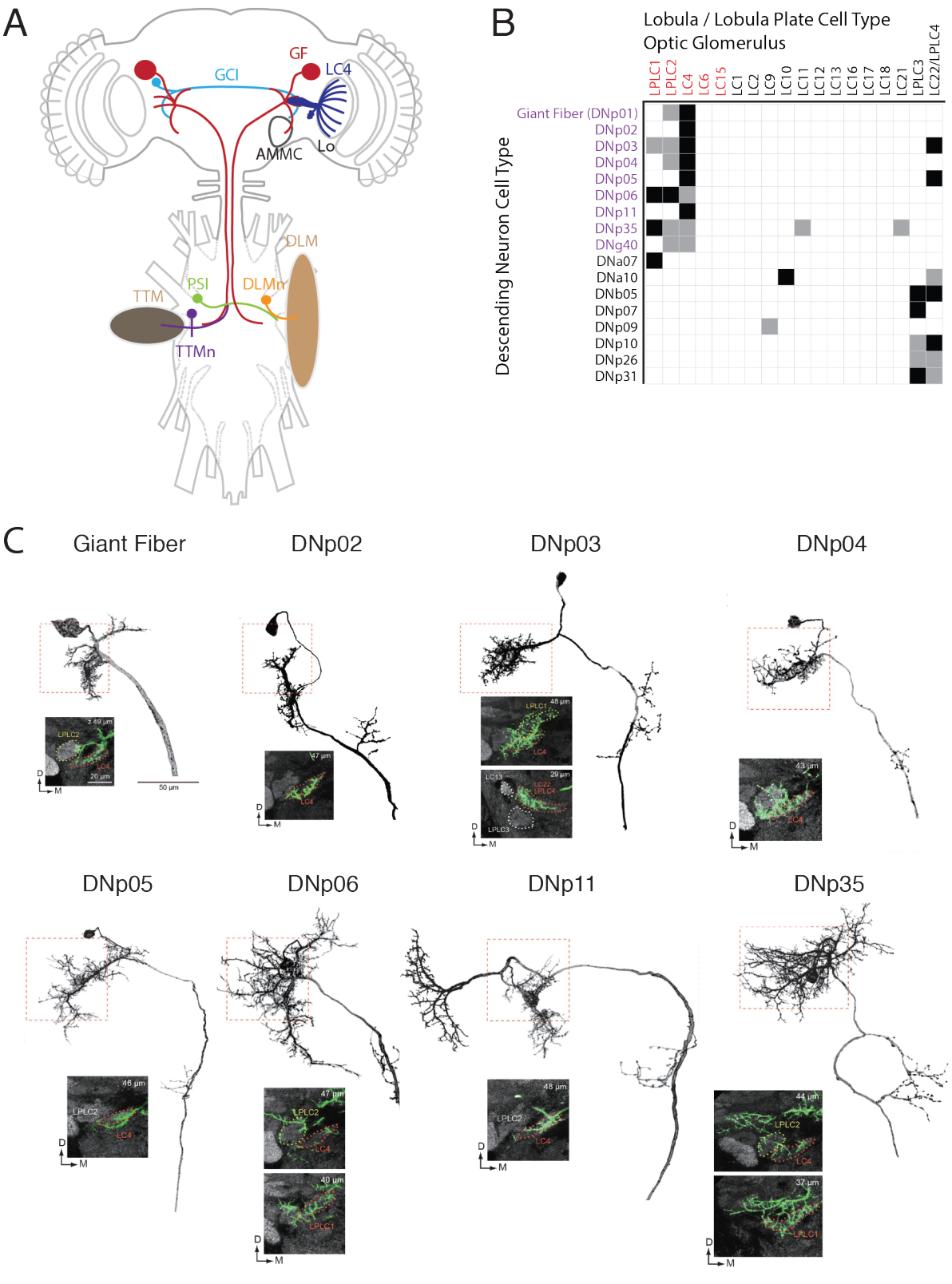

Figure 3.1: LC4DN Classification by Anatomical Analysis of Visual and Descending Neurons

Figure 3.1 *(previous page)*: LC4DN classification by anatomical analysis of visual and descending neurons
(A) Schematic of the giant fiber system. For detailed description see Chapter 1.
(B) Matrix of DN innervation in optic glomeruli formed by specific visual cell types. White, gray and black square entries indicate no, sparse and dense innervation. DNs with LC4 innervation, LC4DNs, are denoted in purple. Visual cell types previously reported [162] to elicit escape during optogenetic activation are denoted in red. Adapted from figure 12 of [106]
(C) Morphology of LC4DN innervation into the LC4 optic glomerulus. Traced neuron morphologies with insets of high-resolution (63x) confocal images at the depth of the LC4 glomerulus. Reproduced from figure 12 supplement 1 of [106].

LC4-cluster Descending Neurons (LC4DNs)

Using confocal imaging of individual DN morphology from the split-GAL4 lines, the locations of DN neurites in the brain were compared to those of the optic glomeruli, bundles of axon terminals from specific visual cell types that form readily identifiable clusters in nc82 synaptic counterstaining. DN innervation into 18 identified optic glomeruli was scored as strong, weak, or no innervation (Figure 3.1B,C). Most DN processes within the optic glomeruli had smooth branches, indicating that they are likely dendrites. The distribution of DN outputs from the optic glomeruli were heterogeneous, consistent with earlier reports from larger flies [139, 140]. (adapted from [106]). The optic glomeruli for LC4 and LC22 (also called LPLC4 [112, 162]) have strongly overlapping dendrites from the largest number of DNs (9 and 8, respectively). LC4 and its neighboring glomeruli, LPLC1 and LPLC2, form a densely innervated group in the ventral lateral protocerebrum. In contrast, the LC22 glomerulus forms a more posterior group with that of LPLC3. A functional study [162] reported escape phenotypes for LC4, LPLC1 and LPLC2 upon optogenetic activation, which suggests that this group could output to escape motor pathways through connected DNs. Furthermore, as described above, LC4 and LPLC2 provide visual looming information to the GF, suggesting that other downstream neurons could receive looming feature information as well. Previous work in blowflies suggests that the GF is part of a cluster of DNs with overlapping LC4 dendrites whose axons projects to different areas of the VNC, and thus may distribute information from LC4 to different motor pathways [100].

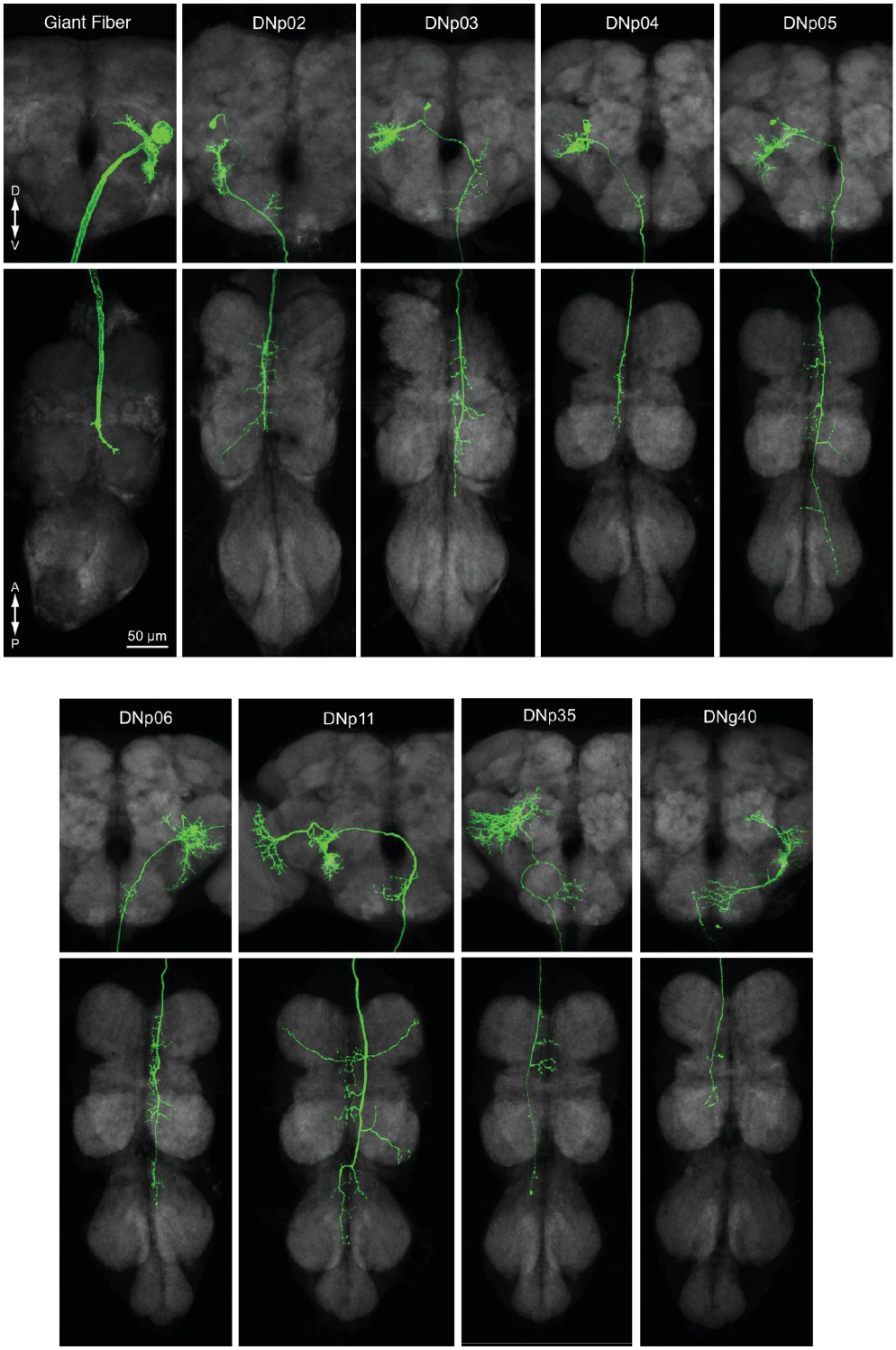

Figure 3.2: Morphlogy of LC4-Cluster Descending Neurons (LC4DNs)
Morphology of individual LC4DNs generated by masks of maximum intensity projections of confocal image stacks of sparse split-GAL4 lines. Adapted from figure 2 supplements 5, 8 and 12 of [106].

We focused our study on the group of nine identified DNs (including the GF) that innervate the LC4 optic glomerulus, and refer to these as the LC4DNs (Figure 3.2).

The LC4DNs have related but distinct VNC innervation. The VNC is composed of a layered system of neuropil, distinguishable by the appendages (legs, wings or halteres) they control (3.3A-B). An integrative region, involved in wing and leg control, called the lower tectulum is not well-described and has unknown function. It contains giant fiber system neurons, including the TTMn, PSI and axonal projections of the GF [80, 163]. Considering that escape involves driving both leg and motor activity, the lower tectulum may house other neurons involved in the escape behavior. Nine identified DNs project to the lower tectulum, including five of the LC4DNs (3.3C-E). While GF and DNp04 both project to the lower tectulum, other LC4DNs innervate other VNC neuropils, suggesting they could control different escape sub-behaviors or other loom-related behaviors.

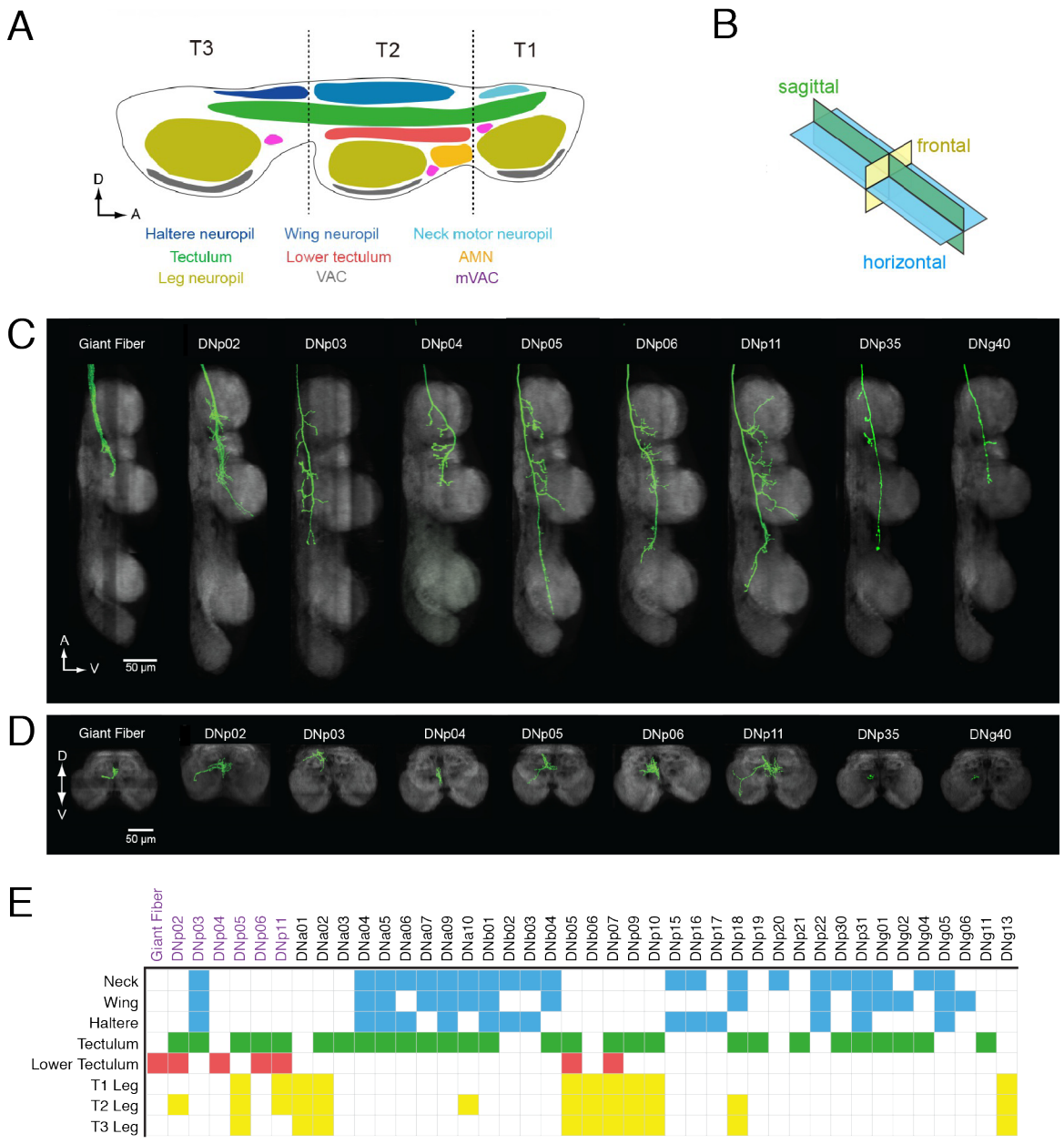

Figure 3.3: LC4DN Axon Projections into the Ventral Nerve Cord
(A) Schematic of VNC neuropil. T1 (prothoracic segment), T2 (mesothoracic segment), T3 (metathoracic segment). Reproduced from figure 4 of [106].
(B) Diagram of planes to describe VNC anatomical imagery.
(C) LC4DN axon projections in the VNC in sagittal views, which divides the lower tectulum. Reproduced from figure 13 of [106].
(D)Frontal views are focused at the mesothoracic neuropil.
(E) Matrix of DN innervation into VNC neuropils, grouped by dorsal neuropils (blue), tectulum (green), lower tectulum (red), leg neuropils (yellow) [137]. LC4DNs denoted in purple text. Adapted from figure 15 of [106].

For this study, we utilized a set of split-GAL4 reagents for the LC4DNs. These driver lines were generated by the Janeila Descending Interneuron Team Project. Expression in the brain and VNC was imaged by standard immunohistochemistry methods (see [106]). We selected a subset of lines with robust expression in target LC4DNs and low off-target expression in at least 3 imaged samples of the brain and VNC (Figure 3.4). Two of the lines express in multiple LC4DN cell types: [DNp02, DNp04] and [DNp02, DNp04, DNp06]. In addition, a driver line useful as a control, the empty brain split, was generated with nearly no expression in the nervous system. With these driver lines, we looked to start experiments characterizing LC4DN function.

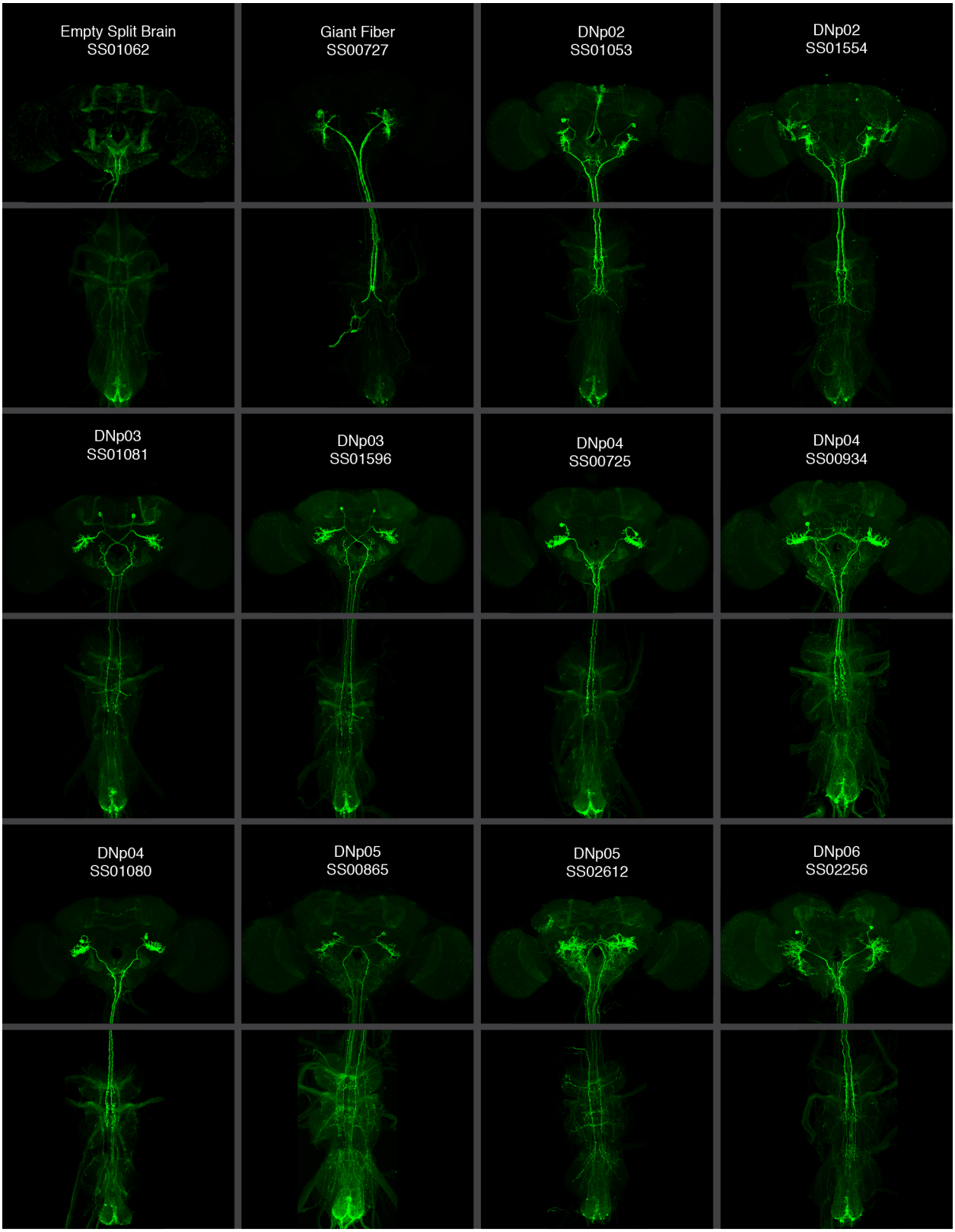

Figure 3.4: LC4DN Split GAL4 Line Expression (Page 1/2)

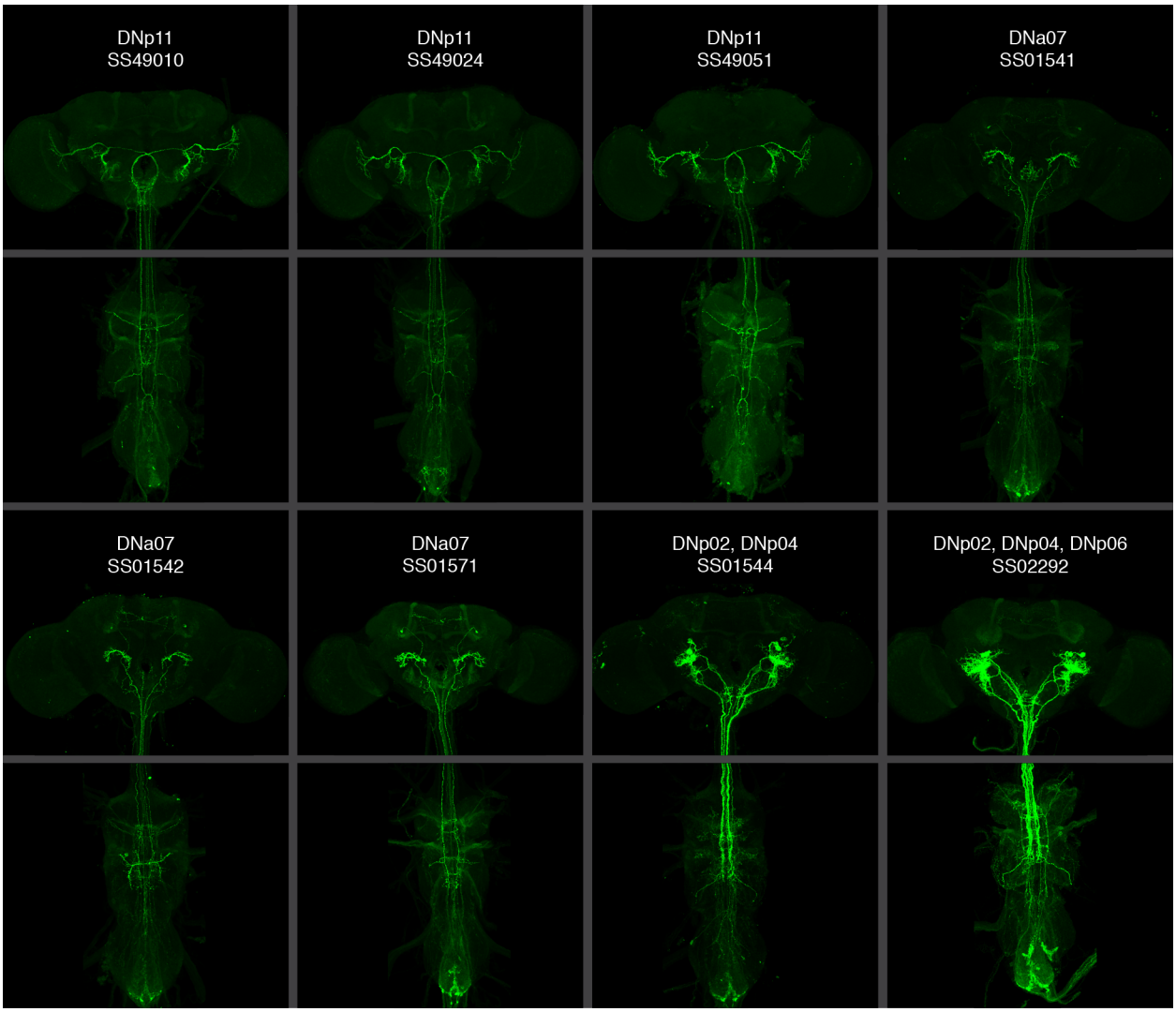

Figure 3.4: LC4DN Split GAL-4 Line Expression (Page 2/2)
Morphology of split-GAL4 lines utilized in this study. Maximum intensity projections of brain and VNC confocal image stacks (green channel) of split-GAL4 lines expressing membrane-bound GFP (green). Images are representative of the expression pattern (minimum 3 flies checked).

3.3 Results

3.3.1 LC4DN activation and silencing experiments

To begin to determine whether LC4DNs play a role in escape behavior, we performed optogenetic activation with the FlyPEZ. For each split-GAL4 line, we drove expression of the red-shifted channelrhodopsin CsChrimson [81] and stimulated freely-behaving flies with a 50 ms red light pulse. Responses of individual flies were captured automatically in 6000 frames-per-second videos. A tracking algorithm, described in Chapter 2, estimated takeoff rates within a 250 ms window of the start of activation. Figure 3.5A shows the two GF lines produced takeoff rates of over 90%, consistent with previous studies [155, 156]. In comparison to the empty brain split control, we also found significant increases for DNp04, DNp11, as well as two multi LC4DN lines which contain [DNp02, DNp04] together and [DNp02, DNp04, DNp06] together (normal approximation to the binomial, see Table 3.1). For DNp02, DNp04 and DNp11, multiple split-GAL4 lines were generated, and increases in takeoff were consistent across lines.

We further analyzed the video data to measure the escape duration between the last two escape sub-behaviors: wing raising and takeoff. As discussed in previous chapters, wildtype flies exhibit a bimodal distribution in the time between the sub-behaviors, on a log scale scale. The GF is necessary and sufficient to produce a short-mode escape, in which the wings are not fully raised prior to takeoff. For GF activation, the escape duration is less than 7 ms. In GF-silenced flies, short-mode escapes are absent, and the escape duration is greater than 7 ms.

For each LC4DN with significant increases in activated takeoff rate, we used the annotation GUI described in Chapter 2 to measure the escape duration. We denoted the video frame at the start of wing raising and the frame where the legs leave the ground, following the procedure previously established [155]). We found that the GF generates short-mode escapes, as expected, but DNp04 and DNp11 generate almost exclusively long-mode escapes

(>7 ms) (Figure 3.5B-C, Table 3.1). These long-mode escapes are characterized by fully-raised wings before takeoff, so activity in DNp04 and DNp11 drives both the wing raising and takeoff escape sub-behaviors. The escape duration is highly variable (Figure 3.5B has log scale time basis), but comparable with the long-mode escapes produced by GF-silenced flies.

The two multi LC4DN driver lines produced both short and long-mode escapes (Figure 3.5C). Both lines contain DNp02, whose solo activation does not elicit escapes, and DNp04, which elicits long-mode escapes. One line also contains DNp06, which also does not elicit escapes. Both lines have a higher escape rate than activating only DNp04 (Figure 3.5B), suggesting that co-activity in these neurons further increases drive to downstream escape motor circuits. Some escapes are long-mode, as expected from DNp04 activation, but others are short-mode, which suggests that the GF system is recruited in a subset of trials. The short-mode is not elicited in any other of the individual non-GF LC4DN activation experiments.

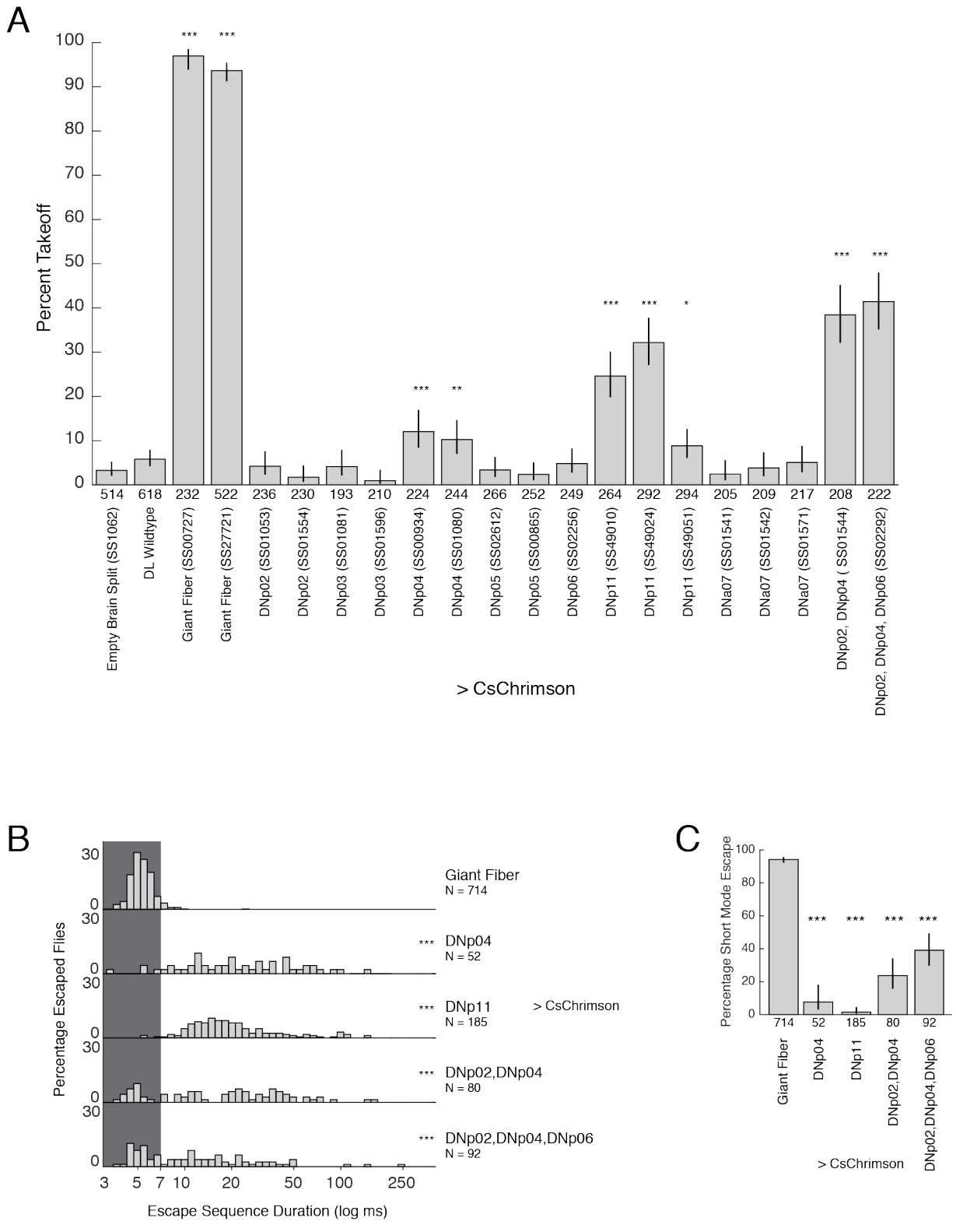

Figure 3.5: Optogenetic Activation of Specific LC4DNs Elicits Long-Mode Escape

Figure 3.5 *(previous page)*: Optogenetic activation of specific LC4DNs elicits long-mode escape
(A) Percent of flies that performed a takeoff in response to CsChrimson optogenetic activation in the FlyPEZ assay. Statistics: error bars, Wilson score interval; n listed below bars; normal approximation to binomial Z-test; Bonferroni correction *post hoc*; * $p < 0.05$, ** $p < 0.01$, *** $p < 0.001$, compared to control (empty brain split x CsChrimson).
(B) For DNs that can elicit escape upon activation, histograms of the duration between the wing raising and takeoff jump sub-behaviors. Escape trials combined from split-GAL4 lines for each DN cell type. Short-mode escape duration (0 to 7 ms, gray shaded region) and long-mode escape duration (>7 ms, white), as established in [155]. Statistics: n as listed; Wilcoxon rank sum test, Bonferroni correction *post hoc*, *** $p < 0.001$, compared to giant fiber.
(C) Percentage short-mode activated escapes. Statistics: error bars, Wilson score interval; samples as in B, n listed below bars; normal approximation to the binomial Z-test, (Table 3.1); Bonferroni correction *post hoc*; *** $p < 0.001$, compared to giant fiber.

To determine if LC4DN activity is necessary for escape, we drove expression of Kir2.1 [10, 116] with the LC4DN driver lines. Using the FlyPEZ, we measured escape rates to looming stimuli at four expansion rates (l/v = 10, 20, 40, 80 ms) (Figure 3.6). Looms were centered 90° to the left or right of the fly at an elevation 45° from the horizon. For a positive control, we tested an L1 and L2 lamina cell type driver line that is motion blind when silenced. As previously reported [155], GF silencing did not reduce escape rate in comparison to the empty brain split control. We did not find consistent differences in silenced LC4DN lines either (Table 3.2). This finding supports the idea that multiple DN pathways for loom-evoked escape form a redundant system that maintains escape probability.

To find any deficits in the duration of escape in LC4DN silenced flies, we annotated videos, as before, and evenly pooled data over the four looming rates (Figure 3.7A). We found that GF-silenced flies generate predominately long-mode escape, as reported previously [155], and that other LC4DN-silenced flies are not significantly different from empty brain split controls. Given that both DNp04 and DNp11 generate long-mode escapes in activation, it is not particularly surprising that we do not observe a long-mode deficit in silencing each individually. These observations indicate that long-mode escape is controlled by at least two pathways.

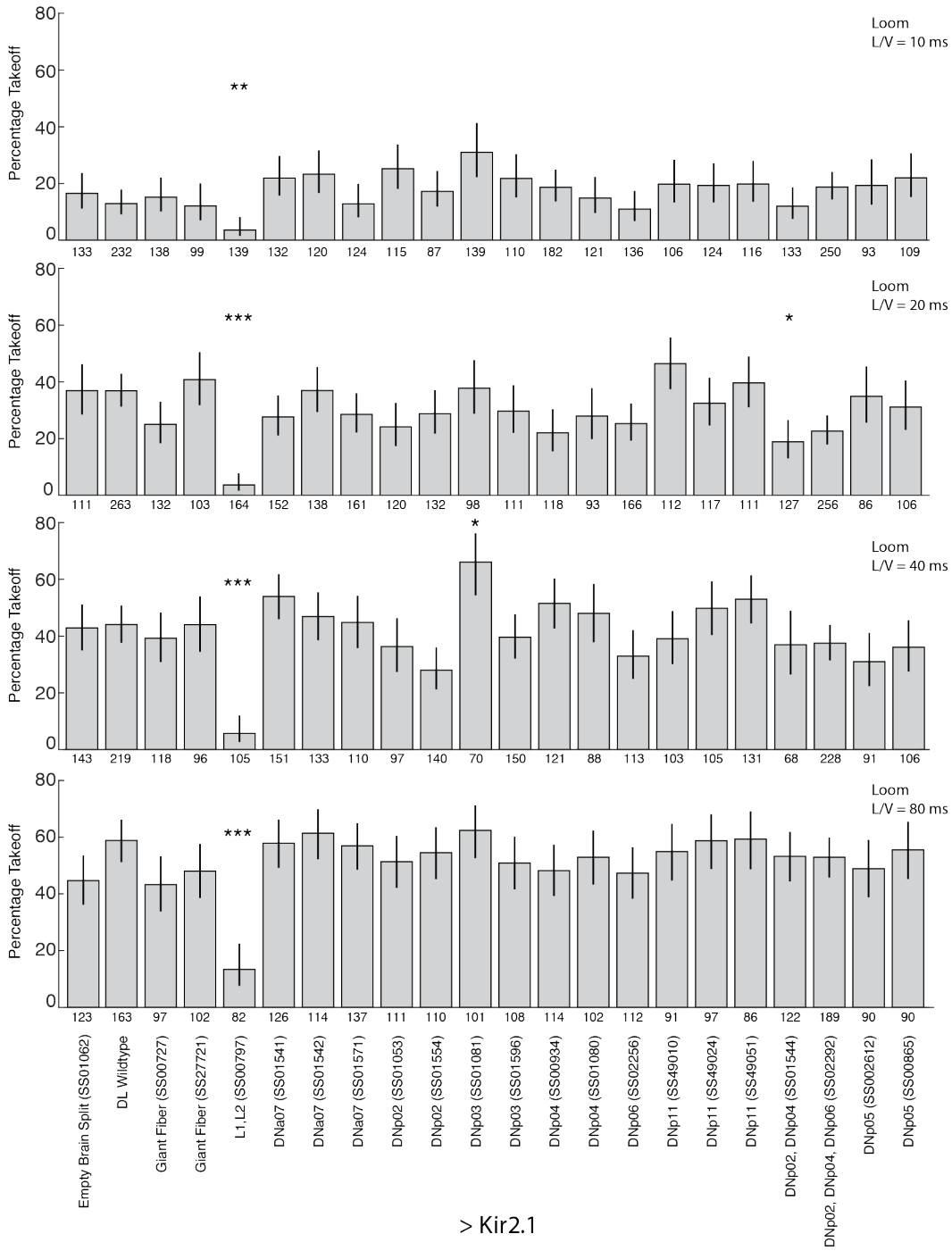

Figure 3.6: LC4DN Silencing Does Not Reduce Takeoff Rate
Neuronal silencing experiments with KIR2.1. Percentage of flies which performed a takeoff to a looming visual stimulus (azimuth = 90°, elevation = 45°) at four looming rates (l/v = 10, 20, 40, 80 ms). Statistics: error bars, Wilson score interval; n listed below bars; normal approximation to the binomial Z-test (Table 3.2); Bonferroni correction *post hoc*; * $p < 0.05$, ** $p < 0.01$, *** $p < 0.001$, compared to control (empty brain split x KIR).

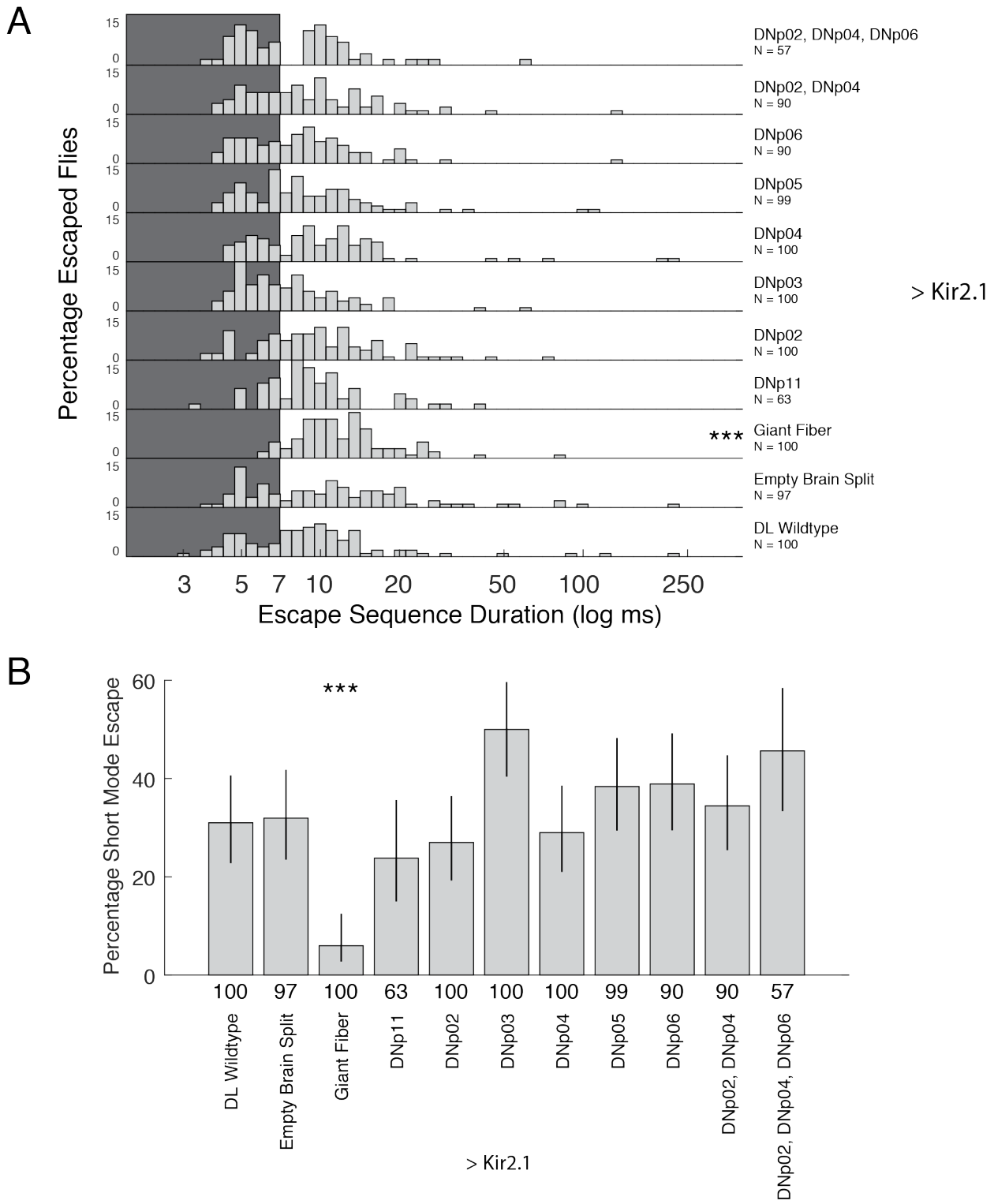

Figure 3.7: LC4DNs are Not Necessary for Long-Mode Escapes

Figure 3.7 *(previous page)*: LC4DNs are not necessary for long-mode escapes
(A) Histograms of the duration between the wing raising and takeoff jump sub-behaviors. Loom-elicited escape trials combined from split-GAL4 lines for each DN cell type. Short-mode escape duration (0 to 7 ms, gray shaded region) and long-mode escape duration (>7 ms, white). Statistics: n as listed; Wilcoxon rank sum test, Bonferroni correction *post hoc*, * $p < 0.05$, *** $p < 0.001$, compared to control (empty brain split x KIR).
(B) Percentage short-mode loom-elicited escapes. Statistics: error bars, Wilson score interval; samples as in A, n listed below bars; normal approximation to the binomial Z-test, (Table 3.3); Bonferroni correction *post hoc*; *** $p < 0.001$, compared to giant fiber.

3.3.2 Electrophysiological characterization of select LC4DNs

Following the observation that the [DNp02, DNp04, DNp06] driver line has higher rates of activated escape than DNp04 alone, we investigated the visual tuning properties of DNp02, DNp04 and DNp06 using *in vivo* whole-cell patch clamp electrophysiology. We displayed dark looming stimuli (45° elevation, 45° azimuth) and observed bursts of spikes riding on stimulus-locked depolarizations during the expansion phase of the stimulus (Figure 3.8). Loom responses were consistent across recordings for each cell type (Figures 3.9, 3.10, 3.11). Across cell types, the highest spike rates were produced at the fastest looming rates (l/v = 10 ms). Overall, DNp04 generated the highest spike rates to looming stimuli, followed by DNp06 and DNp02. The responses in all three LC4DNs recorded indicates that these LC4DNs are coactive during looming stimuli, and so activation of [DNp02, DNp04, DNp06] may be a rough and limited approximation of motor recruitment during loom-evoked of escape. The shared sensitivity to looming stimuli suggests that the putative LC4 input could drive the LC4DNs as a loom-sensitive population.

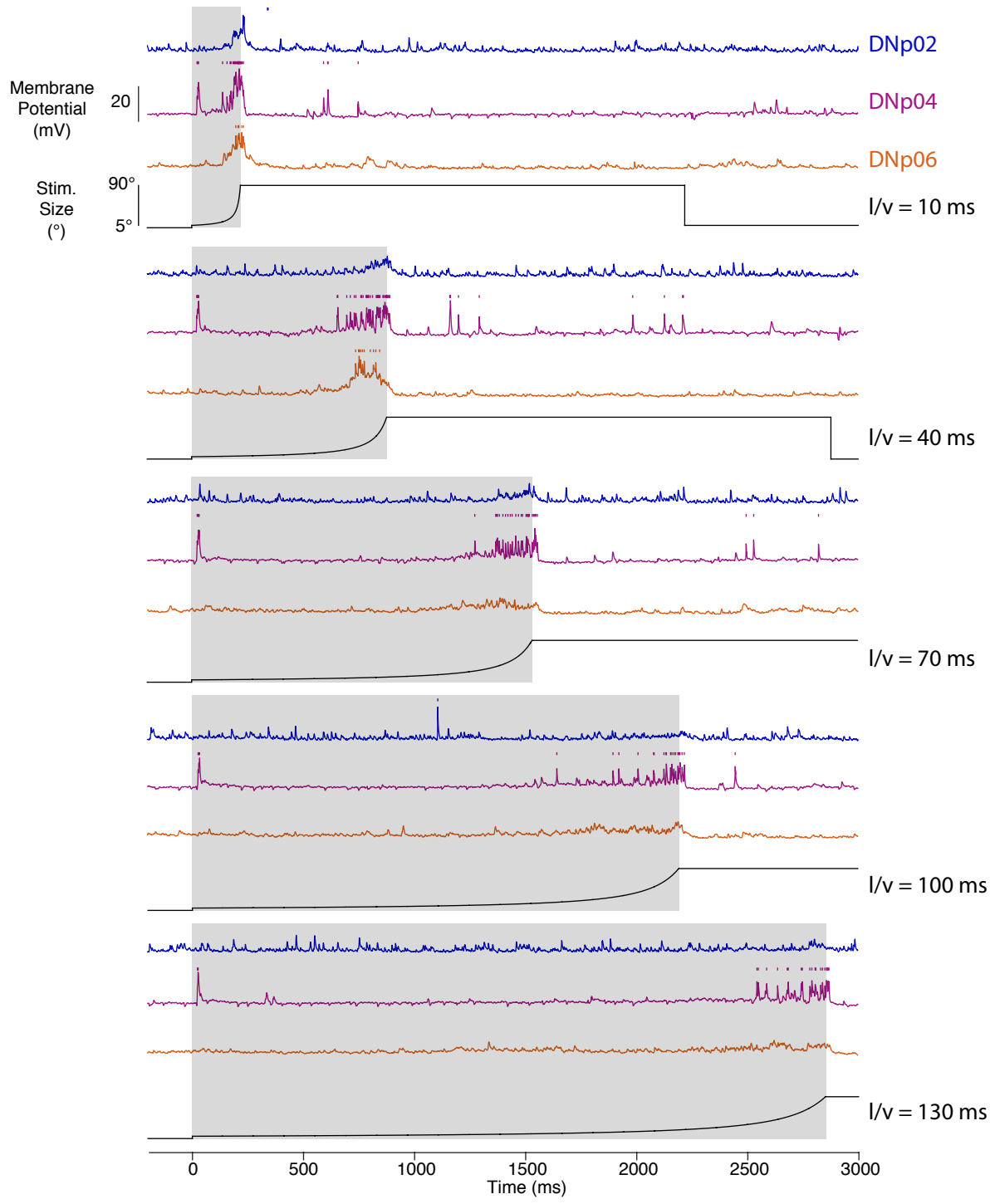

Figure 3.8: LC4DNs Spike in Response to Rapid Looming Stimuli
Traces from whole-cell patch clamp recordings of the membrane potential of DNp02 (blue), DNp04 (purple) and DNp06 (orange) in response to looming visual stimuli (size: 5° to 90°, azimuth = 45°, elevation = 45°) at five looming rates (l/v = 10, 40, 70, 100, 130 ms). Spike raster dots above traces. Shaded regions indicate time period of stimulus expansion. Looming stimuli held at 90° for 2000 ms.

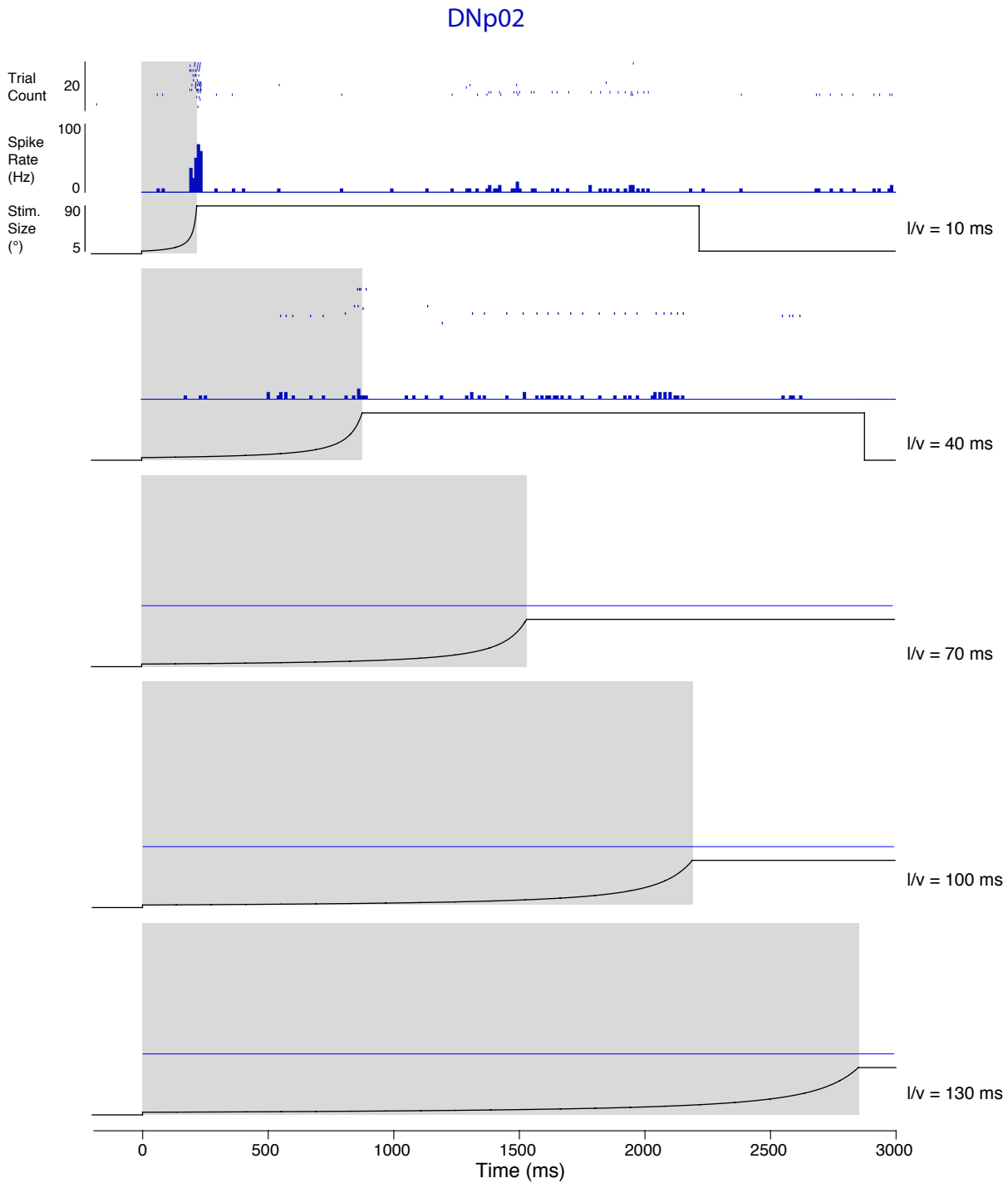

Figure 3.9: Summary of DNp02 Loom Responses
DNp02 spike raster and peri-stimulus time histograms (50 ms bins) for responses to looming stimuli (azimuth = 45°, elevation = 45°, l/v = 10, 40, 70, 100, 130 ms). Gray shaded region indicates time period of looming expansion. 5 flies, 4 trials each.

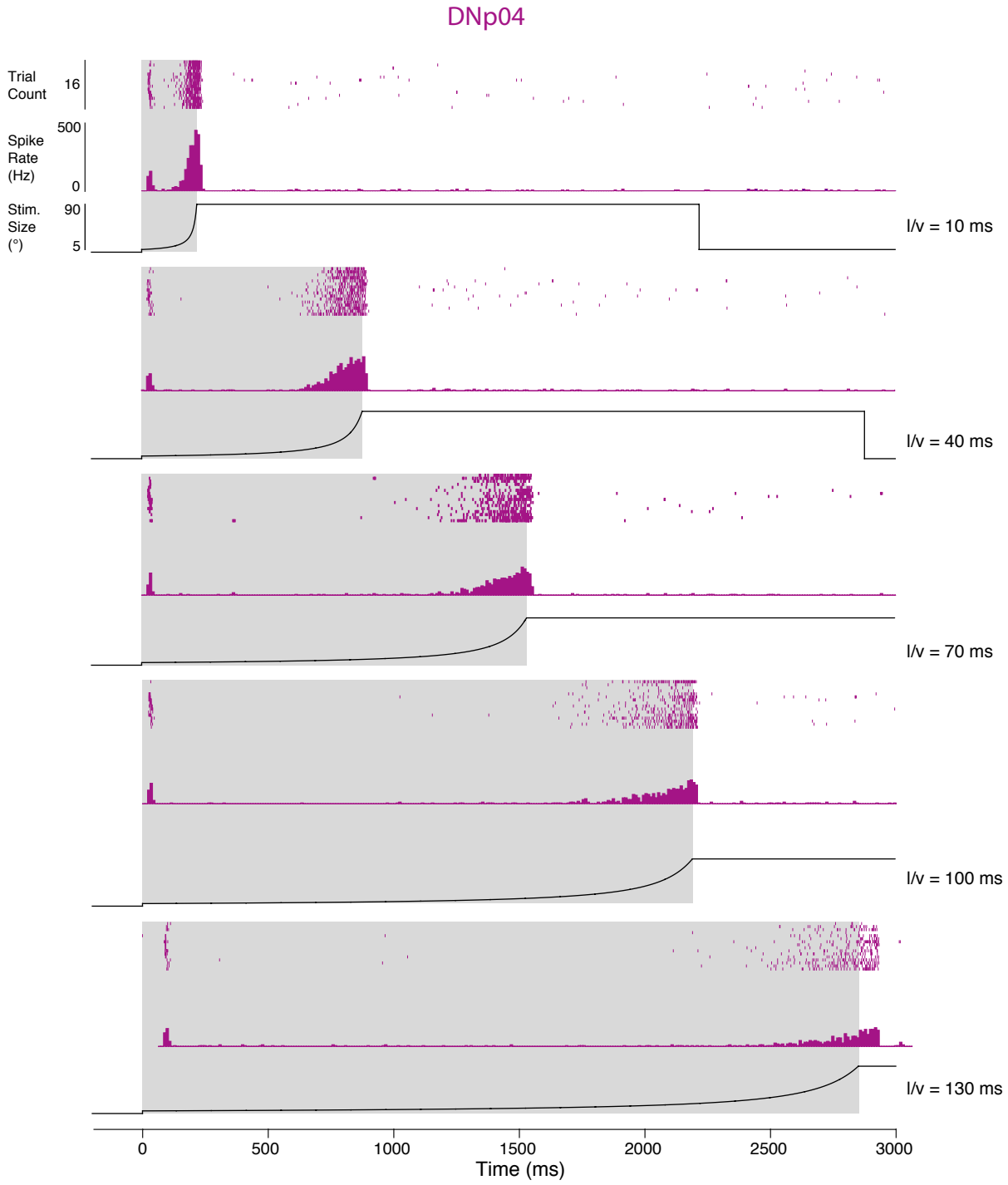

Figure 3.10: Summary of DNp04 Loom Responses
DNp04 spike raster and peri-stimulus time histograms (50 ms bins) for responses to looming stimuli (azimuth = 45°, elevation = 45°, l/v = 10, 40, 70, 100, 130 ms). Gray shaded region indicates time period of looming expansion. 4 flies, 4 trials each.

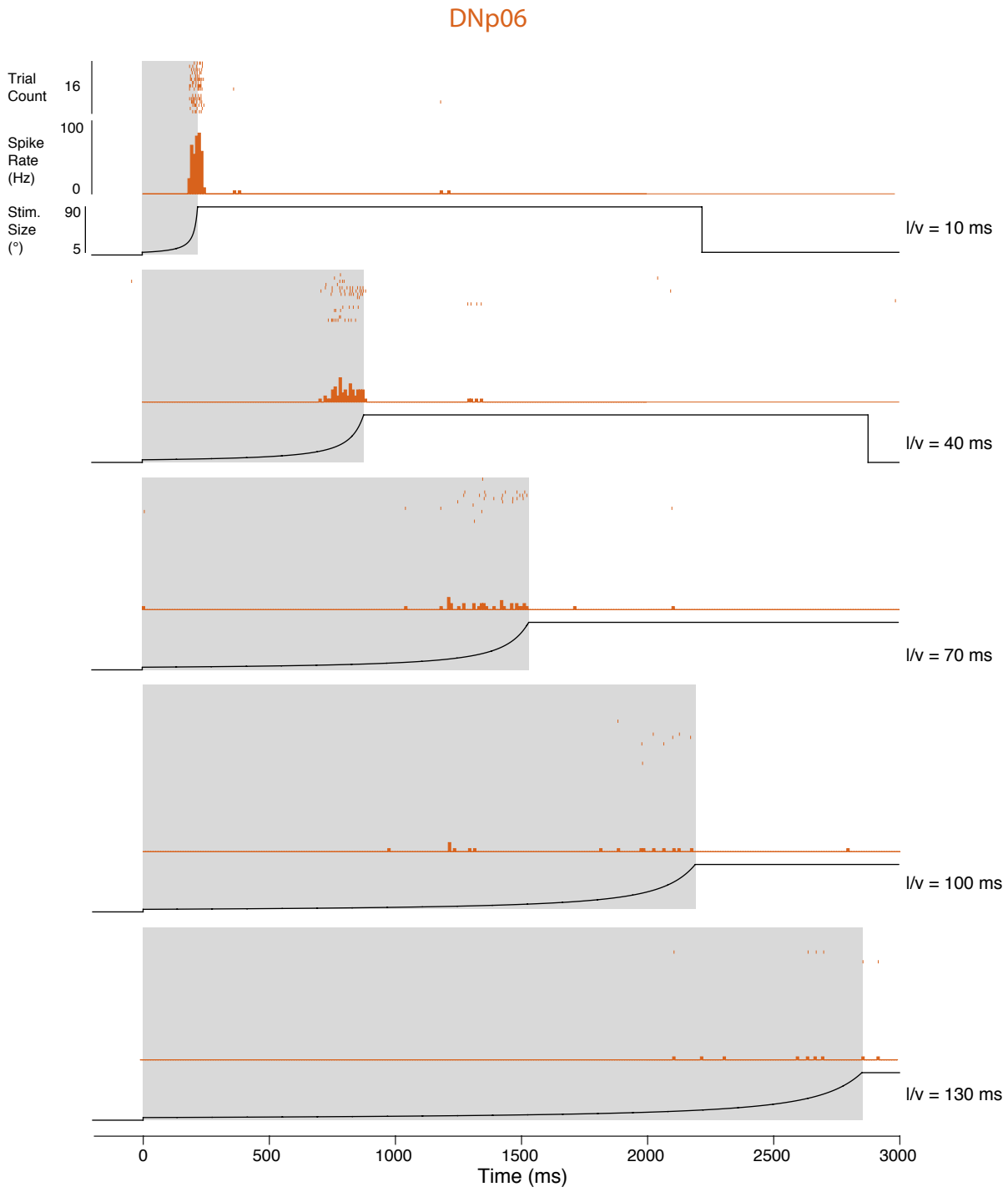

Figure 3.11: Summary of DNp06 Loom Responses
DNp06 spike raster and peri-stimulus time histograms (50 ms bins) for responses to looming stimuli (azimuth = 45°, elevation = 45°, l/v = 10, 40, 70, 100, 130 ms). Gray shaded region indicates time period of looming expansion. 4 flies, 4 trials each.

3.3.3 Directional analysis of evoked escapes

The spiking responses to looming stimuli indicate that LC4DN activity could contribute to the sub-behaviors observed during loom-evoked escape. We analyzed FlyPEZ optogenetic activation videos further to determine if other sub-behaviors such as postural adjustments are elicited. Because lines express pairwise in LC4DNs, we expect bilateral activation to shift fly posture in a forward or backward, but not lateral, direction. Previous work [23] found that the position of the middle legs relative to the fly center of mass is critical in determining the escape direction. To quantify this in FlyPEZ high-speed videos of LC4DN optogenetic activation, we annotated video frames every 5 ms from the start of the activation light pulse to 100 ms, every 5 ms. In each frame, we selected the location of the tips of the middle leg tarsi and tracked the center of mass point using an automated algorithm (see Chapter 2) to determine the angle, α, formed between the three points. (Figure 3.12A). Values of alpha greater or less than 180° indicate a forward or backward shift, and are predicted to set forward and backward takeoff direction, respectively (Figure 3.12B).

We found that flies typically rest on the FlyPEZ filming platform with legs angled relative to the center of mass within a range of $150^\circ < \alpha < 240^\circ$. For GF activation, flies escaped about 25 ms after the start of light pulse and did not change α (Figure 3.12C). GF activity does change body posture, as expected from its known function (see Chapter 1). Similarly, DNp04 and the empty split brain control did not show a consistent change in α. Both DNp02 and [DNp02, DNp04] decrease α between 25 ms and 50 ms, indicating that the center of mass has moved posterior relative to the middle legs due to DNp02 activation. DNp11 shows the opposite trend, with α values increasing over the same time window, indicating a forward shift. The magnitude of the forward and backward shifts are significant compared to control (Figure 3.12D).

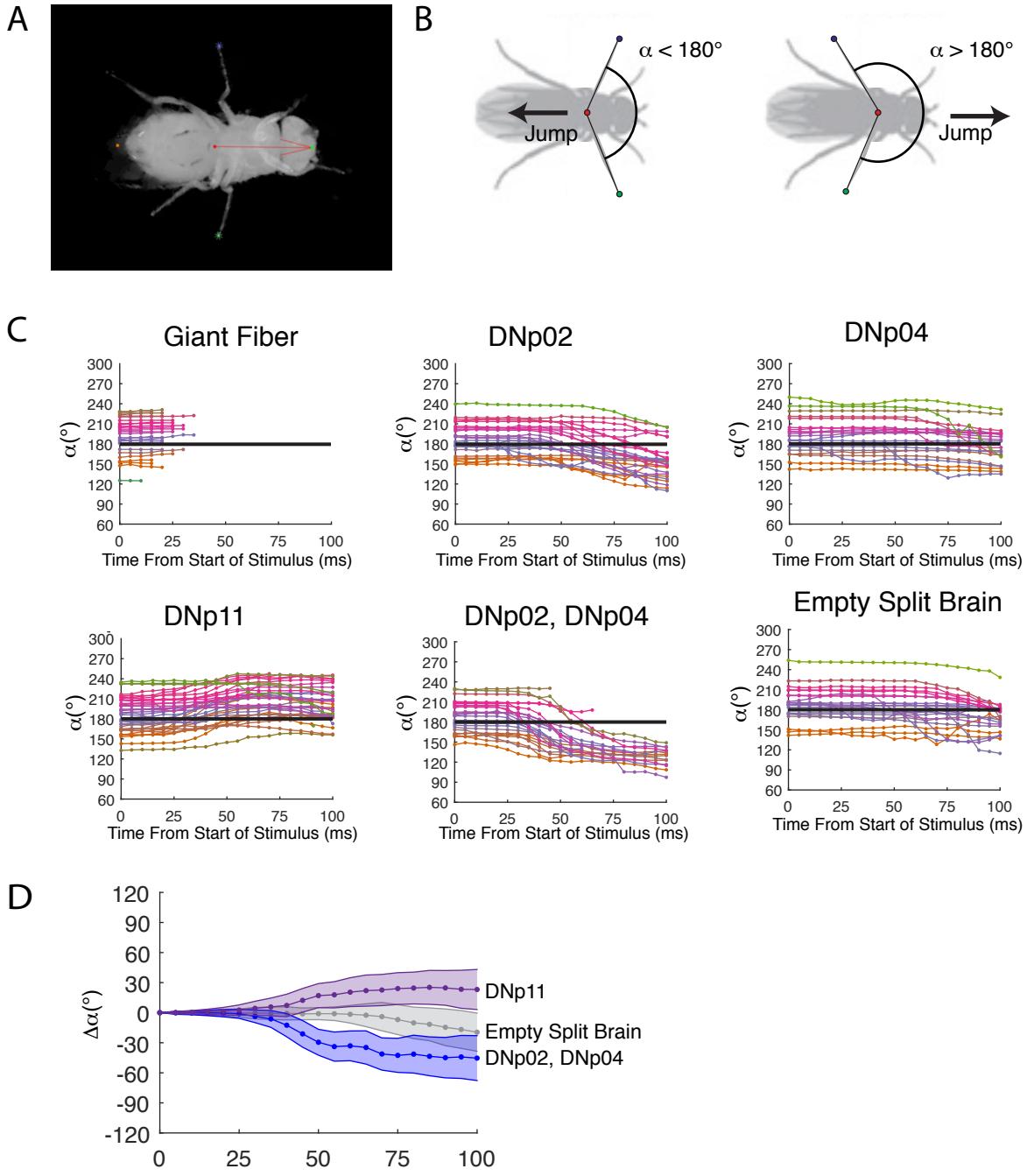

Figure 3.12: Activation of DNp02 and DNp11 Induces Body Position Shifts
(A) Representative video frame from the FlyPEZ showing the ventral view of the fly. Manually annotated mesothoracic leg tip positions (blue, green stars). Automatically tracked (FlyPEZ algorithm) center of mass (red dot) and orientation (red arrow).
(B) Schematic of the fly orientation. The position of the leg tips relative to the center of mass is defined by the angle, α.
(C) α, calculated from annotations, for the first 100 ms of LC4DN activation experiments. For each fly, traces are colored by initial α value. Traces stop short of 100 ms if the fly escapes.
(D) Mean changes in α Statistics: confidence interval, shaded region; n as shown, Mann-Whitney test, [DNp02, DNp04] to empty brain split: p = 1.6E-14, DNp11 to empty brain split: p = 7.6E-4.

The measured postural shifts predict the directionality of elicited escape trajectories. For GF and DNp04, no shifts predict no average bias in escape trajectories. For DNp11, forward shifts predict forward directed escapes, and for DNp02, backward shifts predict backward escape. Activation of DNp02 does not by itself elicit escapes. Instead, we analyzed [DNp02, DNp04]. By decomposition of shifts observed by DNp02 and DNp04 individually, we predict that DNp04 provides no bias and DNp02 contributes to the backwards shift observed from [DNp02, DNp04].

To measure initial escape trajectories, we used a tracking algorithm to find the center of mass position from the start of leg extension through liftoff from the platform. We analyzed flies that escaped within 100 ms of the light pulse and found mean trajectories predicted by the postural shifts. Both GF and DNp04 do not have a directional bias, consistent with no postural shifting. DNp11 and [DNp02, DNp04] showed forward, and backward escape trajectories, respectively. Because DNp02 appears to be setting the postural shift, the parsimonious explanation is that DNp02 activity generates a backward shift that causes a backward escape.

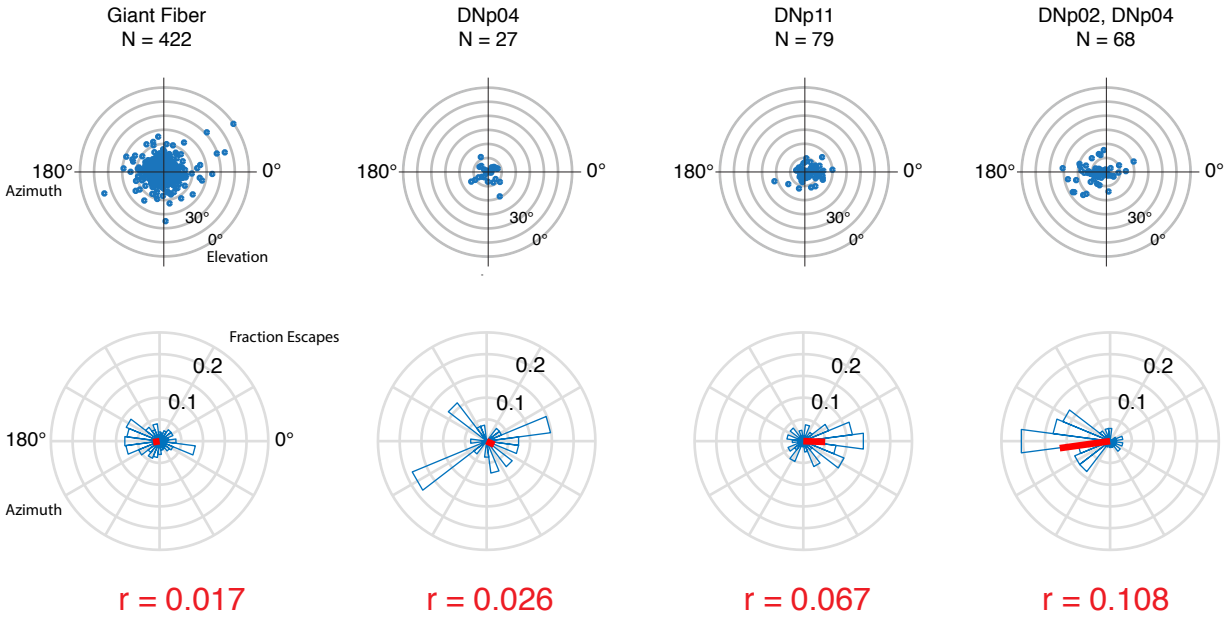

Figure 3.13: DNp02 and DNp11 Evoked Body Shifts Determine Escape Direction
(A) Schematic of the expected jump direction, as established by [23].
(B) Spherical scatter plot of the tracked escape direction for LC4DNs which elicit escape.
(C) Radial histogram of the escape azimuth. Radial mean (red line). Statistics: Hodges-Ajne test for non-uniformity of circular data. N as shown. DNp11: p = 4.5E-3, [DNp02,DNp04]: p = 3.6E-6.

3.3.4 Characterization of the synaptic connectivity of LC4DNs

If DNp02 and DNp11 can control opposite escape directions but both receive input from LC4, how might their visual inputs differ in order to be active in appropriate circumstances? We next aimed to assess the spatial sensitivity to looming stimulus position. It is currently unclear if visual spatial information is retained as the retinotopically distributed LC4 neurons project their axons in a seemingly disordered fashion to form the optic glomerulus [162] where the LC4DNs putatively take input. Namiki, et al. [106] reported biases in the spatial location of LC4DN neurites within the LC4 glomerulus [106], suggesting that each LC4DN could form biases in connectivity in different regions of the LC4 optic glomerulus. Given that the glomerulus is seemingly spatially unstructured in its representation of visual space, it is difficult to predict the organization of LC4 inputs to LC4DNs.

To explore this mystery, we traced the LC4 neurons, as well as DNp02, DNp04 and DNp11 in one brain hemisphere of an electron microscopy brain dataset [168] (Figure 3.14A). We marked synapses between each of 55 LC4 neurons and each DN (Figure 3.14B). We found a wide range in the number of synapses formed by individual LC4 neurons onto a given LC4DN (rainbow color scale). Taking synapse count as a measure of connection strength, we applied a color map to label each LC4 and its synapses to determine if there is a spatial bias for connectivity strength within the glomerulus. We did not find a recognizable pattern at the glomerulus for any of the DNs; however, coloration of the LC4 dendrites in the lobula reveals a spatial gradient that is distinct for each of the LC4DNs (Figure 3.14C-D).

DNp02 and DNp11 have gradients of opposite valence. The visual region with the highest predicted LC4 input strength to DNp02 is in the anterior field, and vice versa for DNp11. A simple model based on these predictions and the observations from activation experiments. When a fly sees a frontal looming stimulus, anterior LC4s provide relatively more drive to DNp02, which produces a postural shift that will generate a backwards escape trajectory. Takeoffs are generated by co-activity in GF, DNp04 or other escape pathways. For a looming stimulus directed from behind the fly, posterior LC4s become active and drive DNp11 to generate postural shifts and a forward-directed takeoff. Although activation indicates DNp11 can induce takeoffs, co-activity in GF and DNp04 could elicit directed takeoffs if DNp11 set the posture.

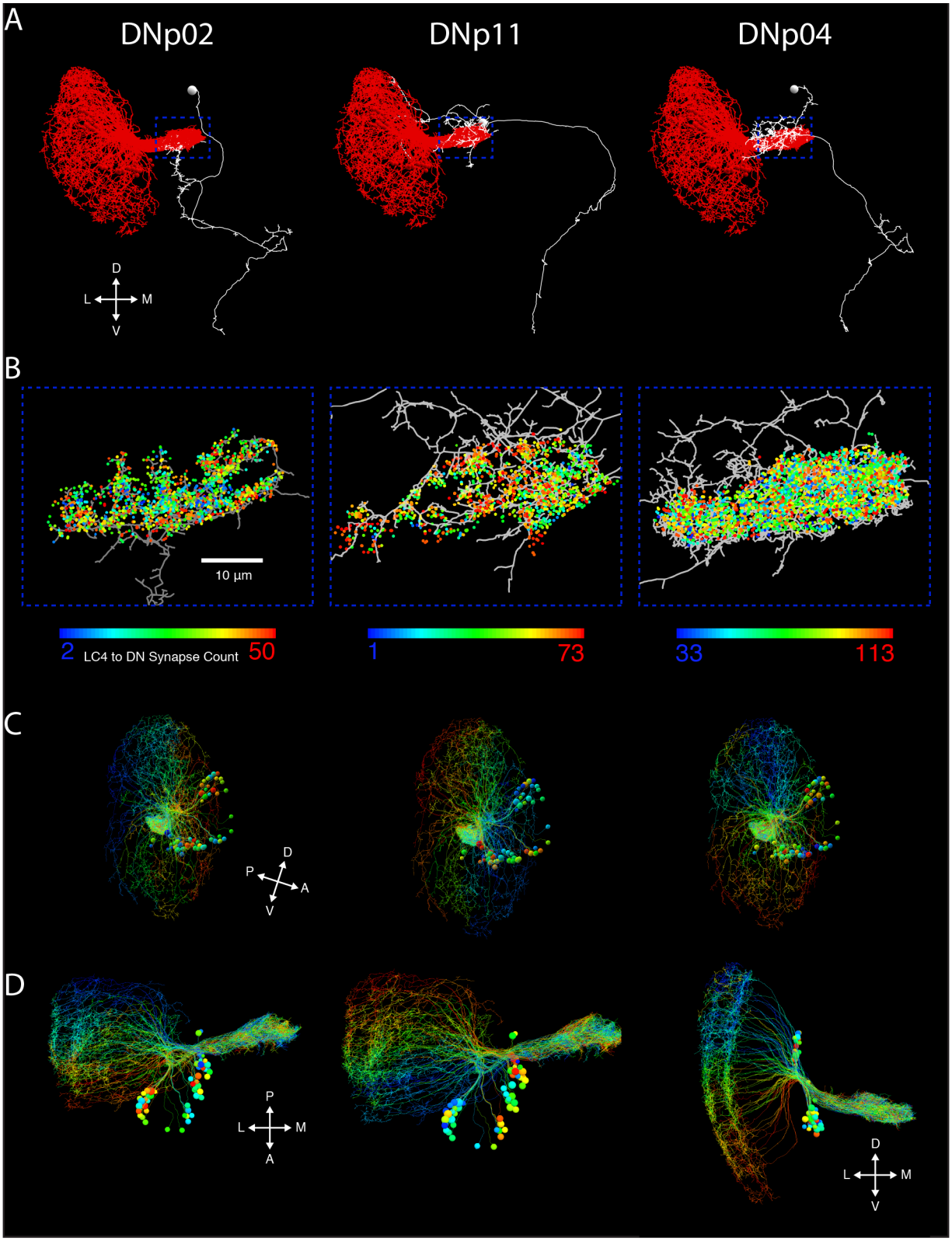

Figure 3.14: DNp02, DNp04 and DNp11 Connectivity With LC4 Neurons Reveals Visual Gradients in Synaptic Counts

Figure 3.14 ***(previous page)*****: DNp02, DNp04 and DNp11 Connectivity With LC4 Neurons Reveals Visual Gradients in Synaptic Counts**
(A) LC4DNs: DNp02, DNp11, DNp04 (white) and 55 LC4 neurite skeletons (red) traced in a fly brain EM volume [168]. Soma marked with a circle approximating the diameter.
(B)Annotated synapses from LC4 Neurons to DNp02 (1498), DNp04 (3479) and DNp11 (1363) at the LC4 optic glomerulus. LC4 presynaptic sites are overlaid onto the dendritic arbors for DNp02, DNp11 and DNp04. Synapse markers colored by the total number of synapses formed by a particular LC4 neuron.
(C) Individual LC4 neurons colored according to number of synapses, as in (B). Rotated into symmetric view of the lobula. Due to the off-axis orientation of the lobula axes presented here are approximate: D: dorsal, V: ventral, L: lateral, M: medial, A: anterior, P: posterior.
(D) Additional views of the synaptic gradients.

3.4 Discussion

3.4.1 Summary of results

In order to identify neural pathways underlying fly escape beyond the GF, we investigated a set of DNs related by their putatively shared input from LC4, a population of retinotopic, looming speed-encoding visual neurons. We hypothesized that these LC4DNs could control aspects of the escape behavior by carrying looming-encoding signals from LC4 to escape motor circuits in the lower tectulum of the VNC. Using DN-specific driver lines, we found evidence that four LC4DN types support distinct escape sub-behaviors, indicating that they form a functional group for escape control. Using the FlyPEZ, activation of DNp04 and DNp11 elicited long-mode escapes that are distinct from the known short-mode escapes generated by GF activation. Silencing of LC4DNs in looming-evoked escapes did not reveal complementary deficits in long-mode escape, perhaps due to the expected redundancy for generation of long-mode escape within the group. Closer examination of the activation phenotypes revealed that DNp02 and DNp11 shift the fly center of mass relative to the jumping legs and determine the direction of activation-driven escapes. To understand if this motor bias is linked to a sensory preference, we traced DNp02, DNp04 and DNp11 in an EM volume to assess LC4 connectivity. Each LC4 neuron forms different numbers of synapses with each DN depending on its position in visual space, resulting in distinct connectivity

gradients across the LC4 retinotopy for each DN.

3.4.2 Working model of looming-evoked escape

The LC4DN functional group can coordinate escape through the following sensorimotor processing model. First, a looming stimulus is detected by the visual system, and encoded in loom-detecting visual output neurons, including LC4. At the LC4 optic glomerulus, each LC4 neuron is pre-synaptic to multiple downstream LC4DNs. At lower looming expansion rates, few LC4DNs are recruited (such as DNp04), and at higher rates, more are co-active (including GF). In the case that the center of looming expansion originates in the anterior visual field, DNp02 is expected to receive more LC4 input; while DNp11 would receive more if the center originated in the posterior field. DNp02, DNp04, DNp06, DNp11, and GF axons all converge on the lower tectulum, where they can recruit motor circuits to drive local circuits regulating wing raising, leg extension and wing depression. DNp02 and DNp11 are expected to connect to circuits governing posture, which determines a backward or forward escape trajectory. For high looming expansion rates, when escape is urgent, GF activity could override ongoing recruitment by other LC4DNs to generate immediate takeoff [155]. Slower, less urgent stimuli would be more likely to drive postural adjustments and long-mode escapes.

3.4.3 Future LC4DN work

Although we investigated the LC4DNs using the FlyPEZ with available driver lines, our experiments were certainly not exhaustive. Critically, in our silencing experiments, we were unable to simultaneously target DNp04 and DNp11 to determine if long-mode escapes are reduced. Within the LC4DN functional group, we utilized high-quality driver lines, and future investigations will benefit from new technologies allowing more precise and combinatorial testing. A critical future experiment is the investigation of the spatial tuning properties afforded by the LC4 to LC4DN synaptic connectivity identified in the EM tracing

and annotations. To determine if these gradients have functional significance, physiology experiments measuring DN activity can be used to determine the spatial looming receptive field for DNp02, DNp04 and DNp11. From the identified synaptic connectivity gradients, we predict that DNp2 and DNp11 will show strongest looming responses from the anterior and posterior fields, respectively.

For LC4DNs we did not find activation phenotypes for, or couldn't make driver lines for, it is possible or even likely, that they (DNp03, DNp05, DNp35 and DNp40) are looming-sensitive and in some way contribute to escape and/or avoidance behaviors on land [56] or in flight [103]. As indicated by the EM data, the possibility of sensitivity to spatial location of the looming stimulus suggests new looming stimulus orientations to test in silencing behavioral experiments of DNp02 and DNp11. Furthermore, beyond the LC4DNs, a study by our colleagues, Zacharias et. al. [166], implicates DNp09 in the control of looming-evoked freezing behavior, indicating that descending control of the escape sequence extends to DNs outside of the LC4DN group. The looming sensitivity of DNp09 has not yet been investigated. In future experiments, ongoing development imaging techniques [26] that can monitor population neural activity and behavior could more efficiently and completely identify DN control of loom-evoked behavior.

3.5 Statistics Tables

Due to the large number of statistical comparisons in the FlyPEZ behavior experiments, we generated a set of tables for completeness and clarity. In each graph, we report the groups being compared, the test statistic, and the raw p-value in standard form. The p-value (Bonf.) indicates the application of the *post-hoc* Bonferroni correction for multiple comparisons. This is typically not reported as a change to a p-value, but as a change in the comparison value, α, that indicates significance level. It is not standard practice to do this because it is possible to get non-sensical p-values (greater than 1); however by applying the correction in to the p-value listed, we can determine significance intuitively by the standard

values (* for $p < 0.05$, ** $p < 0.01$, *** $p < 0.001$), so values are presented in this way here.

Table 3.1: Statistics for Figure 3.5

Normal Approximation to the Binomial Z-Test for Figure 3.5A

Group 1	Group 2	$N_{Group\ 1}$	$N_{Group\ 2}$	Z-Score	p-value	p-value (Bonf)	Significance Marker
Empty Split Control x CsChrimson	DL Wildtype x CsChrimson	514	618	2.00E+00	4.59E-02	9.17E-01	
Empty Split Control x CsChrimson	Giant Fiber (SS00727) x CsChrimson	514	232	2.53E+01	0.00E+00	0.00E+00	***
Empty Split Control x CsChrimson	Giant Fiber (SS27721) x CsChrimson	514	522	2.91E+01	0.00E+00	0.00E+00	***
Empty Split Control x CsChrimson	DNp02 (SS01053) x CsChrimson	514	236	6.35E-01	5.26E-01	1.05E+01	
Empty Split Control x CsChrimson	DNp02 (SS01554) x CsChrimson	514	230	1.19E+00	2.33E-01	4.65E+00	
Empty Split Control x CsChrimson	DNp03 (SS01081) x CsChrimson	514	193	5.37E-01	5.91E-01	1.18E+01	
Empty Split Control x CsChrimson	DNp03 (SS01596) x CsChrimson	514	210	1.80E+00	7.21E-02	1.44E+00	
Empty Split Control x CsChrimson	DNp04 (SS00934) x CsChrimson	514	224	4.61E+00	3.96E-06	7.91E-05	***
Empty Split Control x CsChrimson	DNp04 (SS01080) x CsChrimson	514	244	3.90E+00	9.57E-05	1.91E-03	**
Empty Split Control x CsChrimson	DNp05 (SS02612) x CsChrimson	514	266	5.61E-02	9.55E-01	1.91E+01	
Empty Split Control x CsChrimson	DNp05 (SS00865) x CsChrimson	514	252	7.06E-01	4.80E-01	9.60E+00	
Empty Split Control x CsChrimson	DNp06 (SS02256) x CsChrimson	514	249	1.02E+00	3.06E-01	6.12E+00	
Empty Split Control x CsChrimson	DNp11 (SS49010) x CsChrimson	514	264	9.17E+00	0.00E+00	0.00E+00	***
Empty Split Control x CsChrimson	DNp11 (SS49024) x CsChrimson	514	292	1.14E+01	0.00E+00	0.00E+00	***
Empty Split Control x CsChrimson	DNp11 (SS49051) x CsChrimson	514	294	3.37E+00	7.44E-04	1.49E-02	*
Empty Split Control x CsChrimson	DNa07 (SS01541) x CsChrimson	514	205	6.10E-01	5.42E-01	1.08E+01	
Empty Split Control x CsChrimson	DNa07 (SS01542) x CsChrimson	514	209	3.47E-01	7.28E-01	1.46E+01	
Empty Split Control x CsChrimson	DNa07 (SS01571) x CsChrimson	514	217	1.13E+00	2.57E-01	5.14E+00	
Empty Split Control x CsChrimson	DNp02, DNp04 (SS01554) x CsChrimson	514	208	1.25E+01	0.00E+00	0.00E+00	***
Empty Split Control x CsChrimson	DNp02, DNp04, DNp06 (SS02292) x CsChrimson	514	222	1.34E+01	0.00E+00	0.00E+00	***

Wilcoxon Rank Sum Test for Figure 3.5B

Group 1	Group 2	$N_{Group\ 1}$	$N_{Group\ 2}$	W-Score	p-value	p-value (Bonf)	Significance Marker
Giant Fiber x CsChrimson	DNp04 x CsChrimson	714	52	2.56E+05	1.14E-95	4.56E-95	***
Giant Fiber x CsChrimson	DNp11 x CsChrimson	714	185	2.57E+05	9.35E-29	3.74E-28	***
Giant Fiber x CsChrimson	DNp02, DNp04 x CsChrimson	714	80	2.65E+05	3.89E-22	1.56E-21	***
Giant Fiber x CsChrimson	DNp02, DNp04, DNp06 x CsChrimson	714	92	2.69E+05	3.62E-19	1.45E-18	***

Normal Approximation to the Binomial Z-Test for Figure 3.5C

Group 1	Group 2	$N_{Group\ 1}$	$N_{Group\ 2}$	Z-Score	p-value	p-value (Bonf)	Significance Marker
Giant Fiber x CsChrimson	DNp04 x CsChrimson	714	52	2.60E+01	0.00E+00	0.00E+00	***
Giant Fiber x CsChrimson	DNp11 x CsChrimson	714	185	1.88E+01	0.00E+00	0.00E+00	***
Giant Fiber x CsChrimson	DNp02, DNp04 x CsChrimson	714	80	1.79E+01	0.00E+00	0.00E+00	***
Giant Fiber x CsChrimson	DNp02, DNp04, DNp06 x CsChrimson	714	92	1.53E+01	0.00E+00	0.00E+00	***

Normal Approximation to the Binomial Z-Test for Figure 3.6A (L/V = 10)

Group 1	Group 2	$N_{Group\ 1}$	$N_{Group\ 2}$	Z-Score	p-value	p-value (Bonf)	Significance Marker
Empty Split Control x KIR	DL Wildtype x KIR	133	232	9.50E-01	3.42E-01	7.19E+00	
Empty Split Control x KIR	Giant Fiber (SS00727) x KIR	133	138	2.98E-01	7.66E-01	1.61E+01	
Empty Split Control x KIR	Giant Fiber (SS27721) x KIR	133	99	9.42E-01	3.46E-01	7.27E+00	
Empty Split Control x KIR	L1, L2 (SS00797) x KIR	133	139	3.57E+00	3.59E-04	7.53E-03	**
Empty Split Control x KIR	DNa07 (SS01541) x KIR	133	132	1.12E+00	2.62E-01	5.51E+00	
Empty Split Control x KIR	DNa07 (SS01542) x KIR	133	120	1.35E+00	1.76E-01	3.69E+00	
Empty Split Control x KIR	DNa07 (SS01571) x KIR	133	124	8.21E-01	4.12E-01	8.64E+00	
Empty Split Control x KIR	DNp02 (SS01053) x KIR	133	115	1.69E+00	9.18E-02	1.93E+00	
Empty Split Control x KIR	DNp02 (SS01554) x KIR	133	87	1.59E-01	8.73E-01	1.83E+01	
Empty Split Control x KIR	DNp03 (SS01081) x KIR	133	139	2.53E+00	1.15E-02	2.42E-01	
Empty Split Control x KIR	DNp03 (SS01596) x KIR	133	110	1.05E+00	2.96E-01	6.21E+00	
Empty Split Control x KIR	DNp04 (SS00934) x KIR	133	182	4.91E-01	6.24E-01	1.31E+01	
Empty Split Control x KIR	DNp04 (SS01080) x KIR	133	121	3.64E-01	7.16E-01	1.50E+01	
Empty Split Control x KIR	DNp05 (SS02612) x KIR	133	93	5.45E-01	5.86E-01	1.23E+01	
Empty Split Control x KIR	DNp05 (SS00865) x KIR	133	109	1.08E+00	2.80E-01	5.88E+00	
Empty Split Control x KIR	DNp06 (SS02256) x KIR	133	136	1.31E+00	1.89E-01	3.98E+00	
Empty Split Control x KIR	DNp11 (SS49010) x KIR	133	106	6.54E-01	5.13E-01	1.08E+01	
Empty Split Control x KIR	DNp11 (SS49024) x KIR	133	124	6.19E-01	5.36E-01	1.13E+01	
Empty Split Control x KIR	DNp11 (SS49051) x KIR	133	116	6.72E-01	5.01E-01	1.05E+01	
Empty Split Control x KIR	DNp02, DNp04 (SS01554) x KIR	133	133	1.05E+00	2.93E-01	6.16E+00	
Empty Split Control x KIR	DNp02, DNp04, DNp06 (SS02292) x KIR	133	250	4.88E-01	6.26E-01	1.31E+01	

Normal Approximation to the Binomial Z-Test for Figure 3.6B (L/V = 20)

Group 1	Group 2	$N_{Group\ 1}$	$N_{Group\ 2}$	Z-Score	p-value	p-value (Bonf)	Significance Marker
Empty Split Control x KIR	DL Wildtype x KIR	111	263	1.00E-02	9.92E-01	2.08E+01	
Empty Split Control x KIR	Giant Fiber (SS00727) x KIR	111	132	2.01E+00	4.40E-02	9.24E-01	
Empty Split Control x KIR	Giant Fiber (SS27721) x KIR	111	103	5.76E-01	5.65E-01	1.19E+01	
Empty Split Control x KIR	L1, L2 (SS00797) x KIR	111	164	7.19E+00	6.35E-13	1.33E-11	***
Empty Split Control x KIR	DNa07 (SS01541) x KIR	111	152	1.60E+00	1.09E-01	2.28E+00	
Empty Split Control x KIR	DNa07 (SS01542) x KIR	111	138	3.18E-03	9.97E-01	2.09E+01	
Empty Split Control x KIR	DNa07 (SS01571) x KIR	111	161	1.45E+00	1.46E-01	3.07E+00	
Empty Split Control x KIR	DNp02 (SS01053) x KIR	111	120	2.11E+00	3.49E-02	7.32E-01	
Empty Split Control x KIR	DNp02 (SS01554) x KIR	111	132	1.35E+00	1.77E-01	3.71E+00	
Empty Split Control x KIR	DNp03 (SS01081) x KIR	111	98	1.22E-01	9.03E-01	1.90E+01	
Empty Split Control x KIR	DNp03 (SS01596) x KIR	111	111	1.14E+00	2.55E-01	5.35E+00	
Empty Split Control x KIR	DNp04 (SS00934) x KIR	111	118	2.48E+00	1.32E-02	2.78E-01	
Empty Split Control x KIR	DNp04 (SS01080) x KIR	111	93	1.36E+00	1.74E-01	3.65E+00	
Empty Split Control x KIR	DNp05 (SS02612) x KIR	111	86	2.98E-01	7.66E-01	1.61E+01	
Empty Split Control x KIR	DNp05 (SS00865) x KIR	111	106	9.02E-01	3.67E-01	7.71E+00	
Empty Split Control x KIR	DNp06 (SS02256) x KIR	111	166	2.07E+00	3.83E-02	8.04E-01	
Empty Split Control x KIR	DNp11 (SS49010) x KIR	111	112	1.44E+00	1.51E-01	3.16E+00	
Empty Split Control x KIR	DNp11 (SS49024) x KIR	111	117	1.04E+00	2.98E-01	6.27E+00	
Empty Split Control x KIR	DNp11 (SS49051) x KIR	111	111	4.14E-01	6.79E-01	1.43E+01	
Empty Split Control x KIR	DNp02, DNp04 (SS01554) x KIR	111	127	3.12E+00	1.83E-03	3.85E-02	*
Empty Split Control x KIR	DNp02, DNp04, DNp06 (SS02292) x KIR	111	256	2.83E+00	4.64E-03	9.74E-02	

Table 3.2: Statistics for Figure 3.6 (Page 1/2)

Normal Approximation to the Binomial Z-Test for Figure 3.6C (L/V = 40)

Group 1	Group 2	$N_{Group\ 1}$	$N_{Group\ 2}$	Z-Score	p-value	p-value (Bonf)	Significance Marker
Empty Split Control x KIR	DL Wildtype x KIR	143	219	2.21E-01	8.25E-01	1.73E+01	
Empty Split Control x KIR	Giant Fiber (SS00727) x KIR	143	118	6.01E-01	5.48E-01	1.15E+01	
Empty Split Control x KIR	Giant Fiber (SS27721) x KIR	143	96	1.67E-01	8.67E-01	1.82E+01	
Empty Split Control x KIR	L1, L2 (SS00797) x KIR	143	105	6.47E+00	9.57E-11	2.01E-09	***
Empty Split Control x KIR	DNa07 (SS01541) x KIR	143	151	1.88E+00	5.96E-02	1.25E+00	
Empty Split Control x KIR	DNa07 (SS01542) x KIR	143	133	6.61E-01	5.08E-01	1.07E+01	
Empty Split Control x KIR	DNa07 (SS01571) x KIR	143	110	3.00E-01	7.64E-01	1.60E+01	
Empty Split Control x KIR	DNp02 (SS01053) x KIR	143	97	1.02E+00	3.08E-01	6.46E+00	
Empty Split Control x KIR	DNp02 (SS01554) x KIR	143	140	2.60E+00	9.21E-03	1.93E-01	
Empty Split Control x KIR	DNp03 (SS01081) x KIR	143	70	3.16E+00	1.57E-03	3.30E-02	
Empty Split Control x KIR	DNp03 (SS01596) x KIR	143	150	5.78E-01	5.63E-01	1.18E+01	
Empty Split Control x KIR	DNp04 (SS00934) x KIR	143	121	1.39E+00	1.64E-01	3.44E+00	
Empty Split Control x KIR	DNp04 (SS01080) x KIR	143	88	7.53E-01	4.52E-01	9.48E+00	
Empty Split Control x KIR	DNp05 (SS02612) x KIR	143	91	1.83E+00	6.78E-02	1.42E+00	
Empty Split Control x KIR	DNp05 (SS00865) x KIR	143	106	1.09E+00	2.78E-01	5.83E+00	
Empty Split Control x KIR	DNp06 (SS02256) x KIR	143	113	1.62E+00	1.05E-01	2.21E+00	
Empty Split Control x KIR	DNp11 (SS49010) x KIR	143	103	6.01E-01	5.48E-01	1.15E+01	
Empty Split Control x KIR	DNp11 (SS49024) x KIR	143	105	1.07E+00	2.83E-01	5.95E+00	
Empty Split Control x KIR	DNp11 (SS49051) x KIR	143	131	1.66E+00	9.73E-02	2.04E+00	
Empty Split Control x KIR	DNp02, DNp04 (SS01554) x KIR	143	68	8.14E-01	4.16E-01	8.73E+00	
Empty Split Control x KIR	DNp02, DNp04, DNp06 (SS02292) x KIR	143	228	1.03E+00	3.02E-01	6.35E+00	

Normal Approximation to the Binomial Z-Test for Figure 3.6D (L/V = 80)

Group 1	Group 2	$N_{Group\ 1}$	$N_{Group\ 2}$	Z-Score	p-value	p-value (Bonf)	Significance Marker
Empty Split Control x KIR	DL Wildtype x KIR	123	163	2.38E+00	1.74E-02	3.65E-01	
Empty Split Control x KIR	Giant Fiber (SS00727) x KIR	123	97	2.10E-01	8.34E-01	1.75E+01	
Empty Split Control x KIR	Giant Fiber (SS27721) x KIR	123	102	4.98E-01	6.19E-01	1.30E+01	
Empty Split Control x KIR	L1, L2 (SS00797) x KIR	123	82	4.70E+00	2.61E-06	5.49E-05	***
Empty Split Control x KIR	DNa07 (SS01541) x KIR	123	126	2.09E+00	3.69E-02	7.75E-01	
Empty Split Control x KIR	DNa07 (SS01542) x KIR	123	114	2.57E+00	1.01E-02	2.13E-01	
Empty Split Control x KIR	DNa07 (SS01571) x KIR	123	137	1.97E+00	4.91E-02	1.03E+00	
Empty Split Control x KIR	DNp02 (SS01053) x KIR	123	111	1.01E+00	3.10E-01	6.52E+00	
Empty Split Control x KIR	DNp02 (SS01554) x KIR	123	110	1.50E+00	1.34E-01	2.82E+00	
Empty Split Control x KIR	DNp03 (SS01081) x KIR	123	101	2.63E+00	8.43E-03	1.77E-01	
Empty Split Control x KIR	DNp03 (SS01596) x KIR	123	108	9.43E-01	3.46E-01	7.26E+00	
Empty Split Control x KIR	DNp04 (SS00934) x KIR	123	114	5.44E-01	5.86E-01	1.23E+01	
Empty Split Control x KIR	DNp04 (SS01080) x KIR	123	102	1.23E+00	2.19E-01	4.60E+00	
Empty Split Control x KIR	DNp05 (SS02612) x KIR	123	90	6.03E-01	5.46E-01	1.15E+01	
Empty Split Control x KIR	DNp05 (SS00865) x KIR	123	90	1.56E+00	1.18E-01	2.48E+00	
Empty Split Control x KIR	DNp06 (SS02256) x KIR	123	112	4.00E-01	6.89E-01	1.45E+01	
Empty Split Control x KIR	DNp11 (SS49010) x KIR	123	91	1.48E+00	1.39E-01	2.92E+00	
Empty Split Control x KIR	DNp11 (SS49024) x KIR	123	97	2.01E+00	4.40E-02	9.24E-01	
Empty Split Control x KIR	DNp11 (SS49051) x KIR	123	86	2.08E+00	3.79E-02	7.96E-01	
Empty Split Control x KIR	DNp02, DNp04 (SS01554) x KIR	123	122	1.34E+00	1.80E-01	3.78E+00	
Empty Split Control x KIR	DNp02, DNp04, DNp06 (SS02292) x KIR	123	189	1.46E+00	1.44E-01	3.02E+00	

Table 3.2 ***(previous page)*****: Statistics for Figure 3.6 (Page 2/2)**

Wilcoxon Rank Sum Test for Figure 3.7A

Group 1 (Escape Duration)	Group 2 (Escape Duration)	$N_{Group\ 1}$	$N_{Group\ 2}$	W-Score	p-value	p-value (Bonf)	Significance Marker
DL Wildtype x KIR	SS1062	100	97	1.03E+04	6.50E-02	6.50E-01	
DL Wildtype x KIR	Giant Fiber x KIR	100	100	1.20E+04	2.72E-06	2.72E-05	***
DL Wildtype x KIR	DNp02 x KIR	100	100	1.05E+04	3.14E-01	3.14E+00	
DL Wildtype x KIR	DNp03 x KIR	100	100	9.03E+03	1.24E-02	1.24E-01	
DL Wildtype x KIR	DNp04 x KIR	100	100	1.05E+04	2.30E-01	2.30E+00	
DL Wildtype x KIR	DNp05 x KIR	100	99	9.64E+03	5.16E-01	5.16E+00	
DL Wildtype x KIR	DNp06 x KIR	100	90	8.23E+03	3.35E-01	3.35E+00	
DL Wildtype x KIR	DNp11 x KIR	100	63	6.48E+03	2.48E-01	2.48E+00	
DL Wildtype x KIR	DNp02, DNp04 x KIR	100	90	5.44E+03	1.87E-01	1.87E+00	
DL Wildtype x KIR	DNp02, DNp04, DNp06 x KIR	100	57	8.91E+03	4.01E-01	4.01E+00	

Normal Approximation to the Binomial Z-Test for Figure 3.7B

Group 1 (Escape Duration)	Group 2 (Escape Duration)	$N_{Group\ 1}$	$N_{Group\ 2}$	Z-Score	p-value	p-value (Bonf)	Significance Marker
DL Wildtype x KIR	SS1062	100	97	1.45E-01	8.85E-01	8.85E+00	
DL Wildtype x KIR	Giant Fiber x KIR	100	100	4.55E+00	5.30E-06	5.30E-05	***
DL Wildtype x KIR	DNp02 x KIR	100	100	6.23E-01	5.33E-01	5.33E+00	
DL Wildtype x KIR	DNp03 x KIR	100	100	2.74E+00	6.20E-03	6.20E-02	
DL Wildtype x KIR	DNp04 x KIR	100	100	3.09E-01	7.58E-01	7.58E+00	
DL Wildtype x KIR	DNp05 x KIR	100	99	1.09E+00	2.74E-01	2.74E+00	
DL Wildtype x KIR	DNp06 x KIR	100	90	1.14E+00	2.54E-01	2.54E+00	
DL Wildtype x KIR	DNp11 x KIR	100	63	9.93E-01	3.21E-01	3.21E+00	
DL Wildtype x KIR	DNp02, DNp04 x KIR	100	90	5.06E-01	6.13E-01	6.13E+00	
DL Wildtype x KIR	DNp02, DNp04, DNp06 x KIR	100	57	1.83E+00	6.71E-02	6.71E-01	

Table 3.3: Statistics for Figure 3.7

Line Designation	Expression	Genotype	Reference
Empty Brain Control	None	R24A03_p65ADZp (attP40); R74C01_ZpGdbd (attP2)	Namiki et. al. 2018
DL Wildtype	-	-	Wild-type line from M. H. Dickinson, Caltech
SS00797	L1,L2 (Lamina)	R48H08_p65ADZp (attP40); R29G11_ZpGdbd (attP2)	Tuthill et. al. 2013
SS00727	Giant Fiber (DNp01)	R14A01_p65ADZp (attP40); R79H12_ZpGdbd (attP2)	Namiki et. al. 2018
SS27721	Giant Fiber (DNp01)	R17A04_p65ADZp (attP40); R68A06_ZpGdbd (attP2)	Von Reyn et. al. 2014
SS01053	DNp02	VT063736_p65ADZp (attP40); R24A03_ZpGdbd (attP2)	Namiki et. al. 2018
SS01554	DNp02	VT063736_p65ADZp (attP40); VT017647_ZpGdbd (attP2)	Namiki et. al. 2018
SS01081	DNp03	R91C05_p65ADZp (attP40); R31B08_ZpGdbd (attP2)	Namiki et. al. 2018
SS01596	DNp03	R29F12_p65ADZp (attP40); R37G07_ZpGdbd (attP2)	Namiki et. al. 2018
SS01080	DNp04	R84B12_p65ADZp (attP40); VT048835_ZpGdbd (attP2)	Namiki et. al. 2018
SS00934	DNp04	VT032898_p65ADZp (attP40); VT048835_ZpGdbd (attP2)	Namiki et. al. 2018
SS02612	DNp05	VT047755_p65ADZp (attP40); VT003280_ZpGdbd (attP2)	Namiki et. al. 2018
SS00865	DNp05	VT019060_p65ADZp (attP40); VT003280_ZpGdbd (attP2)	Namiki et. al. 2018
SS02256	DNp06	VT019018_p65ADZp (attP40); VT017411_ZpGdbd (attP2)	Namiki et. al. 2018
SS49010	DNp11	BJD110D01_p65ADZp (attP40); R18G08_ZpGdbd (attP2)	Namiki et. al. 2018
SS49024	DNp11	BJD119F04_p65ADZp (attP40); R18G08_ZpGdbd (attP2)	Namiki et. al. 2018
SS49051	DNp11	R18G08_p65ADZp (attP40); BJD100H09_ZpGdbd (attP2)	Namiki et. al. 2018
SS01541	DNa07	VT028606_p65ADZp (attP40); R56G08_ZpGdbd (attP2)	Namiki et. al. 2018
SS01542	DNa07	VT028606_p65ADZp (attP40); R87B09_ZpGdbd (attP2)	Namiki et. al. 2018
SS01571	DNa07	VT028606_p65ADZp (attP40); VT008675_ZpGdbd (attP2)	Namiki et. al. 2018
SS01544	DNp02, DNp04	VT048835_p65ADZp (attP40); VT017647_ZpGdbd (attP2)	Namiki et. al. 2018
SS02292	DNp02, DNp04, DNp06	VT017411_p65ADZp (attP40); VT017647_ZpGdbd (attP2)	Namiki et. al. 2018

Table 3.4: Fly Driver Lines

3.6 Materials and Methods

3.6.1 Fly stocks

We prepared flies following identical procedures described in Chapter 2 for optogenetic activation and neuronal inactivation experiments on the FlyPEZ. The driver lines used in this study are contained in Table 3.4. Access to a subset of the LC4DN driver lines and imagery is available at the FlyLight project website (http://splitgal4.janelia.org/cgi-bin/splitgal4.cgi).

For electrophysiology experiments, driver lines for DNp02 (SS01053), DNp04 (SS0934) and DNp06 (SS02256) were crossed to a reporter construct, pJFRC28-10XUAS-IVS-GFP-p10 (attP2) [117], to express cytosolic GFP in order to visually target patch electrodes to the cell body.

3.6.2 FlyPEZ activation and silencing experiments

Acquisition of video data using the FlyPEZ was performed in the same procedure described in the Materials and Methods section of Chapter 2. For both activation with CsChrimson [81] and Kir2.1 [116] silencing of LC4DNs and controls, an identical protocol was followed in preparing and testing flies. As described earlier, data was processed using the automated tracking and manual annotation GUI.

Analysis for Figure 3.12 was performed by building a custom MATLAB (The Mathworks, Inc., Natick, MA, USA) GUI for selecting the tips of middle leg tarsi. We utilized the ventral view from the 6000 frames-per-second FlyPEZ videos. The videos are subsampled at 200 Hz (5 ms intervals), which was sufficient to observe smooth changes in leg and body movements. Video data were analyzed if, in the 50 ms before the onset of the light stimulus, flies moved less than 0.25 mm and rotated less than 20° in azimuth. At the start of the stimulus, the fly center of mass was required to be within a 3 mm centered square boundary of the 5 mm square platform in order to ensure that all six legs were visible on the platform. This avoids potential biases from interactions between the fly and the edge of the filming platform. Videos in which visibility of legs was lost over the 100 ms of annotation were also excluded, except for cases where the fly performed a takeoff.

3.6.3 Electrophysiology

In vivo whole-cell patch clamp experiments were performed on tethered flies in a manner similar to [94, 155]. Female flies were anesthetized on a peltier-driven cold plate and positioned ventral side up to be tethered on a custom polyether ether ketone (PEEK) plate.

Flies were mounted with UV-cure glue. For recording stability, the proboscis was glued in a retracted position and the front pair of legs were clipped and glued at the femur. A window was cut in the cuticle on the posterior side of the head and the overlying fat was removed in order to access the DN soma. The brain was perfused with standard extracellular saline [58] containing: 103 mM NaCl, 3 mM KCl, 5mM *N*-Tris (hydroxymethyl)methyl-2-aminoethane-sulfonic acid, 8 mM trehalose, 10 mM glucose, 26 mM $NaHCO_3$, 1 mM NaH_2PO_4, 1.5 mM $CaCl_2$ and 4 mM $MgCl_2$ (osmolarity adjusted to 270-275 mOsm), bubbled with 95% O_2/5% CO_2 and adjusted to pH 7.3 at 21-23° C. The cell body for each LC4DN was targeted by its GFP expression. Collagenase (0.25% in extracellular saline, Collagenase from *Clostridium histolyticum*, Sigma-Aldrich Corp.) was applied gently with a large-bore pipette to the surface of the brain to break the perineural sheath locally above the position of the targeted soma. A small amount of tissue was then removed to gain unrestricted pipette access. Somata were visualized for patch recording with a 40x objective (UPLFLN, Olympus) and illuminated with an IR LED (OD-880F Opto Diode Corp.). Patch electrodes (5.5-7.5 MΩ) were backfilled with intracellular saline [58] containing: 140 mM potassium aspartate, 10 mM HEPES, 1 mM EGTA, 4 mM MgATP, 0.5 mM Na_3GTP, 1 mM KCl (osmolarity adjusted to 260-275, pH 7.3) and Alexa-568-hydazide-Na (10 μM, Invitrogen). The dye and the cytosolic GFP indicated that the target DN was patched. Signals were amplified and recorded with a MultiClamp 700B amplifier and a Digidata 1440A analog-to-digital converter (Molecular Devices). Recordings were sampled at 40khz and low-pass filtered to 10 khz. Recordings were performed in current clamp, with no applied holding current. Traces in figures are not corrected for liquid junction potential (13 mV) [58]. Patch recordings were performed if the initial seal was 4-8 GΩ, and the resting potential was less than -50 mV. Visual stimuli were presented by projection onto a 4-inch diameter dome. The projector and dome was prepared for back projection in the same method as the FlyPEZ GlobeDisplay. Custom visual stimuli were produced in Matlab to display looming stimuli of different l/v values in randomized sets. Looming stimuli were black on a white background, and programmed to expand from

5° to 90° following the expansion rate modeling constant velocity approach (see Introduction). Stimuli were displayed with a 5 second inter-stimulus interval. Presentation of stimuli was controlled by the Psychophysics Toolbox [16, 115, 83]. Recordings were analyzed only if the spiking responses were maintained throughout the visual stimulus presentation set (approximately 40 minutes). Stimulus frames were synchronized by simultaneously recording a photodiode with the recording trace and alternating light-dark patch on it, outside of the dome. During the recordings, flies did not have tarsal contact and did not initiate flight. Flight status was measured using a custom optical analyzer tool for measuring the fly's wingbeat frequency [94].

3.6.4 Electron microscopy

We annotated the FAFB transmission electron microscopy dataset [168] using the CATMAID [123] software suite to determine the chemical synaptic connectivity between the LC4 visual output neurons and three descending neurons of interest, DNp02, DNp04 and DNp11. As a starting point, we utilized previously-traced skeletons for LC4 and LPLC2 from a separate ongoing study. To start tracing the DNs, we used morphological cues from confocal fluorescence imaging [106] in distinct strategies to locate a starting point for tracing each descending neuron. For DNp02, confocal microscopy stacks suggested that the somata neurite travels close to the path of the GF somata neurite. We found DNp02 by locating its neurite within a shared soma tract, which, along with several other neurites, appears encased in a dark sheath. DNp04 was located when tracing the LC4 neurons. The skeleton was then traced out and linked to the same soma tract as DNp02 and GF. DNp11 was located by searching for candidate descending neurons which cross the midline dorsal of the esophagus. From each starting node, the full skeleton was traced and compared to the confocal image stacks for confirmation of cell type identity.

To determine the chemical synaptic connectivity, we searched for four criteria: T-bars and presynaptic vesicles, synaptic clefts, and post-syanptic densities. If a potential synapse

possessed two out of four criteria, it was labeled as a synapse. We focused our efforts on LC4 (presynaptic) and DNp02/DNp04/DNp11 (postsynaptic) synapses to gain a representative view of the connectivity between LC4 and the DNs.

3.7 Contributions and Acknowledgements

Work on the this project was performed by myself (M.Y.P.), Shigehiro Namiki (S.N.), Patrick Breads (P.B.), W. Ryan Williamson (W.R.W), Jason Polsky (J.P.), Shada Alghailani (S.A.), Emily Tenshaw (E.T.), Ruchi Parekh (R.P.), Grace Zhiyu Zheng (G.Z.Z.) and Gwyneth M. Card (G.M.C.).

S.N. identified and analyzed the anatomical characteristics of the LC4-cluster descending neurons and constructed the split-GAL4 lines in conjunction with the Descending Interneuron Team Project and the FlyLight Project, both at Janelia Research Campus. M.Y.P. performed the whole-cell patch clamp recordings and analysis. M.Y.P., P.B., W.R.W., G.Z.Z. carried out the FlyPEZ behavior experiments and analysis. J.P., S.A., E.T., R.P., and M.Y.P. carried out the neuronal tracing, synaptic labeling and connectivity analysis.

I worked in collaboration with my lab mate, S.N., to find and characterize novel descending neurons (DNs) likely related to the escape behavior. In his own project, S.N. anatomically described a large number of distinct descending neuron cell types in *Drosophila melanogaster*[106]. A subset of this work identifies and anatomically characterizes the LC4DNs. For clarity, a summary and adaptation of relevant work is presented here as introductory material, with permission.

For the FlyPEZ behavioral experiments, I designed the experiments based on split-GAL4 lines generated by S.N. G.Z.Z. and I prepared the flies, and P.B. and I ran the experiments on the FlyPEZ. P.B., W.R.W. and I worked on the behavioral analysis and data visualization.

The whole-cell patch clamp experiments were carried out and analyzed by myself. I had technical assistance and training from Catherine von Reyn, Jan Ache, Eyal Gruntman and Gwyneth Card.

For the anatomical analysis in the electron microscopy volume, I worked with the Janelia Connectome Annotation Group. J.P., S.A. and E.T. traced the morphology of the LC4 and descending neurons using the CATMAID [123] software suite. They also marked the synapses between LC4 and the descending neurons. J.P. generated the synaptic gradient visualizations. The team was coordinated by R.P.. I organized the project scope and goals.

In addition to my collaborators, I would like to thank Catherine Von Reyn, Jan Ache, Nathan Klapoetke, Vivek Jayaraman, Melina Hale, Daniel Margoliash, Ulrike Heberlein and Gwyneth Card for guidance and helpful discussions during this project.

CHAPTER 4

CONCLUDING REMARKS

In this thesis, I investigated the role of descending neurons in the control of visually-evoked escape behavior of fruit flies. I characterized how the control of particular sub-behaviors of the escape sequence are distributed across distinct descending neuron cell types. In chapter 2, I described the development of the FlyPEZ, a new assay for detailed and efficient characterization of fly behavior. I employed the FlyPEZ in chapter 3, along with other experiments, to investigate the LC4DNs, a group of descending neurons of which a subset are implicated in the control of escape. In this chapter, I will give a few personal perspectives on this work, discuss its significance in a broader context and speculate about ideas for future studies.

4.1 Considerations on Behavioral Side Effects from the FlyPEZ

The FlyPEZ automatically runs behavioral experiments with its three modules: FlyGate, FlyDetect and FlyGlobe. In the initial development of the FlyPEZ, I worked on the mechanism of the FlyGate, which automatically isolates individual flies as they walk up a small tunnel. By separating flies in this way, my colleagues and I have wondered whether flies are injured or are put into an alert or defensive state. These are important concerns because behavioral responses to stimuli are recorded within seconds of being isolated, and the effects of gating could influence the recorded behavior.

Determining whether the fly's state is altered by the FlyPEZ is difficult to assess. We have established that the visually-evoked escape behavior observed in the FlyPEZ matches previously described experiments [23] that did not use a gating system. The performance of the gating mechanism determines the degree to which the fly's state is affected. At the start of the project, I iterated FlyGate designs weekly using 3-D printed plastic with the goal of reducing both the number of flies that are pinned or crushed by the gate and the number of instances that two flies are released at the same time. Crushing a fly blocks the channel,

which stops the experiment until an operator clears it. In this failure mode, the experiment is no longer automated. Releasing multiple flies is easily handled by the FlyDetect algorithm, but reduces experimental efficiency. We successfully minimized pinning and crushing by tuning the micro-controller algorithm with specific empirically-determined thresholds and by using a micro servo with a crank rocker to precisely control the movement of the gate.

The most comparable method for moving flies for a behavioral assay is aspiration, where flies are sucked into a small chamber, typically by breathing in, and then blown out into a behavioral chamber (for example, see [122]). Other methods anesthetize flies by chill coma or carbon dioxide, which allows finer manipulation and individual mounting. The fly literature indicates that each method can deliver consistent results in behavioral experiments; however, there is evidence that any kind of handling strongly affects behavior, as assessed by Trannoy et al. [149]. In their aggression assay, handling affected the memory formed from losing bouts, and introduction of flies by negative geotaxis, similar to the FlyPEZ but without the gate, was deemed the best solution. A practical answer to assess the effect of the FlyGate on the fly's alertness may be finding a difference between a set of singly housed and released, or grouped and then gated out flies in the looming escape paradigm to test their tendency to escape. I would expect the flies to escape at a higher rate if the interaction with the gate raises their alertness. Investigating these effects may be the most purposeful if the FlyGate is adapted to assay other, sensitive behaviors, like aggression.

4.2 Feed-forward Generation of Escape Behavior by Descending Neurons

A simple model of feed-forward descending control of the the fly escape a system involves distinct DN cell types triggering each sub-behavior of the escape sequence. For freezing, postural adjustment, wing raising, and takeoff (wing depression and middle leg extension) [23], the activity in a particular LC4DN cell type generates each distinct action, in a feed-

forward manner. This model is plausible because we found that the GF activity drives takeoff [155], so perhaps the other sub-behaviors could be controlled in a similar fashion.

Using the FlyPEZ to perform optogenetic activation experiments with the LC4DN driver lines, we predicted that distinct DNs can generate particular escape sub-behaviors. We found that activation of DNp04 and DNp11 generated long-mode escapes, indicating that they can drive both wing raising and takeoff. The timing between wing raising and takeoff varied widely. These observations are surprising because they suggest a downstream mechanism that can perform both actions separated by a variable amount of time. One possibility is that initial activity from the DNs activates a wing raising circuit, and if the DN activity passes a threshold, a takeoff is generated by a separate DN-coupled circuit.

In contrast to finding LC4DN cell types that can generate one or multiple escape sub-behaviors, a study in the locust found evidence for multiplexing escape sub-behaviors in a single DN, the DCMD (descending contralateral movement detector) [48]. Locust escape is composed a preparatory cocontraction of antagonistic leg muscles and a jump. Fotowat et al. showed that cocontraction begins at a DCMD firing rate threshold and the jump timing matches peak firing rate. Whether the locust jumps or not depends on the total spike count. The current model for descending control involves activity of a pair of DNs: the DCMD and a nearly identical ipsilateral DN. Perhaps some multiplexing properties of the DCMD are present in circuits for LC4DNs that can generate multiple sub-behaviors. Initiation, and threshold properties could be substantiated if DN activity could be precisely monitored with motor activity.

Activation of DNp02 and DNp11 generated postural shifts that lead to directional escape. These postural shifts aren't exactly like those observed in response to looming stimuli. When evoked by activation, shifts move the fly center of mass regardless of initial position. When visually-evoked, repositioning of the legs only occurs when the position needs to be changed. This observation is the basis for describing the leg repositioning as motor planning [23]. The behavior is likely to have a reading of current postural state, and this seems to not be

engaged or is overridden by the activation. There may exist proprioceptive feedback control to these DNs through ascending neurons to engage shifting only when appropriate. While the activated shifting was effective in determining escape direction, leg repositioning was never observed. Perhaps group co-activity in DNs is important in naturalistic shifting and leg repositioning. The phenotype for DNp06, which is looming sensitive, involved raising a variable number of legs. The fly may lose its balance and hit the filming platform. This was difficult to quantify in FlyPEZ videos, but may be a clue into different motor components coordinated by DN signaling.

To contextualize our LC4DN silencing results, we can consider previous work on the LC4 visual output neurons and the GF. When LC4 is activated, flies generate a short-mode escape similar to GF activation. When LC4 is silenced, looming-evoked short-mode escapes are reduced nearly to the extent of GF-silenced flies [156]. These results are consistent with idea that LC4 activation drives a spike in GF to produce short-mode escapes, interrupting any wing-raising expected of downstream DNp04 and DNp11 long-mode escapes. Evidence and modeling for a GF override property has been explored in previous work [155]. Silencing of LC4 also reduces loom-evoked escape rates at high looming expansion rates (l/v = 10, 20, 40 ms) to a greater degree than GF silencing [156]. This suggests that LC4 silencing decreases overall escape drive by reducing visual drive to all LC4DN escape pathways. We can relate this to our observation that activation of multi LC4DN lines produced higher escape rates than would be expected from a summation of escape rates of individually activated LC4DNs. Together, these findings suggest a convergence in downstream motor circuits where drive from LC4DNs is integrated. We did not observe consistent differences in escape rates from control at the same looming expansion rates tested in the LC4 experiments. The two multi LC4DN lines did not show reductions either; however, we were unable to develop a driver line with both DNp04 and DNp11, the two LC4DNs which can individually drive long-mode escape. Considering that GF can generate some long-mode looming-evoked escape due to its override property [155], we would expect elimination of long-mode only if there are

no other wing-raising pathways. To resolve this question and investigate the possibility of pooled drive to downstream circuits, future experiments could investigate methods that allow improved selectivity and flexibility in the control expression in groups of distinct but functionally-related cell types.

4.3 Mechanisms for Generating the Escape Sequence

Differential tuning in DNs to expansion properties of the looming stimulus could set the order of the escape sequence. The freezing DN would have sensitivity to a small, slowly-expanding start of the looming stimulus, while the takeoff would be most sensitive to the large, quickly-expanding end of the looming stimulus. Peak activity in the DNs as the looming stimulus proceeds would piece together the escape sequence. Peak activity at a looming stimulus size (η response) has been observed in the GF and in loom-encoding neurons in many escape systems. This response profile is computed through the combination of excitatory and inhibitory visual inputs [114], and so a group of DNs with slightly different looming stimulus size tuning seems a plausible mechanism for ordering the sub-behaviors of the escape sequence.

To characterize the response profiles of a subset of the LC4DNs, I recorded DNp02, DNp04 and DNp06 and presented looming stimuli. I found strong responses, especially at fast looming expansion rates. All DNs were more active at the fastest looming rate tested (l/v = 10 ms). Spiking activity was highest during the period of fastest expansion of the looming stimulus, so I did not find clear evidence for peak activity during different periods of the looming stimulus. There may be other properties of the response that better explain the control than peak activity, such as the timing of the first spike.

To investigate how different attributes of the looming responses correspond to the escape behavior, I tried to perform recordings while measuring escape behavior. GF spike activity has a one-to-one correspondence with leg extension and flight initiation through *in vivo* electrophysiology experiments [155], and I used these same methods to investigate the LC4DNS.

The escape sub-behaviors could be initiated by a single spike, like the GFs. Alternatively, because the recorded LC4DNs can fire bursts of spikes, there may be a spike rate code where a period of high activity corresponds to the initiation and amplitude of the behavior. For example, in postural adjustment, the magnitude of displacement of the center-of-mass of the fly could be controlled by the number of spikes in DNp02. While significance of the tuning in the LC4DNs will require investigation of downstream VNC circuits, it is critical and possible now to correlate the measured activity to observed behavioral output.

In my recordings, I utilized a wingbeat tachometer to detect flight initiation (a proxy for takeoff). I did not observe consistent flight initiation to looming stimuli. In some experiments, I used a small piece of tissue attached to a rod to provide tarsal contact. Because the GF is likely intact in these preparations and could generate some escapes, it is most likely that the flies were not in a sufficiently healthy state to perform the behavior due to the damage from experimental access required for the pipette. The relationship between spike activity and behavior remains unresolved. For now, our understanding of the relationship between activity and behavior is limited to the FlyPEZ optogenetic activation experiments, in which we assume activation drives spiking activity.

If we could assess the correspondence between LC4DN activity and behavior, we also determine whether the DNs are active during behaviors other than escape. The GF appears to have a dedicated role for escape behaviors. This is not necessarily the case with the other LC4DNs. My recordings show that they are tuned to fast visual stimuli, but I also observed mechanosensory responses as well, indicating that other inputs drive the LC4DN outside of the looming stimulus context. While the activation data implicates the DNs in escape, they may serve distinct roles when the fly is flying, such as object avoidance. Multi-behavior capabilities in LC4DNs would indicate that their axonal targets, including the lower tectulum tract in the VNC, are motor centers which have the capability to read out DN activity into distinct actions. For now, we do not have evidence for such circuit properties.

REFERENCES

[1] S. Agrawal, S. Safarik, and M. Dickinson. The relative roles of vision and chemosensation in mate recognition of drosophila melanogaster. *Journal of Experimental Biology*, 217(15):2796–2805, 2014.

[2] T. Alisch, J. D. Crall, D. Zucker, and B. L. de Bivort. Maple: a modular automated platform for large-scale experiments, a low-cost robot for integrated animal-handling and phenotyping. *bioRxiv*, page 239459, 2017.

[3] A. P. Alivisatos, M. Chun, G. M. Church, R. J. Greenspan, M. L. Roukes, and R. Yuste. The brain activity map project and the challenge of functional connectomics. *Neuron*, 74(6):970 – 974, 2012.

[4] M. J. Allen, T. A. Godenschwege, M. A. Tanouye, and P. Phelan. Making an escape: Development and function of the drosophila giant fibre system. *Seminars in Cell & Developmental Biology*, 17(1):31–41, Feb. 2006.

[5] J. M. Allman. *Evolving Brains*. Scientific American Library, 1040-3213; no. 68. Henry Holt and Company, 1st edition, 2000.

[6] Y. Aso, D. Hattori, Y. Yu, R. M. Johnston, N. A. Iyer, T.-T. B. Ngo, H. Dionne, L. F. Abbott, R. Axel, H. Tanimoto, and G. M. Rubin. The neuronal architecture of the mushroom body provides a logic for associative learning. *eLife*, 3:e04577, Dec. 2014.

[7] Y. Aso, D. Sitaraman, T. Ichinose, K. R. Kaun, K. Vogt, G. Belliart-Guerin, P. Y. Placais, A. A. Robie, N. Yamagata, C. Schnaitmann, W. J. Rowell, R. M. Johnston, T. T. Ngo, N. Chen, W. Korff, M. N. Nitabach, U. Heberlein, T. Preat, K. M. Branson, H. Tanimoto, and G. M. Rubin. Mushroom body output neurons encode valence and guide memory-based action selection in drosophila. *Elife*, 3:e04580, 2014.

[8] Y. Aso, D. Sitaraman, T. Ichinose, K. R. Kaun, K. Vogt, G. Belliart-Guérin, P.-Y. Plaçais, A. A. Robie, N. Yamagata, C. Schnaitmann, W. J. Rowell, R. M. Johnston, T.-T. B. Ngo, N. Chen, W. Korff, M. N. Nitabach, U. Heberlein, T. Preat, K. M. Branson, H. Tanimoto, and G. M. Rubin. Mushroom body output neurons encode valence and guide memory-based action selection in Drosophila. *eLife*, 3:e04580, Dec. 2014.

[9] J. P. Bacon and N. J. Strausfeld. The dipteran 'giant fibre'pathway: neurons and signals. *Journal of Comparative Physiology A*, 158(4):529–548, 1986.

[10] R. A. Baines, J. P. Uhler, A. Thompson, S. T. Sweeney, and M. Bate. Altered electrical properties in Drosophila neurons developing without synaptic transmission. *Journal of Neuroscience*, 21(5):1523–1531, Mar. 2001.

[11] D. E. Bath, J. R. Stowers, D. Hörmann, A. Poehlmann, B. J. Dickson, and A. D. Straw. Flymad: rapid thermogenetic control of neuronal activity in freely walking drosophila. *Nature Methods*, 11(7):756–762, 2014.

[12] S. Batsching, R. Wolf, and M. Heisenberg. Inescapable stress changes walking behavior in flies - learned helplessness revisited. *PLoS One*, 11(11):e0167066, 2016.

[13] G. J. Berman, W. Bialek, and J. W. Shaevitz. Predictability and hierarchy in drosophila behavior. *Proceedings of the National Academy of Sciences*, 113(42):11943–11948, 2016.

[14] G. Blaj and J. H. van Hateren. Saccadic head and thorax movements in freely walking blowflies. *Journal of Comparative Physiology A*, 190(11):861–868, 2004.

[15] A. Borst. Neural Circuits for Motion Vision in the Fly. *Cold Spring Harbor Symposia on Quantitative Biology*, 79:131–139, June 2015.

[16] D. H. Brainard. The psychophysics toolbox. *Spatial Vision*, 10(4):433–436, 1997.

[17] A. H. Brand and N. Perrimon. Targeted gene expression as a means of altering cell fates and generating dominant phenotypes. *Development*, 118(2):401–415, June 1993.

[18] K. Branson, A. A. Robie, J. Bender, P. Perona, and M. H. Dickinson. High-throughput ethomics in large groups of drosophila. *Nature Methods*, 6(6):451–457, 2009.

[19] R. Brent and M. Ptashne. A eukaryotic transcriptional activator bearing the DNA specificity of a prokaryotic repressor. *Cell*, 43(3 Pt 2):729–736, Dec. 1985.

[20] S. M. Buchanan, J. S. Kain, and B. L. de Bivort. Neuronal control of locomotor handedness in drosophila. *Proceedings of the National Academy of Sciences*, 112(21):6700–5, 2015.

[21] J. Cande, G. J. Berman, S. Namiki, J. Qiu, W. Korff, G. Card, J. W. Shaevitz, and D. L. Stern. Optogenetic dissection of descending behavioral control in drosophila. *bioRxiv*, page 230128, 2017.

[22] G. Card and M. Dickinson. Performance trade-offs in the flight initiation of Drosophila. *Journal of Experimental Biology*, 211(3):341–353, Feb. 2008.

[23] G. Card and M. H. Dickinson. Visually Mediated Motor Planning in the Escape Response of Drosophila. *Current Biology*, 18(17):1300–1307, Sept. 2008.

[24] G. Card and M. H. Dickinson. Visually mediated motor planning in the escape response of drosophila. *Current Biology*, 18(17):1300–1307, 2008.

[25] G. M. Card. Escape behaviors in insects. *Current Opinion in Neurobiology*, 22(2):180–186, Apr. 2012.

[26] C.-L. Chen, L. Hermans, M. C. Viswanathan, D. Fortun, M. Unser, A. Cammarato, M. H. Dickinson, and P. Ramdya. Imaging neural activity in the ventral nerve cord of behaving adult drosophila. *bioRxiv*, 2018.

[27] M. Cheng and J. Outerbridge. Inter-saccadic interval analysis of optokinetic nystagmus. *Vision Research*, 14(11):1053–1058, 1974.

[28] M. E. Chiappe, J. D. Seelig, M. B. Reiser, and V. Jayaraman. Walking Modulates Speed Sensitivity in Drosophila Motion Vision. *Current Biology*, 20(16):1470–1475, Aug. 2010.

[29] W. Cho, U. Heberlein, and F. W. Wolf. Habituation of an odorant-induced startle response in Drosophila. *Genes, Brain and Behavior*, 3(3):127–137, June 2004.

[30] P. Coen, J. Clemens, A. J. Weinstein, D. A. Pacheco, Y. Deng, and M. Murthy. Dynamic sensory cues shape song structure in drosophila. *Nature*, 507(7491):233–7, 2014.

[31] S. E. J. de Vries and T. R. Clandinin. Loom-Sensitive Neurons Link Computation to Actionin the Drosophila Visual System. *Current Biology*, 22(5):353–362, Mar. 2012.

[32] M. Dickinson and C. F. Moss. Editorial overview. *Current Opinion in Neurobiology*, 22(2):177–179, 2012.

[33] H. Dionne, K. L. Hibbard, A. Cavallaro, J.-C. Kao, and G. M. Rubin. Genetic reagents for making split-gal4 lines indrosophila. *Genetics*, 209(1):31–35, Mar 2018.

[34] P. Domenici, J. M. Blagburn, and J. P. Bacon. Animal escapology I: theoretical issues and emerging trends in escape trajectories. *Journal of Experimental Biology*, 214(15):2463–2473, July 2011.

[35] P. Domenici, J. M. Blagburn, and J. P. Bacon. Animal escapology II: escape trajectory case studies. *Journal of Experimental Biology*, 214(15):2474–2494, July 2011.

[36] P. Domenici, D. Booth, J. M. Blagburn, and J. P. Bacon. Cockroaches Keep Predators Guessing by Using Preferred Escape Trajectories. *CURBIO*, 18(22):1792–1796, Nov. 2008.

[37] T. Drew, S. Prentice, and B. Schepens. Cortical and brainstem control of locomotion. In *Progress in Brain Research*, volume 143, pages 251–261. Elsevier, 2004.

[38] J. B. Duffy. GAL4 system in Drosophila: a fly geneticist's Swiss army knife. *Genesis*, 34(1-2):1–15, Sept. 2002.

[39] T. W. Dunn, C. Gebhardt, E. A. Naumann, C. Riegler, M. B. Ahrens, F. Engert, and F. Del Bene. Neural Circuits Underlying Visually Evoked Escapes in Larval Zebrafish. *Neuron*, 89(3):613–628, Feb. 2016.

[40] C. Dupre and R. Yuste. Non-overlapping Neural Networks in Hydra vulgaris. *Current Biology*, 27(8):1085–1097, Apr. 2017.

[41] R. Eaton, R. Lee, and M. Foreman. The mauthner cell and other identified neurons of the brainstem escape network of fish. *Progress in Neurobiology*, 63(4):467 – 485, 2001.

[42] R. C. Eaton. *Neural Mechanisms of Startle Behavior*. Springer US, 1st edition, 1984.

[43] R. C. Eaton and D. S. Emberley. How stimulus direction determines the trajectory of the Mauthner-initiated escape response in a teleost fish. *The Journal of Experimental Biology*, 161:469–487, Nov. 1991.

[44] R. C. Eaton and D. S. Emberley. How stimulus direction determines the trajectory of the mauthner-initiated escape response in a teleost fish. *Journal of Experimental Biology*, 161(1):469–487, 1991.

[45] J. E. Engel and C.-F. Wu. Altered habituation of an identified escape circuit in drosophila memory mutants. *Journal of Neuroscience*, 16(10):3486–3499, 1996.

[46] K. F. Fischbach and A. P. M. Dittrich. The optic lobe of Drosophila Melanogaster. I. A Golgi analysis of wild-type structure. *Cell and Tissue Research*, 258(3):441–475, July 1989.

[47] H. Fotowat, A. Fayyazuddin, H. J. Bellen, and F. Gabbiani. A Novel Neuronal Pathway for Visually Guided Escape in Drosophila melanogaster. *Journal of Neurophysiology*, 102(2):875–885, July 2009.

[48] H. Fotowat and F. Gabbiani. Collision Detection as a Model for Sensory-Motor Integration. *Annual review of neuroscience*, 34(1):1–19, July 2011.

[49] H. Fotowat, R. R. Harrison, and F. Gabbiani. Multiplexing of motor information in the discharge of a collision detecting neuron during escape behaviors. *Neuron*, 69(1):147–158, Jan 2011.

[50] H. Fotowat, R. R. Harrison, and F. Gabbiani. Multiplexing of motor information in the discharge of a collision detecting neuron during escape behaviors. *Neuron*, 69(1):147 – 158, 2011.

[51] T. Fujiwara, T. L. Cruz, J. P. Bohnslav, and M. E. Chiappe. A faithful internal representation of walking movements in the drosophila visual system. *Nature neuroscience*, 20(1):72–81, 2017.

[52] F. Gabbiani, H. G. Krapp, C. Koch, and G. Laurent. Multiplicative computation in a visual neuron sensitive to looming. *Nature*, 420(6913):320–324, Nov. 2002.

[53] F. Gabbiani, H. G. Krapp, and G. Laurent. Computation of object approach by a wide-field, motion-sensitive neuron. *Journal of Neuroscience*, 19(3):1122–1141, Jan. 1999.

[54] J. W. Gargano, I. Martin, P. Bhandari, and M. S. Grotewiel. Rapid iterative negative geotaxis (ring): a new method for assessing age-related locomotor decline in drosophila. *Experimental Gerontology*, 40(5):386–95, 2005.

[55] B. R. Geurten, P. Jähde, K. Corthals, and M. C. Göpfert. Saccadic body turns in walking drosophila. *Frontiers in Behavioral Neuroscience*, 8:365, 2014.

[56] W. T. Gibson, C. R. Gonzalez, C. Fernandez, L. Ramasamy, T. Tabachnik, R. R. Du, P. D. Felsen, M. R. Maire, P. Perona, and D. J. Anderson. Behavioral Responses to a Repetitive Visual Threat Stimulus Express a Persistent State of Defensive Arousal in Drosophila. *Current Biology*, 25(11):1401–1415, June 2015.

[57] K. G. Götz and H. Wenking. Visual control of locomotion in the walking fruitfly drosophila. *Journal of Comparative Physiology*, 85(3):235–266, 1973.

[58] N. W. Gouwens and R. I. Wilson. Signal propagation in drosophila central neurons. *Journal of Neuroscience*, 29(19):6239–6249, 2009.

[59] W. Gronenberg and N. J. Strausfeld. Descending neurons supplying the neck and flight motor of diptera: Physiological and anatomical characteristics. *The Journal of Comparative Neurology*, 302(4):973–991, Dec 1990.

[60] M. E. Hale, H. R. Katz, M. Y. Peek, and R. T. Fremont. Neural circuits that drive startle behavior, with a focus on the Mauthner cells and spiral fiber neurons of fishes. *Journal of Neurogenetics*, 30(2):89–100, June 2016.

[61] S. Hammond and M. O'Shea. Escape flight initiation in the fly. *Journal of Comparative Physiology A*, 193(4):471–476, Jan. 2007.

[62] S. Hampel and A. M. Seeds. Targeted manipulation of neuronal activity in behaving adult flies. In A. Celik and M. F. Wernet, editors, *Decoding Neural Circuit Structure and Function*, book section 7, pages 191–222. Springer, 2017.

[63] C. D. Harvey, F. Collman, D. A. Dombeck, and D. W. Tank. Intracellular dynamics of hippocampal place cells during virtual navigation. *Nature*, 461(7266):941–6, 2009.

[64] N. Hatsopoulos, F. Gabbiani, and G. Laurent. Elementary computation of object approach by a wide-field visual neuron. *Science*, 270(5238):1000–1003, 1995.

[65] M. Heisenberg and R. Wolf. *Vision in Drosophila: genetics of microbehavior*, volume 12 of *Studies of Brain Function*. Springer Berlin Heidelberg, 1984.

[66] J. M. Hemmi. Predator avoidance in fiddler crabs: 1. Escape decisions in relation to the risk of predation. *Animal Behaviour*, 69(3):603–614, Mar. 2005.

[67] E. D. Hoopfer, Y. Jung, H. K. Inagaki, G. M. Rubin, and D. J. Anderson. P1 interneurons promote a persistent internal state that enhances inter-male aggression in drosophila. *Elife*, 4, 2015.

[68] C. T. Hsu and V. Bhandawat. Organization of descending neurons in Drosophila melanogaster. *Scientific Reports*, 6:20259, Feb. 2016.

[69] C. Hu, M. Petersen, N. Hoyer, B. Spitzweck, F. Tenedini, D. Wang, A. Gruschka, L. S. Burchardt, E. Szpotowicz, M. Schweizer, A. R. Guntur, C. H. Yang, and P. Soba. Sensory integration and neuromodulatory feedback facilitate drosophila mechanonociceptive behavior. *Nature Neuroscience*, 20(8):1085–1095, 2017.

[70] H. K. Inagaki, Y. Jung, E. D. Hoopfer, A. M. Wong, N. Mishra, J. Y. Lin, R. Y. Tsien, and D. J. Anderson. Optogenetic control of Drosophila using a red-shifted channelrhodopsin reveals experience-dependent influences on courtship. *Nature Methods*, 11(3):325–332, Mar. 2014.

[71] A. Jenett, G. M. Rubin, T.-T. Ngo, D. Shepherd, C. Murphy, H. Dionne, B. D. Pfeiffer, A. Cavallaro, D. Hall, and J. Jeter. A gal4-driver line resource for drosophila neurobiology. *Cell reports*, 2(4):991–1001, 2012.

[72] M. Kabra, A. A. Robie, M. Rivera-Alba, S. Branson, and K. Branson. Jaaba: interactive machine learning for automatic annotation of animal behavior. *Nature Methods*, 10(1):64–67, 2012.

[73] A. Kamikouchi, H. K. Inagaki, T. Effertz, O. Hendrich, A. Fiala, M. C. Göpfert, and K. Ito. The neural basis of Drosophila gravity-sensing and hearing. *Nature*, 457(7235):165–171, Mar. 2009.

[74] E. Kandel. *Principles of Neural Science, Fifth Edition*. Principles of Neural Science. McGraw-Hill Education, 2013.

[75] M. Kanou, M. Ohshima, and J. Inoue. The Air-puff Evoked Escape Behavior of the Cricket Gryllus bimaculatus and its Compensational Recovery after Cercal Ablations. *Zoological Science*, 16(1):71–79, Feb. 1999.

[76] A. Y. Katsov and T. R. Clandinin. Motion Processing Streams in Drosophila Are Behaviorally Specialized. *Neuron*, 59(2):322–335, July 2008.

[77] O. Kiehn. Decoding the organization of spinal circuits that control locomotion. *Nature Reviews Neuroscience*, 17(4):224–238, Mar. 2016.

[78] A. J. Kim, L. M. Fenk, C. Lyu, and G. Maimon. Quantitative predictions orchestrate visual signaling in drosophila. *Cell*, 168(1):280–294. e12, 2017.

[79] S. S. Kim, R. Franconville, D. Turner-Evans, and V. Jayaraman. Optogenetics in drosophila melanogaster. In *New Techniques in Systems Neuroscience*, pages 147–176. Springer International Publishing, Cham, 2015.

[80] D. G. King and R. J. Wyman. Anatomy of the giant fibre pathway in Drosophila. I. Three thoracic components of the pathway. *Journal of Neurocytology*, 9(6):753–770, Dec. 1980.

[81] N. C. Klapoetke, Y. Murata, S. S. Kim, S. R. Pulver, A. Birdsey-Benson, Y. K. Cho, T. K. Morimoto, A. S. Chuong, E. J. Carpenter, Z. Tian, J. Wang, Y. Xie, Z. Yan, Y. Zhang, B. Y. Chow, B. Surek, M. Melkonian, V. Jayaraman, M. Constantine-Paton, G. K.-S. Wong, and E. S. Boyden. Independent optical excitation of distinct neural populations. *Nature Methods*, 11(3):338–346, Feb. 2014.

[82] N. C. Klapoetke, A. Nern, M. Y. Peek, E. M. Rogers, P. Breads, G. M. Rubin, M. B. Reiser, and G. M. Card. Ultra-selective looming detection from radial motion opponency. *Nature*, 551(7679):237–241, Nov. 2017.

[83] M. Kleiner, D. Brainard, and D. Pelli. What's new in psychtoolbox-3. *Perception*, 36(ECVP Abstract Supplement), 2007.

[84] H. Korn and D. S. Faber. The mauthner cell half a century later: A neurobiological model for decision-making? *Neuron*, 47(1):13 – 28, 2005.

[85] M. Koto, M. A. Tanouye, A. Ferrus, J. B. Thomas, and R. J. Wyman. The morphology of the cervical giant fiber neuron ofdrosophila. *Brain Research*, 221(2):213 – 217, 1981.

[86] I. Kupfermann and K. R. Weiss. The command neuron concept. *Behavioral and Brain Sciences*, 1(01):3, Mar 1978.

[87] S.-L. Lai and T. Lee. Genetic mosaic with dual binary transcriptional systems in Drosophila. *Nature Neuroscience*, 9(5):703–709, Apr. 2006.

[88] G. Laurent and F. Gabbiani. Collision-avoidance: nature's many solutions. *Nature Neuroscience*, 1(4):261–263, Aug. 1998.

[89] B. P. Lehnert, A. E. Baker, Q. Gaudry, A.-S. Chiang, and R. I. Wilson. Distinct roles of TRP channels in auditory transduction and amplification in Drosophila. *Neuron*, 77(1):115–128, Jan. 2013.

[90] J. Levine and D. Tracey. Structure and function of the giant motorneuron ofdrosophila melanogaster. *Journal of comparative physiology*, 87(3):213–235, Sep 1973.

[91] K. S. Liu and J. R. Fetcho. Laser ablations reveal functional relationships of segmental hindbrain neurons in zebrafish. *Neuron*, 23(2):325–335, June 1999.

[92] Y.-C. Liu, I. Bailey, and M. E. Hale. Alternative startle motor patterns and behaviors in the larval zebrafish (Danio rerio). *Journal of Comparative Physiology A*, 198(1):11–24, Oct. 2011.

[93] H. Luan, N. C. Peabody, C. R. Vinson, and B. H. White. Refined Spatial Manipulation of Neuronal Function by Combinatorial Restriction of Transgene Expression. *Neuron*, 52(3):425–436, Nov. 2006.

[94] G. Maimon, A. D. Straw, and M. H. Dickinson. Active flight increases the gain of visual motion processing in Drosophila. *Nature Neuroscience*, 13(3):393–399, Feb. 2010.

[95] E. Marder. Understanding brains: details, intuition, and big data. *PLoS Biology*, 13(5):e1002147, May 2015.

[96] D. Marr and T. Poggio. From understanding computation to understanding neural circuitry. Memo, Massachusetts Institute of Technology Artificial Intelligence Laboratory, May 1976. A.I. Memo 357.

[97] D. J. Mellert, W. R. Williamson, T. R. Shirangi, G. M. Card, and J. W. Truman. Genetic and environmental control of neurodevelopmental robustness in drosophila. *PloS one*, 11(5):e0155957, 2016.

[98] C. S. Mendes, I. Bartos, T. Akay, S. Márka, and R. S. Mann. Quantification of gait parameters in freely walking wild type and sensory deprived drosophila melanogaster. *Elife*, 2:e00231, 2013.

[99] R. Menzel. Spectral sensitivity and color vision in invertebrates. In H. Autrum, editor, *Handbook of Sensory Physiology*, volume VII/6A, chapter 9, pages 503–580. Springer Verlag, 1979.

[100] J. J. Milde and N. J. Strausfeld. Cluster organization and response characteristics of the giant fiber pathway of the blowfly Calliphora erythrocephala. *The Journal of Comparative Neurology*, 294(1):59–75, Apr. 1990.

[101] L. Mu, J. P. Bacon, K. Ito, and N. J. Strausfeld. Responses of drosophila giant descending neurons to visual and mechanical stimuli. *Journal of Experimental Biology*, 217(12):2121–2129, Mar 2014.

[102] L. Mu, K. Ito, J. P. Bacon, and N. J. Strausfeld. Optic Glomeruli and Their Inputs in Drosophila Share an Organizational Ground Pattern with the Antennal Lobes. *Journal of Neuroscience*, 32(18):6061–6071, May 2012.

[103] F. T. Muijres, M. J. Elzinga, J. M. Melis, and M. H. Dickinson. Flies evade looming targets by executing rapid visually directed banked turns. *Science*, 344(6180):172–177, Apr 2014.

[104] M. Murthy and G. Turner. Whole-Cell In Vivo Patch-Clamp Recordings in the Drosophila Brain. *Cold Spring Harbor Protocols*, 2013(2):pdb.prot071704–pdb.prot071704, Feb. 2013.

[105] W. NACHTIGALL and D. M. WILSON. Neuro-muscular control of dipteran flight. *Journal of Experimental Biology*, 47(1):77–97, 1967.

[106] S. Namiki, M. H. Dickinson, A. M. Wong, W. Korff, and G. M. Card. The functional organization of descending sensory-motor pathways in drosophila. *eLife*, 7:e34272, 2018.

[107] D. Oliva, V. Medan, and D. Tomsic. Escape behavior and neuronal responses to looming stimuli in the crab chasmagnathus granulatus (decapoda: Grapsidae). *Journal of Experimental Biology*, 210(5):865–880, 2007.

[108] D. Oliva and D. Tomsic. Computation of object approach by a system of visual motion-sensitive neurons in the crab Neohelice. *Journal of Neurophysiology*, 112(6):1477–1490, Sept. 2014.

[109] D. O'Malley and Y. Kao. Imaging the functional organization of zebrafish hindbrain segments during escape behaviors. *Neuron*, pages 1–11, Dec. 1996.

[110] M. O'Shea and J. Williams. The anatomy and output connection of a locust visual interneurone; the lobular giant movement detector (LGMD) neurone. *Journal of Comparative Physiology A*, 1974.

[111] H. Otsuna and K. Ito. Systematic analysis of the visual projection neurons ofDrosophila melanogaster. I. Lobula-specific pathways. *The Journal of Comparative Neurology*, 497(6):928–958, 2006.

[112] K. Panser, L. Tirian, F. Schulze, S. Villalba, G. S. Jefferis, K. Bühler, and A. D. Straw. Automatic segmentation of drosophila neural compartments using gal4 expression data reveals novel visual pathways. *Current Biology*, 26(15):1943 – 1954, 2016.

[113] K. Panser, L. Tirian, F. Schulze, S. Villalba, G. S. X. E. Jefferis, K. Bühler, and A. D. Straw. Automatic Segmentation of Drosophila Neural Compartments Using GAL4 Expression Data Reveals Novel Visual Pathways. *Current Biology*, 26(15):1943–1954, Aug. 2016.

[114] M. Y. Peek and G. M. Card. ScienceDirectComparative approaches to escape. *Current Opinion in Neurobiology*, 41:167–173, Dec. 2016.

[115] D. G. Pelli. The videotoolbox software for visual psychophysics: transforming numbers into movies. *Spatial Vision*, 10(4):437–42, 1997.

[116] B. D. Pfeiffer, T. T. B. Ngo, K. L. Hibbard, C. Murphy, A. Jenett, J. W. Truman, and G. M. Rubin. Refinement of Tools for Targeted Gene Expression in Drosophila. *Genetics*, 186(2):735–755, Oct. 2010.

[117] B. D. Pfeiffer, J. W. Truman, and G. M. Rubin. Using translational enhancers to increase transgene expression in drosophila. *Proceedings of the National Academy of Sciences*, 109(17):6626–6631, Apr 2012.

[118] P. Phelan, M. Nakagawa, M. B. Wilkin, K. G. Moffat, C. J. O'Kane, J. A. Davies, and J. P. Bacon. Mutations in shaking-B prevent electrical synapse formation in the Drosophila giant fiber system. *Journal of Neuroscience*, 16(3):1101–1113, Feb. 1996.

[119] S. Pick and R. Strauss. Goal-driven behavioral adaptations in gap-climbing drosophila. *Current Biology*, 15(16):1473–8, 2005.

[120] M. E. Power. The thoracico-abdominal nervous system of an adult insect, Drosophila melanogaster. *The Journal of Comparative Neurology*, 88(3):347–409, Jan. 1948.

[121] P. Ramdya, P. Lichocki, S. Cruchet, L. Frisch, W. Tse, D. Floreano, and R. Benton. Mechanosensory interactions drive collective behaviour in drosophila. *Nature*, 519(7542):233–6, 2015.

[122] A. A. Robie, J. Hirokawa, A. W. Edwards, L. A. Umayam, A. Lee, M. L. Phillips, G. M. Card, W. Korff, G. M. Rubin, J. H. Simpson, M. B. Reiser, and K. Branson. Mapping the neural substrates of behavior. *Cell*, 170(2):393–406.e28, 2017.

[123] S. Saalfeld, A. Cardona, V. Hartenstein, and P. Tomancak. Catmaid: collaborative annotation toolkit for massive amounts of image data. *Bioinformatics*, 25(15):1984–1986, Apr 2009.

[124] R. D. Santer, Y. Yamawaki, F. C. Rind, and P. J. Simmons. Motor activity and trajectory control during escape jumping in the locust Locusta migratoria. *Journal of Comparative Physiology A*, 191(10):965–975, July 2005.

[125] J. Savall, E. T. W. Ho, C. Huang, J. R. Maxey, and M. J. Schnitzer. Dexterous robotic manipulation of alert adult drosophila for high-content experimentation. *Nature Methods*, 12(7):657, 2015.

[126] F. Schlaghecken, L. Rowley, S. Sembi, R. Simmons, and D. Whitcomb. The negative compatibility effect: A case for self-inhibition. *Advances in Cognitive Psychology*, 3(1-2):227–40, 2008.

[127] B. Schnell, I. G. Ros, and M. H. Dickinson. A descending neuron correlated with the rapid steering maneuvers of flying drosophila. *Current Biology*, 27(8):1200–1205, 2017.

[128] O. Schwarz, A. A. Bohra, X. Liu, H. Reichert, K. Vijay Raghavan, and J. Pielage. Motor control of drosophila feeding behavior. *eLife*, 6:e19892, 2017.

[129] C. Shang, Z. Liu, Z. Chen, Y. Shi, Q. Wang, and S. Liu. A parvalbumin-positive excitatory visual pathway to trigger fear responses in mice. . . . , 2015.

[130] J. C. Simon and M. H. Dickinson. A new chamber for studying the behavior of drosophila. *PLoS ONE*, 5(1):e8793, 2010.

[131] J. H. Simpson. *Chapter 3 Mapping and Manipulating Neural Circuits in the Fly Brain*, volume 65 of *Advances in Genetics*. Academic Press, 2009.

[132] J. H. Simpson and L. L. Looger. Functional imaging and optogenetics in drosophila. *Genetics*, 208(4):1291–1309, 2018.

[133] E. Sivan-Loukianova and D. F. Eberl. Synaptic ultrastructure ofDrosophila Johnston's organ axon terminals as revealed by an enhancer trap. *The Journal of Comparative Neurology*, 491(1):46–55, 2005.

[134] B. Soibam, M. Mann, L. Liu, J. Tran, M. Lobaina, Y. Y. Kang, G. H. Gunaratne, S. Pletcher, and G. Roman. Open-field arena boundary is a primary object of exploration for drosophila. *Brain and Behavior*, 2(2):97–108, 2012.

[135] L. Squire. *Fundamental Neuroscience*. Academic Press/Elsevier, 3rd edition, 2008.

[136] J. R. Stowers, A. Fuhrmann, M. Hofbauer, M. Streinzer, A. Schmid, M. H. Dickinson, and A. D. Straw. Reverse engineering animal vision with virtual reality and genetics. *Computer*, 47(7):38–45, 2014.

[137] N. Strausfeld, U. Bassemir, R. Singh, and J. Bacon. Organizational principles of outputs from dipteran brains. *Journal of Insect Physiology*, 30(1):73 – 93, 1984.

[138] N. J. Strausfeld and U. K. Bassemir. Cobalt-coupled neurons of a giant fibre system in Diptera. *Journal of Neurocytology*, 12(6):971–991, Dec. 1983.

[139] N. J. Strausfeld and J.-Y. Okamura. Visual system of calliphorid flies: Organization of optic glomeruli and their lobula complex efferents. *The Journal of Comparative Neurology*, 500(1):166–188, 2006.

[140] N. J. Strausfeld, I. Sinakevitch, and J.-Y. Okamura. Organization of local interneurons in optic glomeruli of the dipterous visual system and comparisons with the antennal lobes. *Developmental Neurobiology*, 67(10):1267–1288, 2007.

[141] H. Sun and B. J. Frost. Computation of different optical variables of looming objects in pigeon nucleus rotundus neurons. *Nature Neuroscience*, 1(4):296–303, Aug. 1998.

[142] A. Suska, I. Miguel-Aliaga, and S. Thor. Segment-specific generation of drosophila capability neuropeptide neurons by multi-faceted hox cues. *Developmental Biology*, 353(1):72–80, May 2011.

[143] J. S. Takahashi, K. Shimomura, and V. Kumar. Searching for genes underlying behavior: lessons from circadian rhythms. *Science*, 322(5903):909–912, 2008.

[144] J. Takalo, A. Piironen, A. Honkanen, M. Lempeä, M. Aikio, T. Tuukkanen, and M. Vähäsöyrinki. A fast and flexible panoramic virtual reality system for behavioural and electrophysiological experiments. *Scientific Reports*, 2(1):1602, 2012.

[145] M. A. Tanouye and R. J. Wyman. Motor outputs of giant nerve fiber in Drosophila. *Journal of Neurophysiology*, 44(2):405–421, 1980.

[146] E. Tauber and J. Camhi. The wind-evoked escape behavior of the cricket Gryllus bimaculatus: integration of behavioral elements. *Journal of Experimental Biology*, 198(Pt 9):1895–1907, 1995.

[147] I. Temizer, J. C. Donovan, H. Baier, and J. L. Semmelhack. A visual pathway for looming-evoked escape in larval zebrafish. *Current Biology*, 25(14):1823–1834, 2015.

[148] L. Tirian and B. Dickson. The vt gal4, lexa, and split-gal4 driver line collections for targeted expression in the drosophila nervous system. *bioRxiv*, 2017.

[149] S. Trannoy, B. Chowdhury, and E. A. Kravitz. Handling alters aggression and "loser" effect formation in drosophila melanogaster. *Learning & Memory*, 22(2):64–68, 2015.

[150] S. Trannoy, B. Chowdhury, and E. A. Kravitz. A new approach that eliminates handling for studying aggression and the "loser" effect in drosophila melanogaster. *Journal of Visualized Experiments*, 106(e53395), 2015.

[151] J. Trimarchi and A. Schneiderman. Different neural pathways coordinate Drosophila flight initiations evoked by visual and olfactory stimuli. *Journal of Experimental Biology*, 198(Pt 5):1099–1104, May 1995.

[152] J. Trimarchi and A. Schneiderman. Initiation of flight in the unrestrained fly, Drosophila melanogaster. *Journal of Zoology*, 1995.

[153] J. Trimarchi and A. Schneiderman. Initiation of flight in the unrestrained fly, drosophila melanogaster. *Journal of Zoology*, 235(2):211–222, 1995.

[154] J. C. Tuthill, A. Nern, S. L. Holtz, G. M. Rubin, and M. B. Reiser. Contributions of the 12 Neuron Classes in the Fly Lamina to Motion Vision. *Neuron*, 79(1):128–140, July 2013.

[155] C. R. von Reyn, P. Breads, M. Y. Peek, G. Z. Zheng, W. R. Williamson, A. L. Yee, A. Leonardo, and G. M. Card. A spike-timing mechanism for action selection. *Nature Publishing Group*, 17(7):962–970, June 2014.

[156] C. R. von Reyn, A. Nern, W. R. Williamson, P. Breads, M. Wu, S. Namiki, and G. M. Card. Feature Integration Drives Probabilistic Behavior in the Drosophila Escape Response. *Neuron*, 94(6):1190–1204.e6, June 2017.

[157] B. White and N. Peabody. Neurotrapping: cellular screens to identify the neural substrates of behavior in drosophila. *Frontiers in Molecular Neuroscience*, 2:20, 2009.

[158] J. S. Wiegert, M. Mahn, M. Prigge, Y. Printz, and O. Yizhar. Silencing neurons: Tools, applications, and experimental constraints. *Neuron*, 95(3):504–529, 2017.

[159] R. I. Wilson, G. C. Turner, and G. Laurent. Transformation of olfactory representations in the Drosophila antennal lobe. *Science (New York, N.Y.)*, 303(5656):366–370, Jan. 2004.

[160] T. Wolff, N. A. Iyer, and G. M. Rubin. Neuroarchitecture and neuroanatomy of the Drosophilacentral complex: A GAL4-based dissection of protocerebral bridge neurons and circuits. *The Journal of Comparative Neurology*, 523(7):997–1037, Dec. 2015.

[161] P. B. Woodbury. The geometry of predator avoidance by the blue crab, callinectes sapidus Rathbun. *Animal Behaviour*, 34(1):28–37, Feb. 1986.

[162] M. Wu, A. Nern, W. R. Williamson, M. M. Morimoto, M. B. Reiser, G. M. Card, and G. M. Rubin. Visual projection neurons in the Drosophila lobula link feature detection to distinct behavioral programs. *eLife*, 5, Dec. 2016.

[163] R. J. Wyman, J. B. Thomas, L. Salkoff, and D. G. King. *The Drosophila Giant Fiber System*, pages 133–161. Springer US, Boston, MA, 1984.

[164] A. Yamamoto, L. Zwarts, P. Callaerts, K. Norga, T. F. C. Mackay, and R. R. H. Anholt. Neurogenetic networks for startle-induced locomotion in Drosophila melanogaster. *Proceedings of the National Academy of Sciences*, 105(34):12393–12398, Aug. 2008.

[165] R. Yuste. Circuit neuroscience: the road ahead. *Frontiers in neuroscience*, 2(1):6–9, July 2008.

[166] R. Zacarias, S. Namiki, G. M. Card, M. L. Vasconcelos, and M. A. Moita. Speed dependent descending control of freezing behavior in drosophila melanogaster. *Nature Communications*, 9(1), Sep 2018.

[167] S. Zhang and M. Srinivasan. Prior experience enhances pattern discrimination in insect vision. *Nature*, 368(6469):330, 1994.

[168] Z. Zheng, J. S. Lauritzen, E. Perlman, C. G. Robinson, M. Nichols, D. Milkie, O. Torrens, J. Price, C. B. Fisher, N. Sharifi, S. A. Calle-Schuler, L. Kmecova, I. J. Ali, B. Karsh, E. T. Trautman, J. A. Bogovic, P. Hanslovsky, G. S. Jefferis, M. Kazhdan, K. Khairy, S. Saalfeld, R. D. Fetter, and D. D. Bock. A complete electron microscopy volume of the brain of adult drosophila melanogaster. *Cell*, 174(3):730 – 743.e22, 2018.